

# Influence of steps and kinks on CO and hydrogen adsorption, co-adsorption and dissociation on Co single crystal surfaces

**Citation for published version (APA):**

Sharma, D. (2025). *Influence of steps and kinks on CO and hydrogen adsorption, co-adsorption and dissociation on Co single crystal surfaces*. [Phd Thesis 1 (Research TU/e / Graduation TU/e), Applied Physics and Science Education]. Eindhoven University of Technology.

**Document status and date:**

Published: 01/05/2025

**Document Version:**

Publisher's PDF, also known as Version of Record (includes final page, issue and volume numbers)

**Please check the document version of this publication:**

- A submitted manuscript is the version of the article upon submission and before peer-review. There can be important differences between the submitted version and the official published version of record. People interested in the research are advised to contact the author for the final version of the publication, or visit the DOI to the publisher's website.
- The final author version and the galley proof are versions of the publication after peer review.
- The final published version features the final layout of the paper including the volume, issue and page numbers.

[Link to publication](#)

**General rights**

Copyright and moral rights for the publications made accessible in the public portal are retained by the authors and/or other copyright owners and it is a condition of accessing publications that users recognise and abide by the legal requirements associated with these rights.

- Users may download and print one copy of any publication from the public portal for the purpose of private study or research.
- You may not further distribute the material or use it for any profit-making activity or commercial gain
- You may freely distribute the URL identifying the publication in the public portal.

If the publication is distributed under the terms of Article 25fa of the Dutch Copyright Act, indicated by the "Taverne" license above, please follow below link for the End User Agreement:

[www.tue.nl/taverne](http://www.tue.nl/taverne)

**Take down policy**

If you believe that this document breaches copyright please contact us at:

[openaccess@tue.nl](mailto:openaccess@tue.nl)

providing details and we will investigate your claim.

# Influence of steps and kinks on CO and hydrogen adsorption, co-adsorption and dissociation on Co single crystal surfaces



Devyani Sharma



# **Influence of steps and kinks on CO and hydrogen adsorption, co-adsorption and dissociation on Co single crystal surfaces**

## **PROEFSCHRIFT**

ter verkrijging van de graad van doctor aan de Technische Universiteit Eindhoven, op gezag van de rector magnificus prof. dr. S.K. Lenaerts, voor een commissie aangewezen door het College voor Promoties, in het openbaar te verdedigen op May 1<sup>st</sup>, 2025 om 11:00.

door

Devyani Sharma

geboren te Delhi, India

Dit proefschrift is goedgekeurd door de promotoren en de samenvatting van de promotiecommissie is als volgt:

voorzitter: prof.dr. P.A. Bobbert  
promotor: prof.dr.ir. M.C.M. van de Sanden  
leden: dr. M.A. Gleeson (DIFFER)  
prof.dr.ir. E.J.M. Hensen  
prof.dr.ir. M. Saeys (Universiteit Gent)  
prof.dr. I.M.N. Groot (Universiteit Leiden)  
prof.dr.ir. W.M.M. Kessels  
prof.dr.ir. G.J. van Rooij

*Het onderzoek of ontwerp dat in dit proefschrift wordt beschreven is uitgevoerd in overeenstemming met de TU/e Gedragscode Wetenschapsbeoefening.*



**DIFFER**



This work was carried out in the context of the SynCat@DIFFER programme between the Dutch Institute for Fundamental Energy Research (DIFFER), Eindhoven University of Technology (TU/e) and Syngaschem BV and is funded jointly by the Dutch Organization for Scientific Research (NWO) and Syngaschem BV. The research was conducted at DIFFER, the Dutch Institute for Fundamental Energy Research, Eindhoven, The Netherlands. DIFFER is part of NWO.

A catalogue record is available from the Eindhoven University of Technology Library

ISBN: 978-94-93431-49-2

Cover design by Devyani Sharma  
Printed by: Proefschriftspecialist - Zaandam  
Copyright ©2025 Devyani Sharma





# Summary

The conversion of CO and hydrogen into long-chain hydrocarbon molecules through Fischer-Tropsch (FT) synthesis over a heterogeneous catalyst has recently gained renewed interest in academia as well as in industry as a consequence of the recent surge in demand for clean fuels in a carbon-neutral society. Instead of relying on traditional coal and gas as feedstocks for FT synthesis, sustainable carbon sources such as CO<sub>2</sub>, agricultural and municipal waste, along with green hydrogen produced via water electrolysis using renewable energy, offer a practical approach towards sustainable hydrocarbon production.

Cobalt catalysts have been widely recognized for its activity in FT synthesis. The experiments in this thesis were carried out on cobalt single crystal surfaces which are structurally well-defined model catalysts. These single crystal surfaces provide a controlled environment with known site concentrations, facilitating the study of the influence of surface structure on reactivity of FTS. To investigate the reactivity of different surface structures, we examined both the flat close-packed Co(0001) surface along with the stepped Co(10 $\bar{1}$ 9) and kinked Co(11 $\bar{2}$ 9) surface. These high Miller index surfaces expose monoatomic steps and kinks, which are separated by close-packed terraces.

Previous research has highlighted the significance of step and kink sites in the reaction, as they are actively involved in the direct dissociation of the CO bond. Therefore, understanding the adsorption of CO on different Co sites, particularly step and kink sites, plays a crucial role in comprehending their contribution to FT synthesis. This study examined and compared the adsorption of CO on flat Co(0001), stepped Co(10 $\bar{1}$ 9), and kinked Co(11 $\bar{2}$ 9) surfaces. The focus was primarily on low CO coverage. Our investigation involved multiple techniques, such as infrared (IR) spectroscopy, X-ray photoelectron spectroscopy (XPS), and density functional theory (DFT) simulations. The IR spectroscopy results indicated the presence of CO adsorbed on the top sites of both the terraces and the steps of the surfaces studied. XPS analysis revealed that there was a slight preference for CO adsorption on stepped sites over terrace sites. This finding was supported by DFT simulations, which demonstrated minimal variation in CO adsorption energies on the top sites of surface atoms with different coordination numbers. The small difference in CO ad-

sorption energy between undercoordinated sites and terrace sites of Co indicated a lack of a strong driving force for CO-induced surface reconstruction. Consequently, under typical reaction conditions, significant CO-induced reconstruction is unlikely to occur, and Co catalyst nanoparticles are expected to retain their initial structure without transforming into highly faceted nanoparticles. This implies that the defect sites will remain accessible for further adsorption during FTS.

During FTS, CO and hydrogen adsorb onto the catalyst surface, leading to surface crowding and lateral interactions between the adsorbates. These interactions have a significant impact on the adsorption behavior of CO and hydrogen. Therefore, non-reactive co-adsorption of CO and hydrogen on the flat Co(0001) surface was investigated to gain further insights into the co-adsorption phenomena. A brief study of CO and hydrogen on Co(0001) on their own serves as background information for the co-adsorption study. The CO adsorption on Co(0001) has been widely discussed in literature. For hydrogen on the other hand, it is observed that when hydrogen is already adsorbed on the surface, the dissociative adsorption of additional hydrogen becomes hindered as the coverage approaches  $\theta = 0.5$  ML. This phenomenon explains the maximum coverage of 0.5 ML of atomic hydrogen ( $H_{ad}$ ) achieved when introducing hydrogen gas. In the existing literature, it is well-established that while hydrogen coverages up to 1 ML remain energetically favorable, the adsorption energy of hydrogen on this surface is coverage-dependent where it decreases approximately 0.12 eV around  $\theta = 0.5$  ML. To overcome the kinetic limitation of achieving a hydrogen coverage of 0.5 ML, an experimental approach employing a hot tungsten filament is utilized. The tungsten filament creates hydrogen atoms and hot hydrogen molecules that increase the dissociative sticking probability and make it possible to obtain hydrogen coverages above 0.5 ML.

Our investigations of the co-adsorption system revealed that as the coverage of atomic hydrogen ( $H_{ad}$ ) on Co(0001) increases at low surface temperatures, the adsorption capacity of CO co-adsorbed with  $H_{ad}$  decreases. This decrease in CO adsorption showed a linear trend; however a single-site model is not sufficient to capture the complexity of CO-H co-adsorption, as the saturation coverages of the two adsorbates do not add up to unity with the single-site model. By considering adsorbate segregation into ad-islands, we were able to obtain a reasonable quantitative description of the correlation between  $\theta_H$  and  $\theta_{CO}$  values in our model system. CO and hydrogen form known structures within the islands but still get mutually influenced on adsorption. Our findings reveal that even on a fully saturated Co(0001) surface with  $H_{ad}$ , a significant amount of CO can still be adsorbed. In contrast, when the surface is saturated with  $CO_{ad}$ , minimal hydrogen adsorption occurs. This behavior can be attributed to the occupation of sites required for dissociative hydrogen adsorption by CO molecules or their inaccessibility due to neighboring CO molecules, thereby increasing the energy barrier for hydrogen's dissociative adsorption. Conversely, dosing hydrogen in the presence of a hot tungsten filament results into hot hydrogen atoms and molecules enabling them to overcome the dissociative adsorp-

tion barrier on Co(0001) surfaces pre-covered with CO.

The role of steps/kinks on CO and hydrogen co-adsorption was also investigated as a part of the research. We initially focus on studying the adsorption of hydrogen alone on the kinked Co(11 $\bar{2}$ 9) surface. Subsequently, we examine the co-adsorption of CO and hydrogen on the same surface. Our investigations demonstrate that the presence of steps and kinks on the close-packed surface plays a crucial role in facilitating both the dissociative adsorption and recombinative desorption processes, providing a barrierless pathway. The steps and kinks on the surface reduce the barrier for dissociative hydrogen adsorption, resulting in an increased sticking coefficient. Consequently, the dissociative sticking probability exhibits a direct correlation with the density of steps, whereby an increased step density leads to a gradual downward shift of the desorption peak. For the co-adsorption system we find that minimal hydrogen can adsorb on a CO-saturated kinked Co(11 $\bar{2}$ 9) surface similar to the flat Co(0001) surface. Additionally, under similar CO saturation coverage, no ordered structures are observed, indicating the absence of long-range ordering.

Although the importance of defects and undercoordinated sites in the dissociation of CO is widely acknowledged, there is ongoing debate regarding the specific nature of active sites responsible for CO dissociation—an essential step in FT synthesis. Therefore, we compare the CO dissociation behavior on the stepped Co(10 $\bar{1}$ 9) and kinked Co(11 $\bar{2}$ 9) surfaces to elucidate the reactivity of these two types of defect sites. Chapter 4 of this thesis focuses on a comparative analysis of the kinetics of CO dissociation on stepped Co(10 $\bar{1}$ 9) and kinked Co(11 $\bar{2}$ 9) surfaces. Our investigations reveal that the dissociation reaction exhibits a similar energy barrier on both stepped and kinked Co surfaces, approximately 110 kJ/mol. However, it is worth mentioning that defect sites on the surfaces can become blocked by atomic oxygen (O) and carbon (C), thereby hindering further dissociation. It was also found that both B5-A and B5-B sites are active for CO dissociation to the same extent on the stepped Co(10 $\bar{1}$ 9) surface. These findings provide valuable insights into the CO dissociation process on different surface structures of cobalt catalysts, highlighting the importance of step-edge sites and the potential limitations imposed by the presence of atomic oxygen and carbon species.

Throughout the thesis, a variety of different approaches have been combined during the investigation of each subject, such as UHV experiments and DFT modelling. While each approach has its own limitations, combining their results allowed for a comprehensive understanding of the catalytic problem. For instance, experimental data collected in the UHV chamber, such as TPD spectra, can be influenced by background desorption and may originate from different surface processes. On the other hand, DFT modeling offers the advantage of providing adsorption energies on a selected surface and facilitating a more detailed data interpretation. However, it should be noted that DFT has inherent inaccuracies, such as the inability to reliably predict CO adsorption sites and energies on transition metal surfaces, as well as van der Waals forces. Therefore, the validity of the results relies on obtaining

experimental confirmation. By combining experimental and theoretical approaches, a comprehensive understanding of the catalytic surface reaction at the molecular level can be achieved. Finding the right balance between simplicity and complexity in studying the target system poses an additional challenge. Investigating a flat Co(0001) surface allows for easier and more feasible acquisition of detailed catalytic information compared to studying stepped or defective cobalt surfaces, which better represent real catalyst nanoparticles. The situation is similar when a number of adsorbates are present on the surface. However, under FTS conditions, the cobalt catalyst surface would be covered with numerous adsorbates. To gain a comprehensive understanding of the more intricate dynamics, it is crucial to explore high coverage CO adsorption and CO dissociation in the presence of CO on stepped and kinked cobalt surfaces.

# Contents

<b>Summary</b>	<b>v</b>
<b>1 Introduction</b>	<b>1</b>
1.1 Fischer-Tropsch synthesis	2
1.2 The surface-science approach	4
1.3 Catalysts for the FT reaction	5
1.4 Scope and structure of this thesis	6
1.5 Abbreviations	8
<b>2 Research Methods</b>	<b>9</b>
2.1 Introduction	9
2.2 Single crystals and vacuum	9
2.2.1 Ultra High Vacuum Vessel	10
2.3 X-ray photoelectron spectroscopy (XPS)	13
2.4 Auger Electron Spectroscopy	14
2.5 Low Energy Electron Diffraction	15
2.6 Temperature Programmed Desorption	18
2.7 Work Function measurements	20
2.8 Reflection Absorption Infrared Spectroscopy (RAIRS)	23
2.8.1 Vibrational frequency and line shape of the infrared absorption bands	24
2.9 Abbreviations	27
<b>3 Influence of defect sites on CO adsorption at low coverage</b>	<b>29</b>
3.1 Abstract	29
3.2 Introduction	29
3.3 Experimental setup	31
3.4 Computational methods	33
3.5 Surface Structures	35
3.6 CO adsorption on flat and sputtered Co(0001)	37
3.7 CO desorption	40

3.8	Discussion . . . . .	44
3.9	Conclusions . . . . .	45
3.10	Supplementary Information . . . . .	46
3.10.1	TPD measurements . . . . .	46
3.11	Abbreviations . . . . .	48
<b>4</b>	<b>CO and hydrogen co-adsorption on Co(0001)</b>	<b>49</b>
4.1	Abstract . . . . .	49
4.2	Introduction . . . . .	50
4.3	Experimental . . . . .	51
4.4	Results and discussion . . . . .	52
4.4.1	CO adsorption on Co(0001) . . . . .	52
4.4.2	Hydrogen adsorption on Co(0001) . . . . .	54
4.4.3	Dosing CO on Co(0001) pre-covered with hydrogen . . . . .	56
4.4.4	Dosing H <sub>2</sub> on Co(0001) pre-covered with CO . . . . .	60
4.5	Summary and conclusions . . . . .	68
4.6	Abbreviations . . . . .	70
<b>5</b>	<b>CO and hydrogen co-adsorption on Co(11<math>\bar{2}</math>9)</b>	<b>71</b>
5.1	Abstract . . . . .	71
5.2	Introduction . . . . .	72
5.3	Experimental setup . . . . .	73
5.4	Results . . . . .	75
5.4.1	CO adsorption on Co(11 $\bar{2}$ 9) . . . . .	75
5.4.2	Hydrogen adsorption on Co(11 $\bar{2}$ 9) . . . . .	77
5.4.3	Dosing CO on Co(11 $\bar{2}$ 9) pre-covered with hydrogen . . . . .	78
5.4.4	Dosing H <sub>2</sub> on Co(11 $\bar{2}$ 9) pre-covered with CO . . . . .	82
5.4.5	Discussion . . . . .	85
5.4.6	Summary and conclusions . . . . .	86
5.5	Abbreviations . . . . .	88
<b>6</b>	<b>CO dissociation</b>	<b>89</b>
6.1	Abstract . . . . .	89
6.2	Introduction . . . . .	90
6.3	Experimental . . . . .	92
6.4	Results . . . . .	93
6.4.1	Barrier Estimation . . . . .	99
6.5	Discussion . . . . .	101
6.6	Conclusions . . . . .	104
6.7	Abbreviations . . . . .	105

<b>7</b>	<b>Conclusions</b>	<b>107</b>
7.1	Chapter 3 : Influence of defect sites on CO adsorption at low coverage	107
7.2	Chapter 4 and 5 : CO and hydrogen co-adsorption on Co(0001) and Co(11 $\bar{2}$ 9) . . . . .	108
7.3	Chapter 6 : CO dissociation . . . . .	110
7.4	Future Prospects . . . . .	110
7.5	Abbreviations . . . . .	113
<b>8</b>	<b>List of publications</b>	<b>115</b>
8.1	Publications within the scope of this thesis . . . . .	115
8.2	Publications outside the scope of this thesis . . . . .	115
8.3	Contributions by the author . . . . .	116
	<b>Bibliography</b>	<b>117</b>
	<b>Acknowledgments</b>	<b>131</b>
	<b>Curriculum Vitae</b>	<b>135</b>



# Chapter 1

## Introduction

As the world's population grows and per capita energy consumption increases, demand for energy continues to rise. Currently, a majority of the world's energy is derived from fossil fuels, which are a finite resource. Consequently, there is an urgent need to explore alternative methods of fulfilling the energy needs of the planet. Additionally, human activity has been shown to have a significant impact on the environment<sup>[1]</sup>. Burning fossil fuels like coal, natural gas and oil release large quantities of CO<sub>2</sub>, as well as other byproducts such as NO<sub>x</sub> and SO<sub>x</sub> and unburned hydrocarbons. Therefore, it is crucial to identify and develop sustainable sources that can meet our energy needs while minimizing environmental harm.

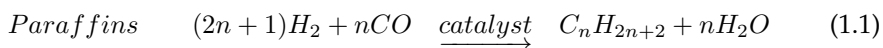
Research indicates a steady rise in global temperatures, a trend closely associated with increasing atmospheric concentrations of carbon dioxide (CO<sub>2</sub>), a primary greenhouse gas<sup>[2,3]</sup>. In response to the urgent need for emissions reduction, many industrialized nations have established ambitious targets and policies. For example, the European Union has committed to achieving net-zero emissions by 2050, with regulations promoting renewable energy use. Similarly, the United States has rejoined the Paris Agreement, aiming to keep global temperature rise well below 2°C—and ideally below 1.5°C—above pre-industrial levels by mid-century<sup>[4]</sup>. China, currently the largest emitter, has pledged to peak its emissions by 2030 and reach carbon neutrality by 2060. In the Netherlands, the energy transition has become a national priority, with goals to cut CO<sub>2</sub> emissions by 49% by 2030 and attain carbon neutrality by 2050. A combination of policies, including renewable energy subsidies and a carbon tax on fossil fuels, has facilitated the country's shift toward renewable energy sources. This highlights the importance of identifying and developing alternative, sustainable sources that can meet the world's energy needs. Fortunately, the sun offers an abundant source of energy that could potentially fulfill the world's energy needs. Various methods, such as solar cells, wind power, and biomass, can be employed to directly or indirectly harness this virtually limitless energy source. However, wind and solar energy present challenges stemming from

their inherent variability and intermittency, potentially affecting grid integration and stability due to the mis-match between their availability and demand. Cost-effective, high-capacity, and long-duration energy storage solutions is imperative to address these issues.

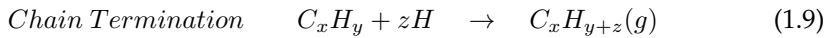
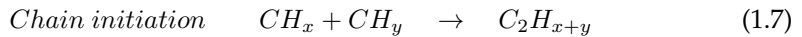
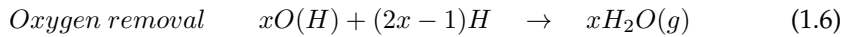
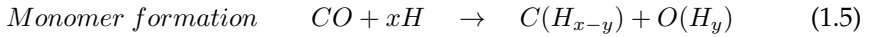
Despite the urgent need to cut carbon emissions, projections suggest that fossil fuels—including natural gas, coal, and petroleum—could still account for over 70% of global energy demand by 2040. This persistent use of fossil fuels is largely due to the relatively low cost of resources like coal in certain parts of the world, the availability of unconventional natural gas sources (such as shale gas), and advances in oil recovery technologies that make previously inaccessible reserves economically viable<sup>[5]</sup>. In light of this, interest is growing in alternative, sustainable carbon feedstocks to produce hydrocarbons with a lower environmental impact. Sustainable sources such as atmospheric CO<sub>2</sub>, agricultural and municipal waste, and green hydrogen (produced through renewable-powered water electrolysis<sup>[6]</sup>) offer promising pathways for renewable hydrocarbon production. Although converting renewable energy into hydrocarbons is generally less efficient than direct energy use, it remains valuable for long-term energy storage (e.g., from summer to winter), long-distance energy transport, and as an alternative for aviation fuels and critical chemicals in the chemical industry. In this context, Fischer-Tropsch Synthesis (FTS)—a process that generates long-chain hydrocarbons from CO and hydrogen—can play a crucial role in transforming renewable energy into chemical forms essential for diverse industrial applications.

## 1.1 Fischer-Tropsch synthesis

The first observation of the conversion of synthesis gas (a mixture of carbon monoxide and hydrogen) into methane on heated nickel was reported by Sabatier in 1902<sup>[7]</sup>. In the 1920s, Franz Fischer and Hans Tropsch further developed this process and showed that passing syngas over iron or cobalt below 300 °C can lead to the formation of higher hydrocarbons, now known as the Fischer Tropsch process<sup>[8-11]</sup>. The long chain hydrocarbons formed via FTS can serve as gasoline, diesel, and waxes. A broad range of C-containing feedstocks such as CO<sub>2</sub>, natural gas, biomass and coal can be used to derive synthesis gas, resulting in a flexible process that can be adapted to local resource availability<sup>[12]</sup>. FTS can generate high-quality fuels with low levels of impurities like sulfur and nitrogen-containing compounds, leading to cleaner burning fuels that emit fewer pollutants. The overall reaction equation for the formation of paraffins and olefins is shown below:



The catalyst facilitates the reaction by providing surface sites that offer a more energetically favorable path for the reactants to convert to products at a given temperature and pressure. To improve catalyst activity and selectivity, understanding of the kinetic aspects of this chain reaction, which encompass monomer formation, chain initiation, chain propagation and chain termination<sup>[13]</sup>, is crucial. The complex network of elementary reaction steps (listed below) in the FT reaction mechanism (eq. 1.1) begins with the adsorption and activation of H<sub>2</sub> and CO molecules (eq. 1.3 and 1.4), followed by chain growth of the monomer species (eq. 1.5), carbon-carbon coupling (eq. 1.7) and subsequent chain growth (eq. 1.8) steps to form longer chains, and hydrogenation and desorption steps to detach the final product (eq. 1.6 and 1.9).



The FT reaction exhibits a surface polymerization nature, whereby chain-growth monomers<sup>[14,15]</sup> are generated in situ. As a result, the products formed display a distribution of chain lengths, which in first approximation adheres to the well-established Anderson-Schulz-Flory (ASF) distribution<sup>[16-18]</sup>. The ASF distribution is characterized by a single parameter known as the chain growth probability ( $\alpha$ ), which is the probability that a growing intermediate will encounter a monomer and grow further (propagation) rather than desorb from the surface (termination). The growth probability is defined as follows where the rates of hydrocarbon chain propagation and termination are denoted by " $r_p$ " and " $r_t$ ", respectively:

$$\alpha = \frac{r_p}{r_p + r_t} \quad (1.10)$$

Traditionally, two operating modes of FT synthesis are identified based on the reaction temperature: low-temperature FTS (200-240°C) where either cobalt or iron-based heterogeneous catalysts are used to produce higher molecular weight products such as wax (high  $\alpha$ ) and high-temperature FTS (300-350°C) on iron-based catalysts for lower molecular weight (low  $\alpha$ ) products<sup>[19]</sup> such as gasoline and short chain olefins. A comparison of cobalt and iron catalysts suggests that cobalt is a good choice for the production of long-chain hydrocarbons in the low-temperature mode<sup>[20]</sup>.

## 1.2 The surface-science approach

The development of modern characterization techniques has made it possible to study catalysis at the atomic level, providing essential insights into active sites, adsorption mechanisms, and reaction pathways. Such atomic-scale understanding is critical for the design and optimization of catalysts. Surface science offers a unique opportunity to simplify the complexity of industrial catalysts by examining their structure, morphology, and reactivity under controlled conditions. This progress is largely due to advancements in ultrahigh vacuum (UHV) technology, which enables studies at pressures ranging from  $10^{-8}$  to  $10^{-10}$  mbar, and surface-sensitive techniques like X-ray photoelectron spectroscopy (XPS) that allow molecular-level investigations. However, because surface atoms comprise only a small fraction of the overall material, their signals are often weak compared to those of the bulk, complicating data interpretation. Additionally, surface contamination from the environment presents a challenge in modeling and acquiring reliable data on surface reactions. To address these issues, this study employs surface-sensitive techniques on single crystal surfaces to achieve an atomistic understanding of heterogeneous catalysis.

The use of UHV provides significant advantages for the fundamental study of catalytic processes, as surface contaminants can be removed in-situ and the surface remains clean for up to 1 hour afterwards. This allows for the study of clean metal surfaces instead of contaminated surfaces. However, this approach introduces the pressure gap, with the reactant pressures used in model experiments being orders of magnitude lower than those in actual catalytic processes under industrial conditions. Studies<sup>[21,22]</sup> at high CO pressures demonstrate that results obtained under UHV conditions at low temperatures on cobalt can extrapolate well into higher pressures and temperatures. At identical coverages, similar surface structures are observed that are independent of the surface temperature. Hence, by using low temperatures we can achieve similar coverages as under industrial conditions, hence obtaining relevant information on FTS. However, the low temperature needed introduces kinetic limitations and the contribution of entropy is comparatively lower. Therefore, we should always be cautious when extrapolating the results obtained from UHV and a single crystal surface to real catalytic processes.

In surface science, low-index single crystal surfaces such as Co(0001) are commonly used to study surface chemistry. However, this approach also introduces the so-called material gap as these models may not fully represent the surface chemistry occurring on real Co catalyst nanoparticles, which often have a large fraction of edge and corner atoms that are undercoordinated compared to the atoms on low index surfaces. These under-coordinated atoms can act as active sites due to the specific local atomic arrangements that contribute to the activity of the catalyst<sup>[23]</sup>. Previous research has suggested using high index, or vicinal surfaces<sup>[24]</sup>, which consist of terraces separated by periodically arranged monoatomic steps containing atoms

with a lower coordination number, to study the reactivity of these sites. This allows for monitoring of the local adsorption and dissociation behavior in the vicinity of under-coordinated atoms. This thesis studies on Co vicinal surfaces, which reveal clear differences in adsorption and dissociation of both CO and hydrogen between flat Co(0001) and vicinal Co surfaces.

### 1.3 Catalysts for the FT reaction

The catalytic activity and selectivity of the system are determined by the delicate balance between bond breaking and bond formation steps<sup>[25]</sup>. Transition metals to the left of the periodic table (eg. Mn) readily dissociate CO, but the atomic C and O formed bind too strongly with the surface, hindering further hydrogenation and coupling reactions. Metallic iron is too reactive, and it is its carbide phase that is considered to be most relevant for FTS<sup>[26,27]</sup>. Transition metals to the right of the periodic table (e.g. Ni) promotes more rapid hydrogenation thus leading to preferential formation of methane. Cobalt offers a good balance between the activation of reactant molecules and hydrogenation and C-C coupling reaction steps. It has a lower selectivity towards the water gas shift reaction as compared to Fe, resulting in a higher C hydrogenation efficiency<sup>[9]</sup>. Because cobalt is significantly more expensive compared to iron, the surface area to volume ratio is increased by making the cobalt particles very small, i.e. between 1-100 nm. These nanoparticles are then usually deposited on a porous high surface area support<sup>[28]</sup>.

Various researchers, such as Bartholomew<sup>[29]</sup> and Yermakov<sup>[30]</sup>, have investigated the impact of particle size on supported Co catalysts. Iglesia and colleagues conducted extensive studies and found that the surface-specific activity, referred to as Turnover Frequency (TOF), of cobalt particles within the size range of 9 to 200 nm is independent of particle size<sup>[31]</sup>, a conclusion supported by others<sup>[32,33]</sup>. However, for smaller cobalt particles (<10 nm), a decrease in FT performance has been observed. Barbier *et al.* reported a decline in TOF for cobalt particles smaller than 6 nm on a silica support<sup>[34]</sup>. Bezemer *et al.*, while utilizing cobalt on carbon nanofiber (CNF) catalysts tested at 1 and 35 bar, demonstrated that cobalt particles smaller than 6 nm (1 bar) or 8 nm (35 bar) exhibit significantly lower TOF compared to larger catalyst particles<sup>[32,35]</sup>. Moreover, these researchers noted an increase in methane selectivity alongside the decrease in TOF for smaller particles. Martinez and Prieto also observed a similar effect of particle size when they employed catalysts prepared via a colloidal route<sup>[36]</sup>. As a result, for Co nanoparticle catalysts, achieving high Fischer-Tropsch activity necessitates relatively larger metal particles (>6 nm)<sup>[37]</sup>. Different proposals have been made to explain this particle size effect. According to one viewpoint, small particles exhibit reduced reactivity due to the strong adsorption of CO, which hinders chain growth<sup>[14]</sup>. Other authors propose that step-edge sites, which are essential for promoting the chain growth reaction, are less abundant on

larger particles<sup>[38–40]</sup>. This observation suggests that larger particles lack the necessary step-edge sites required to drive the chain growth reaction. In both arguments, the structure of the catalyst particle and reactivity differences on different surface sites play an important role.

Theoretical and experimental studies have shown that CO<sup>[25,41,42]</sup> and hydrogen<sup>[43–45]</sup> dissociation require significantly lower activation energy on step sites compared to terraces, where reaction rates are approximately an order of magnitude lower. As a result, terrace sites are unable to compete with step sites in terms of reaction activity. Supported catalysts typically present a heterogeneous surface, consisting of terraces, steps, and kinks, with the relative proportion of these sites influenced by particle size and shape. Step-edge sites are formed by crystalline materials when one layer terminates, exposing the atoms of the underlying layer<sup>[46,47]</sup>. Atoms at the step-edge exhibit a lower coordination number (CN). Generally, smaller particles exhibit a higher density of steps and kinks, which can as described earlier, affect the elementary steps of the FTS reaction. To gain deeper insight into the role of step and kink sites in the initial reaction stages of FTS, this thesis systematically investigates the influence of surface structure on the early elementary steps of the FTS process.

## 1.4 Scope and structure of this thesis

In the context of a heterogeneous catalyst, the reaction proceeds through a sequence of events: the adsorption of reactants onto the catalyst surface, the interaction between adsorbed species, and the subsequent desorption of the resulting product. A heterogeneous catalyst can be conceptualized as a surface with a multitude of active sites and the adsorption process can be seen as the reaction between a vacant site and a molecule. The reactivity of a surface site varies as a function of surface structure, i.e. (1) the coordination number (CN), (2) the site's topology, and (3) the type of the metal - all affect the reactivity of a surface site. The CN denotes the number of nearest neighbors surrounding a surface atom. The topology is determined by the crystal facet type and the orientation of different facets relative to each other. The nature of the adsorbate bond that is activated, whether it be a  $\pi$  or  $\sigma$  bond, is dictated by the type of the metal catalyst and interaction with active site.

The goal of this thesis is to evaluate the influence of steps and kinks on the adsorption behavior of CO and hydrogen and their mutual interactions in the context of FTS. The motivation behind this study is to model the elementary reactions of FTS on well defined surfaces and under controlled conditions. The surface science experimental methods employed in this research include Temperature Programmed Desorption (TPD), Low Energy Electron Diffraction (LEED), Work Function (WF) measurements, and synchrotron-based X-ray Photoemission Spectroscopy (XPS). Computationally, Density Functional Theory (DFT) was applied to examine CO adsorption on the stepped and kinked Co surfaces, providing insights that are otherwise in-

accessible through experimental methods or complementing the experimental findings to strengthen conclusions.

Chapter 2 provides an introduction to the fundamental concepts and detailed information obtainable from the experimental techniques used in this study. It also covers the vacuum setup, single crystal surfaces, and the cleaning procedures employed to ensure reliable experimental conditions.

In chapter 3 of this thesis, we explore if CO adsorbs more strongly on the step sites of Co as compared to its terrace sites like other transition metals such as Pt and Rh<sup>[48,49]</sup> and hence has the potential to poison the step sites during FTS. After detailing the dissimilarities in atomic structures of flat Co(0001), stepped Co(10 $\bar{1}$ 9) and kinked Co(11 $\bar{2}$ 9) surfaces, we conduct a comparative analysis of molecular CO adsorption at low coverage on these surfaces to determine the influence of the steps and kinks on CO adsorption. This is achieved by using a combination of experimental and computational approaches. LEED and TPD techniques are employed to characterize the crystal structure of the clean and CO covered- cobalt surfaces and to provide insights into the desorption behavior of CO on these surfaces. XPS is used to not only corroborate the CO coverages on different surfaces obtained from the TPD experiments but also to differentiate between the CO adsorption sites based on the core-level binding energies of Co.

Since all elementary reaction steps in the FTS mechanism occur under high CO pressure, CO is expected to significantly influence the behavior of other reactants and products on the catalyst surface. Chapters 4 and 5 explore this in detail, examining the interplay between CO and hydrogen adsorption on both flat Co(0001) and kinked Co(11 $\bar{2}$ 9) surfaces under UHV conditions. By using low temperatures, these studies aim to replicate the high surface coverage conditions typical of FTS reactions. Additionally, these chapters investigate co-adsorption phenomena (mixing, segregation, and compression) on a flat cobalt surface, and analyze how step edges and kinks modify these interactions on open surfaces. Chapter 4 studies CO and hydrogen adsorption on the flat Co(0001) surface at high coverage proposing a co-adsorption model. The study explores two dosing sequences: hydrogen adsorption followed by CO, and CO adsorption followed by hydrogen adsorption, highlighting differences in adsorption behavior based on the sequence. Chapter 5 delves into the dissociative adsorption of hydrogen and the effect of CO on this process on the kinked Co(11 $\bar{2}$ 9) surface. Additionally, it explores the interactions between adsorbed CO and hydrogen atoms, aiming to understand how lateral interactions influence their adsorption on kinked Co sites during FTS. This chapter experimentally examines how lateral interactions vary with surface structure by comparing the kinked Co(11 $\bar{2}$ 9) surface to the flat Co(0001) surface.

Chapter 6 investigates the reactivity of different surface defects, specifically steps and kinks, in facilitating CO dissociation, and how various stepped sites differ in their reactivity. A kinetic model, which incorporates temperature effects, is employed to simulate experimental data and estimate reaction barriers, allowing a com-

parison of the reactivity between stepped Co(10 $\bar{1}$ 9) and kinked Co(11 $\bar{2}$ 9) surfaces. Work function measurements were used to determine the surface coverages of CO and O during the CO dissociation experiments and AES was used to study the surface composition after CO dissociation. Chapter 7 summarizes the key results and conclusions drawn from the thesis. It includes a broader discussion on the implications of these findings for industrial catalysis, particularly under FTS conditions. Finally, potential directions for future research are outlined, building on the insights gained from this study.

## 1.5 Abbreviations

- |             |                                       |
|-------------|---------------------------------------|
| 1. FTS      | Fischer-Tropsch Synthesis             |
| 2. CN       | Coordination number                   |
| 3. CNF      | Carbon nanofiber                      |
| 4. TOF      | Turn over frequency                   |
| 5. XPS      | X-ray photoelectron spectroscopy      |
| 6. UHV      | Ultrahigh Vacuum                      |
| 7. $\alpha$ | Chain growth probability              |
| 8. $r_p$    | Rate of hydrocarbon chain propagation |
| 9. $r_t$    | Rate of hydrocarbon chain termination |

# Chapter 2

## Research Methods

### 2.1 Introduction

This chapter details the theoretical and practical aspects of the techniques and describes the experimental set-up used in the present thesis. Details specific to the experiments in various chapters will be described in the chapter itself.

### 2.2 Single crystals and vacuum

The experimental work in this thesis has been carried out using cobalt single crystal surfaces which serve as structurally well-defined model catalysts to investigate the elementary steps of Fischer-Tropsch synthesis reaction. Single crystal refers to a solid which has a continuous crystal lattice across the entire sample with no grain boundaries. Single crystal surfaces expose well-defined sites with known atomic arrangement which enables study of the influence of the atomic structure on reactivity. Bulk cobalt has a hexagonal close packed (HCP) structure with a unit cell that is depicted in fig. 2.1. The axes of the primitive unit cell are  $a_1 = a_2 \neq c$ , which for cobalt are  $a = 2.5071 \text{ \AA}$  and  $c = 4.0695 \text{ \AA}$ . The unit cell contains three close-packed planes in an ABA stacking. The coordination number for a given atom in the ideal close packed structure is 12<sup>[50]</sup>. Planes within the unit cell are denoted using the Miller-Bravais notation  $(h, k, i, l)$ , where  $i = -(h+k)$ , which corresponds to the vector normal to the plane. Three different cobalt surfaces were used in the present work. The Co(0001) surface corresponds to the close-packed layer within the unit cell in which all atoms are identical and have a coordination number of 9. The Co(10 $\bar{1}$ 9) and Co(11 $\bar{2}$ 9) surfaces (depicted in Fig. 2.1) are vicinal and expose monoatomic steps separated by a close-packed terrace where the two differ by the width of the terrace as well as by the structure of the steps. Their structure will be discussed in more detail in chapter

3 of this thesis. We have also used the Co(11 $\bar{2}$ 0) surface for comparison, the details of which can be found in the work of Strømsheim et al.<sup>[51]</sup>.

Ultrahigh vacuum (UHV) is necessary to perform measurements on the surface without significant contamination from residual gases in the chamber. The rate of surface contamination is dependent on the impingement rate of gas molecules on the surface. The impingement rate per unit surface area can be derived from the kinetic theory of gases and is given by

$$\frac{\phi}{N_A} = \frac{P}{\sqrt{2\pi MRT}} \quad (2.1)$$

where  $N_A$  is Avogadro's number (number of molecules per mole),  $P$  is the pressure of the gas,  $M$  is the molar mass of the gas,  $R$  is the universal gas constant, and  $T$  is the absolute temperature.

The Langmuir (L) unit ( $1L = 1.33 \times 10^{-6}$  mbar s $^{-1}$ ) is derived as a useful measure which gives approximately 1 ML when the sticking coefficient is unity. That is if the sticking coefficient is 1 and the surface site density is  $1 \times 10^{15}$  cm $^{-2}$ , exposure of the surface to  $1.33 \times 10^{-6}$  mbar gas for 1 second would result in a surface completely covered with adsorbates whereas exposure to  $1 \times 10^{-10}$  mbar it would require 2.7 hours to completely cover the surface. Therefore, at a base pressure of  $1 \times 10^{-10}$  mbar the cleaned single crystal surface would stay clean of unwanted contaminants for a significant amount of time which allows us to precisely control the surface composition by dosing small amounts of known gas and perform detailed coverage-dependent studies.

### 2.2.1 Ultra High Vacuum Vessel

The temperature programmed desorption (TPD), Low energy electron diffraction (LEED), work function and infrared (IR) experiments reported here were performed in a home-built stainless steel UHV chamber with a base pressure of  $1 \times 10^{-10}$  mbar. The pressure of the analysis chamber is monitored by an ionization gauge (Varian XGS-600). The system is equipped with a sputter gun (PSP Vacuum Tech ISIS 3000), reverse-view four grid retractable LEED / Auger optics (Vacuum microengineering Inc.) and a UHV Kelvin Probe (KP Technology – DCV series 10). Chemical identification of the gases inside the chamber and TPD analysis are performed by a quadrupole mass spectrometer (QMS – Pfeiffer Vacuum QME 200) that probes the gas composition in the main chamber, and a second QMS (Hiden HAL 301) located in a separately pumped compartment which has a 5 mm aperture to sample the gas desorbing from the sample. Reflection absorption infrared spectra (RAIRS) were obtained using a Fourier-Transform infrared spectrometer (Perkin Elmer Frontier) equipped with a KRS-5 wire grid polarizer to selectively detect p-polarized compo-

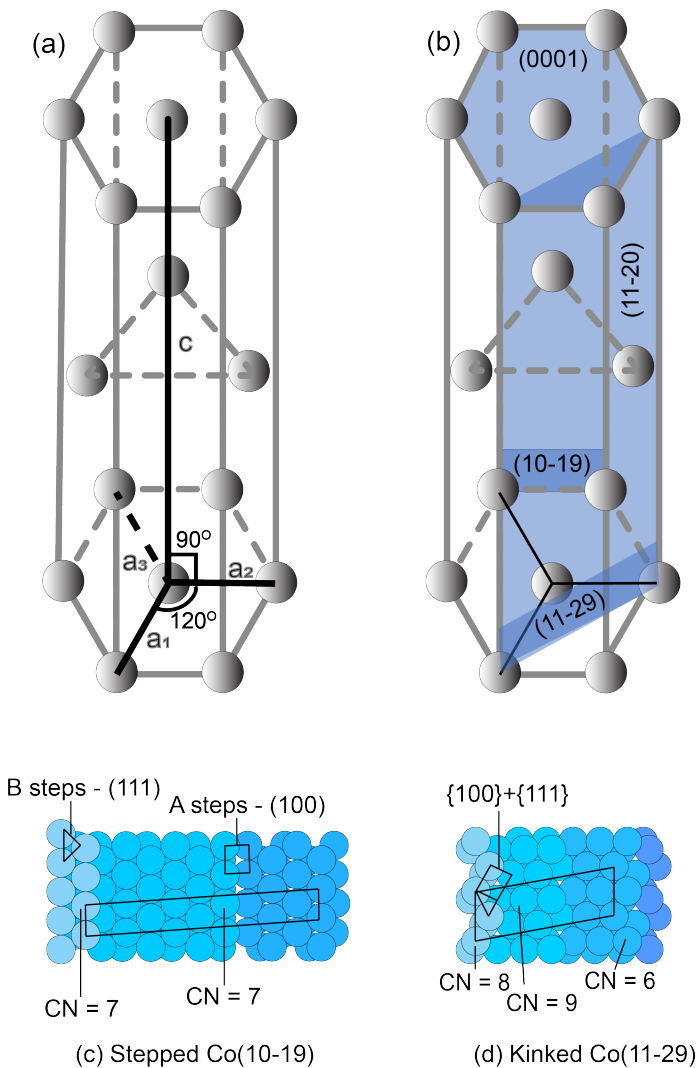


Figure 2.1: The hcp crystal structure with Co(0001), Co(10 $\bar{1}$ 9) and Co(11 $\bar{2}$ 9) planes indicated. Ball models of Co(10 $\bar{1}$ 9) and Co(11 $\bar{2}$ 9) surfaces optimized using DFT are shown as well.

ment of the light. A mercury cadmium telluride (MCT) detector was used with a spectral range of 4000-450  $\text{cm}^{-1}$ . The spectra shown in this thesis were recorded using a spectral resolution of 4  $\text{cm}^{-1}$  and the signal from the clean sample was used as the background. An average of 256 scans is typically shown whereas an average of 30 scans was used for time-resolved experiments. Each experiment was repeated several times to verify reproducibility.

Co single crystals of diameter – 8 mm and thickness – 1.2 mm (Surface preparation laboratory, 4 N purity), were cut and polished to within  $0.1^\circ$  of the desired orientation. Details of the Co(11-20) surface can be found in Strømsheim et. al.<sup>[51]</sup>. Two single crystals were mounted together on opposing sides of a rotary manipulator so that the switch from one sample to the other could be made within minutes, without breaking the vacuum. Both crystals were clamped by a u-shaped tungsten wire (0.5 mm dia) placed in two slits (width – 0.51 mm) on either sides of the crystal. Sample heating was achieved by passing a direct current through the support wire. Sample temperature was measured using a chromel-alumel thermocouple spot-welded to the backside of the sample close to the center. Liquid nitrogen (Linde) cooling of the crystal was done to reach a temperature of around 97 K while the sample was resistively heated to temperatures up to 670 K maximum to avoid the hcp-fcc phase transition which occurs around 690 K<sup>[52]</sup>. The heating rate could be controlled using a Eurotherm temperature controller. Typical heating rates that were used range from 0.1 to 2  $\text{Ks}^{-1}$ .

Sputtering removes the outermost atomic layers of the sample and in this way produces a clean surface. However, when done at room temperature it leads to a rough surface. Annealing heals the surface defects, but Co samples cannot be annealed at high temperature to avoid hcp-fcc phase transition (690 K). An alternative approach of sputtering at elevated temperature is adopted. This results in a smoother surface since annealing takes place during sputtering itself compared to when the surface is sputtered at room temperature and followed by annealing. Following this procedure, sample cleaning was done by bombarding the sample with 0.5-1 keV  $\text{Ar}^+$  ions (sputtering) at 670 K followed by annealing in vacuum at 670 K. Annealing the sample in an oxygen atmosphere ( $<1 \times 10^{-7}$  mbar) for a short amount of time (minutes) was also performed to remove carbon. Residual levels of atomic oxygen could be removed if there was also residual carbon present, through heating the surface to 670 K. If enough carbon was not present to react with the oxygen, additional<sup>[53]</sup> sputtering of the surface was required.

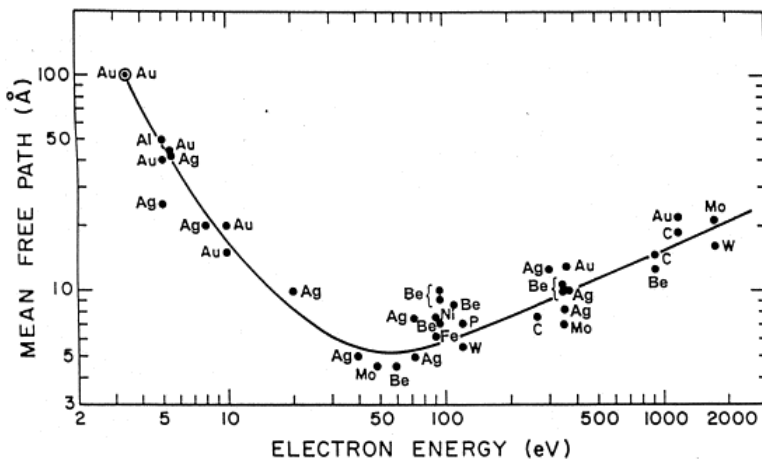


Figure 2.2: The mean free path of an electron depends on its K.E. and determines how much surface information it carries. Optimum surface sensitivity is obtained with electron in the 25-200 eV range. (Adapted from<sup>[55]</sup>)

## 2.3 X-ray photoelectron spectroscopy (XPS)

XPS (core level spectroscopy) is a quantitative technique used to determine the elemental composition of the outermost 1-10 nm of the sample. The technique is based on the photoelectric effect, where an electron is emitted upon the absorption of photons with sufficient energy. The minimum photon energy needed to release photoelectrons is the binding energy. Since the light is quantized, the remaining energy of the photon transforms into kinetic energy of the photoelectron. The binding energy is different for each core-level and is element specific. Different local chemical environments cause small variations in binding energy which can be detected and allow distinguishing different chemical states of the atoms. In our work, we typically use soft X-rays so that the kinetic energy of the photoelectrons is low. Low energy electrons strongly interact with matter so that only those created at or close to the surface-vacuum interface can escape from the sample and reach the detector. The attenuation length of the electrons, which characterizes how the signal of non-elastic electrons decreases with the distance they travel in solid, has a minimum of  $\sim 10$  Å (the exact value depends on the material) at kinetic energy of  $\sim 100$  eV. As a result, the XPS measurements are surface sensitive (fig. 2.2). A more detailed discussion of XPS can be found elsewhere<sup>[54]</sup>.

All XPS measurements in this work have been carried out at synchrotron facilities. The use of high brilliance light from the storage rings makes it possible to get high photon flux ( $\sim 10^{11}$  photons  $s^{-1}$ ), high-energy resolution of the X-ray photons, and the ability to choose the photon energy. The photoemission spectra have been

recorded in normal emission. Since the photon energy is not fixed, a typical experimental approach is to plot XP spectra as a function of binding energy instead of the kinetic energy of the photoelectrons even though kinetic energy is the parameter that is in fact measured. The binding energy is calculated by measuring the Fermi edge using the same photo-electron energy as that used for measurement of the actual spectra. In this way, uncertainties about the exact photon energy and the work function of the spectrometer cancel out. It is derived from the kinetic energy using the following equation.

$$E_k = h\nu - E_b - \phi_{sample} \quad (2.2)$$

where  $\phi_{sample}$  is the work function of the sample (eV),  $h\nu$  is the photon energy and  $E_b$  is the binding energy of the photoelectron with respect to the Fermi level of the sample (eV) and  $E_k$  is the kinetic energy of the emitted electron (eV). The binding energy contains information about the chemical identity of the photoionized atom while differences in chemical environments give rise to so-called chemical shift which provides further information.

Fig. 2.3 provides an illustration of how XPS can be used. It shows a C1s core level spectrum of CO adsorbed on Co(0001) at 100 K, obtained at a synchrotron with photon energy of 380 eV. CO adsorbed on top and bridge sites of the flat Co(0001) surface result in peaks at 285.5 eV and 285.0 eV, respectively<sup>[56]</sup> yielding a chemical shift of 0.5 eV. This means that the two carbon peaks result from two different chemical species. The area under the peak can be used to determine the number of molecules adsorbed on the two sites.

## 2.4 Auger Electron Spectroscopy

The Auger effect is a process in which an incident electron or photon causes emission of a core-electron thereby creating a hole in a deep core level. This hole is filled by a second electron from a higher core-level or valence shell with release of energy equal to the difference between the core hole and the parent higher core-level. This energy can be transferred to kinetic energy of a third electron, the so-called Auger electron. Its kinetic energy is related to the energy levels in the atom making it element specific. The energy can also be dissipated in form of a photon which can be used for e.g., energy dispersive x-ray analysis (EDX) in electron microscopes. In practice, we measure the kinetic energy of the Auger electrons by using LEED optics as a retarding field analyzer. Auger electron spectroscopy is a surface sensitive technique since the energy of the Auger electrons is typically 50 – 1500 eV which translates to 0.5 – 5nm of the mean free path of the electrons (see fig. 2.2).

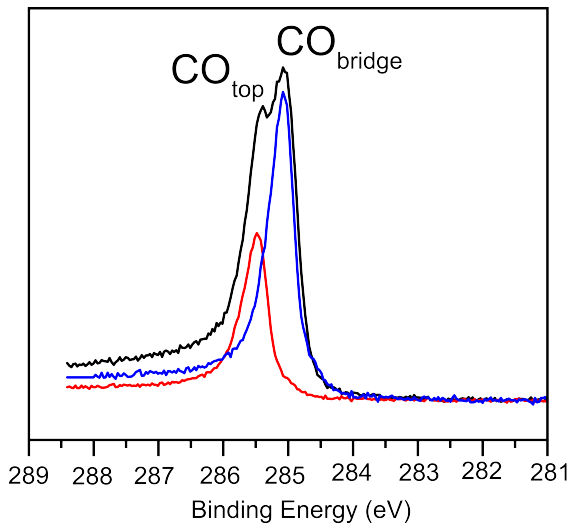


Figure 2.3: C1s spectrum of Co(0001) covered with CO. The red and blue peaks result from deconvolution of the C1s spectra after linear background subtraction.

AES peaks are a small signal on top of a large background signal and a lock-in amplifier is often used to measure the derivative of the signal, where the peak-to-peak ratio is taken as a quantitative measure of the concentration<sup>[57,58]</sup>. To approximate compositional analysis we can use relative sensitivity factors which are supplied with most Auger data processing software<sup>[59]</sup>. The mole fraction  $x_A$  of a component A in a binary mixture of A and B is given by :

$$x_A = \frac{\frac{I_A}{s_A}}{\left(\frac{I_A}{s_A}\right) + \left(\frac{I_B}{s_B}\right)} \quad (2.3)$$

Where  $I_x$  is the peak intensity and  $s_x$  the sensitivity factor of the relative element. In the present work we instead use a known reference state to calculate surface coverages, as this approach eliminates uncertainties in the sensitivity factors. Fig. 2.4 shows an example of Auger spectra used to calculate the amount of C on Co(11 $\bar{2}$ 9) surface. The peak intensities of C and Co are compared with the C and Co peaks in the reference spectra ( $\theta_C = 0.5\text{ML}$ ) obtained on Co(0001).

## 2.5 Low Energy Electron Diffraction

Low energy electron diffraction (LEED) is a surface sensitive technique used to determine the surface structure of crystalline materials. A beam of low energy electrons (< 200 eV) is scattered from the surface and a diffraction pattern is formed on a flu-

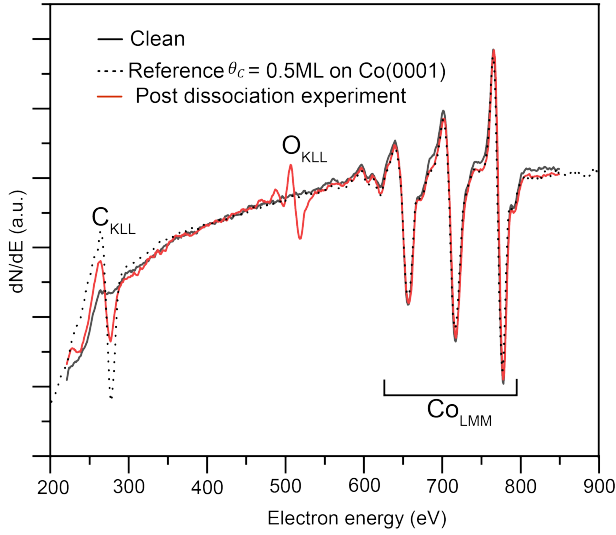


Figure 2.4: Auger spectrum of Co(11 $\bar{2}$ 9) covered with atomic C and O. The black spectrum was obtained on the clean Co(11 $\bar{2}$ 9) surface whereas the dotted spectrum obtained on Co(0001) covered with  $\theta_C = 0.5\text{ML}$  is used as a reference to determine the C coverage on Co(11 $\bar{2}$ 9)

orescent screen after filtering out inelastically scattered electrons. For electrons with low kinetic energy, the penetration is only a couple of atomic layers without losing energy (see fig. 3.2). The elastically reflected electrons carry information only from the outermost layers of the surface. The deeper the electrons penetrate the less they contribute to the diffraction pattern. This makes LEED highly surface sensitive. To obtain clear LEED patterns, the single crystal surface must be clean, free from unwanted compounds and well-ordered<sup>[60]</sup>.

In this thesis, LEED was used in qualitative manner where only the relative spot positions are evaluated. These positions provide information about the size, geometry and orientation of the adsorbate unit cell relative to that of the substrate. The LEED pattern shows the reciprocal lattice. If the 2D substrate surface lattice is expressed by a pair of two basis vectors  $(\vec{a}_1), (\vec{a}_2)$  spanning the unit cell, and the reciprocal lattice is expressed by  $(\vec{a}_1^*), (\vec{a}_2^*)$ , then the reciprocal lattice vectors are related to the real-space lattice vectors through :

$$\vec{a}_1^* = 2\pi \frac{(a_2 \times n)}{(a_1 \cdot a_2 \times n)} \quad (2.4)$$

$$\vec{a}_2^* = 2\pi \frac{(a_1 \times n)}{(a_1 \cdot a_2 \times n)} \quad (2.5)$$

where  $n$  is a unit vector perpendicular to the surface. Adsorbates on a single crys-

tal often form ordered overlayers with a unit cell that is different from the substrate unit cell so that it can be identified using LEED. From the adsorbate-induced diffraction spots the symmetry and rotational alignment of the superstructure with respect to the substrate can be determined. The adsorbate super lattice represented by  $\vec{b}_1, \vec{b}_2$  are related to the primitive translation vector of the substrate,  $\vec{a}_1, \vec{a}_2$  by :

$$\begin{pmatrix} \vec{b}_1^* \\ \vec{b}_2^* \end{pmatrix} = \vec{G} \begin{pmatrix} \vec{a}_1^* \\ \vec{a}_2^* \end{pmatrix} \quad (2.6)$$

Where G is 2x2 matrix relating the adsorbate and substrate meshes<sup>[61]</sup>. The LEED structures in this work are expressed using Wood's notation. In Wood's notation the lengths of  $\vec{b}_1$  and  $\vec{b}_2$  are given as simple multiples of  $\vec{a}_1$  and  $\vec{a}_1$  followed by the angle of rotation of  $\vec{b}_1$  from  $\vec{a}_1$ , ex.  $\sqrt{3} \times \sqrt{3} R30^\circ$  is the structure that 0.33 ML CO forms on Co(0001)<sup>[52]</sup>.

In the present work, single crystal surfaces with a regular array of steps and kinks were used as models to represent specific facets of a catalyst nanoparticle. The nature and concentration of steps and kinks can be controlled by varying the cutting angle of a single crystal. As shown in the fig. 2.5, on the clean Co(0001), we observe a sharp hexagonal LEED pattern, while on the stepped and kinked single crystals, spot splitting characteristic of vicinal surfaces is observed. The splitting of LEED spots occurs due to finite width of terraces on the stepped surfaces and can be used to determine the average terrace size. The determination of the terrace width is explained using an example of the stepped Co(10 $\bar{1}$ 9) surface (fig. 2.5). The spot splitting can be understood as follows – the terraces are very narrow and out-of-phase with each other so that the domain size in one direction is very small. This would produce a large oval spot in the diffraction pattern. The steps on the stepped surface form a regular array which would produce a 9x1 pattern. In LEED, however, only the spots where the 9x1 pattern overlaps with the oval spots on the stepped surface are seen. This produces the doubly or triply split spots typically seen on stepped surfaces. The method developed by Van Hove and Somorjai states that the ratio of the Co-Co bond distance (a) to the step-step distance (b) should be proportional to the beam splitting distance ( $b^*$ ) over the distance between the nearest columns of spots ( $a^*$ )<sup>[62]</sup>.

$$\frac{L}{r} = \frac{(2a^*)}{(3b^*)} \quad (2.7)$$

Where L is the separation between equivalent step edges and r is related to the lattice constant, a<sup>[63]</sup>. For the Co(10 $\bar{1}$ 9) sample, the column-column ratio to measured beam splitting ratio (5.58) is approximately equal to the real space value (5.31). Therefore, the average terrace width is 5 Co atoms. The exposed low miller index plane (111) of metals with a fcc lattice has the same atomic arrangement as the closed packed hcp(0001) plane. Therefore, the step orientations found on fcc (111) surface can also be found on the hcp (0001). But, because of the ABA stacking of the hcp

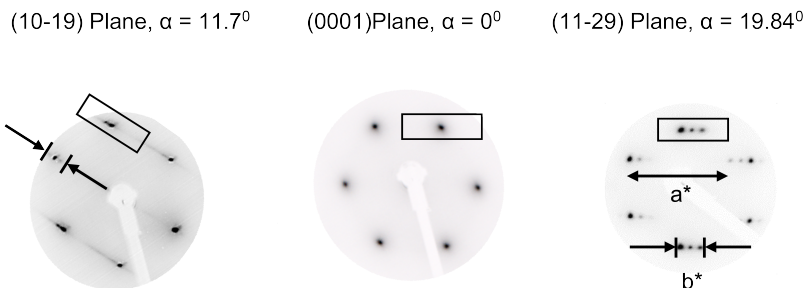


Figure 2.5: LEED images of clean Co( $10\bar{1}9$ ), Co(0001) and Co( $11\bar{2}9$ ) surfaces. The corresponding ball models of Co( $10\bar{1}9$ ) and Co( $11\bar{2}9$ ) are shown in fig. 2.1

lattice the structure of adjacent steps alternates and there exist two terraces between two equivalent step edges. As a result, the distance between two spots of the triply split spots<sup>[64]</sup> from the hcp surface would yield double the actual terrace width in real space. Thus, the distance  $b^*$  is taken as the distance between three consecutive spots on the hcp Co surfaces. We cannot completely exclude step doubling<sup>[65]</sup> from the LEED pattern alone. The LEED pattern of the sputtered surface show weak, broad spots at  $(1\times 1)$  positions which reflects the small size of the close-packed terraces after sputtering.

The direction of the splitting confirms that the step edges run along the  $[10-10]$  direction on Co( $10\bar{1}9$ ) along the  $[11-20]$  direction on Co( $11\bar{2}9$ ) and the average terrace width derived from the spot splitting, 1.25 nm (co atom rows) for Co( $10\bar{1}9$ ) and 0.75 nm for Co( $11\bar{2}9$ ), are close to the expected values. STM studies on flat and sputter-damaged Co(0001) typically show monoatomic steps that predominantly follow the  $\langle 10-10 \rangle$  directions of the substrate<sup>[66,67]</sup>. This is taken as evidence that step doubling on the Co( $10\bar{1}9$ ) surface is unlikely and the sample surface has the bulk-terminated structure.

## 2.6 Temperature Programmed Desorption

Temperature programmed desorption techniques are used to determine the kinetic (activation energy of desorption and pre-exponential factor) parameters of desorption or dissociation processes and to quantify adsorbate coverages. A schematic describing the TPD experiment is given in fig. 3.7. In the present work, the technique is applied in an UHV system where one or more chemical species desorb from a sur-

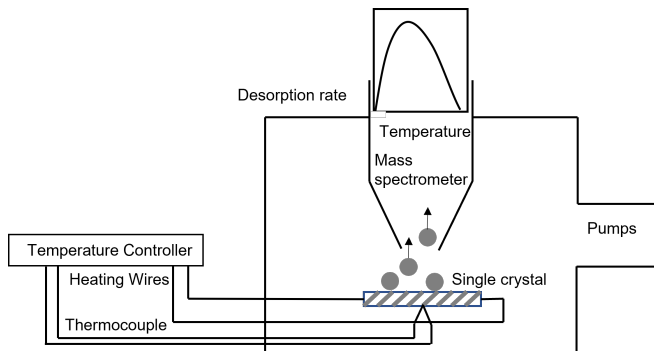


Figure 2.6: Scheme for experimental set-up for a temperature programmed desorption (TPD) experiment. The single crystal is heated by two heating wires pressed into the grooves at the side of the crystal, while the temperature is measured with a thermocouple at the back of the crystal and controlled by a PID controller. Desorption of gases from the surface is monitored by a mass spectrometer. A desorption trace is included. (Adapted from Niemantsverdriet<sup>[55]</sup>)

face during heating with a linear ramp rate ( $0.1 - 2 \text{ K s}^{-1}$ ). The heating induces either desorption or a surface reaction; known as TPD or temperature programmed reaction (TPR), respectively. The desorbing species are captured by a mass spectrometer (QMS). The sample surface is placed as close as possible to the entrance hole (0.5 cm dia) of the QMS compartment to ensure that the majority of what is evolved from the surface is measured by the QMS while contribution from degassing of the heating wires is minimized. The desorption temperature is indicative of the binding strength of the adsorbates to the surface and the signal strength is proportional to the partial pressure of the desorbing species and corresponds to the desorption rate. The surface coverage of the adsorbate can be back-calculated from the area under the desorption peak using a known reference system, e.g. the well-defined  $\sqrt{3} \times \sqrt{3} \text{ R}30^\circ$  - CO structure on Co(0001) with a coverage of  $1/3 \text{ ML CO}$ <sup>[52]</sup>. The rate of desorption of a species from a surface is often described by the Polanyi-Wigner equation<sup>[55,68,69]</sup>:

$$r_{des} = -\frac{d\theta}{dt} = k_d \theta^n = \nu_d(\theta, T) \theta^n e^{-\frac{E_a^{des}(\theta)}{RT}} \quad (2.8)$$

where  $r_{des}$  is the desorption rate,  $\nu_d$  is the pre-exponential factor,  $\theta$  is the surface coverage of the desorbing species,  $n$  is the reaction order of the desorption process,  $E_a^{des}$  is the activation energy of desorption, and  $T$  is temperature.

From this, it is possible to find the activation energy of desorption and the pre-exponential factor for an adsorbed species. The interpretation of the data and extraction of kinetic parameters from eq. (3.8) can be quite complicated, especially if the kinetic parameters, i.e. the adsorption energy and the pre-exponential factor are coverage dependent due to lateral interactions<sup>[70]</sup>. As a consequence, the Polanyi-Wigner equation can be an insufficient tool for the analysis of complex desorption data. A problem that often occurs is the compensation effect, where combination of

high pre-factor and high activation energy may give very similar rate of reaction as the combination of low pre-factor and low activation energy. Accurate determination of both pre-factor and activation energy requires a large data set over a broad range of coverages and heating rates. That is not always possible to obtain experimentally. A common approach to get an estimated barrier is the Redhead approximation, where the pre-factor is assumed, typically the range of  $10^{10}$  -  $10^{13}$   $\text{s}^{-1}$  depending on type of surface reaction<sup>[71,72]</sup>. The limitation of this method are the estimation of  $\nu_d$  and assumption of the coverage independent activation energy, which does not apply for adsorbates with strong lateral interactions. Alternatives to the interpretation by means of Polanyi-Wigner equation are based on the simulation of desorption spectra with complex statistical models for the interactions experienced by the adsorbate. Often so-called Monte-Carlo simulations are used<sup>[67]</sup>.

## 2.7 Work Function measurements

The work function is often sensitive to adsorbate coverage and in this thesis, we use it as a quick (1 s) measurement technique that gives indirect, but in-situ information on the adsorbate coverage that can also be used under (relatively) high pressures. We use this to derive kinetic information about the elementary steps of Fischer-Tropsch synthesis.

The work function is the energy that an electron needs to leave the highest occupied energy level of the metal (Fermi level) to the vacuum level<sup>[55]</sup>. It is the sum of chemical potential (bulk contribution) which is specific to the metal and the energy required to overcome the electrical double layer on the clean metal surface<sup>[73,74]</sup>. According to the Jellium model, the attractive potential due to the positively charged cores at the surface is not strong enough to keep the valence electrons inside the bulk<sup>[75]</sup> and the charge density spreads in the vacuum in a direction perpendicular to the surface. This induces a surface dipole with its negative end outside the metal. An electron travelling from the metal to the vacuum must surmount this dipole barrier as illustrated in the fig. 2.8. The size of the dipole depends on the surface structure so that the absolute work function varies with surface structure.

Adsorbates disturb the surface dipole and change the work function. Electron withdrawing species, such as CO and O on Co(0001), cause an increase in the work function by creating a negative dipole layer pointing away from the surface. The contribution of adsorbed layers to the work function is in first approximation expressed by the Helmholtz equation :

$$\Delta\phi = 2\pi P_A N_S \theta \quad (2.9)$$

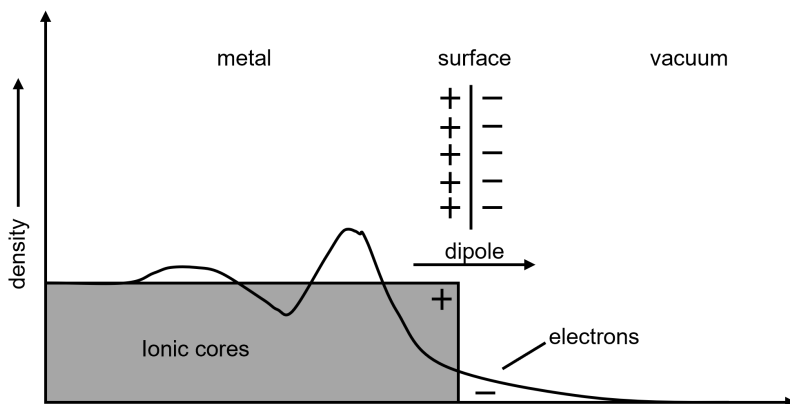


Figure 2.7: The electron distribution in the jellium model creates a dipole layer with the negative end to the outside of the metal surface (Adapted from Chorkendorff and Niemantsverdriet<sup>[76]</sup>)

where  $N_S$  is the number of adsorption sites per unit area,  $P_A$  is the dipole moment of the adsorbate and  $\theta$  is the fraction of occupied sites<sup>[56,77]</sup>. This equation implies a linearity of work-function change ( $\Delta\phi$ ) with the number of adsorbed molecules or coverage of adsorbates and typically a more complex coverage-dependent behavior is found. We can derive the coverage-dependent behavior by comparing with another quantitative technique such as TPD and, once the correlation is established we can derive the coverage directly from the work function data.

We used the vibrating capacitor method to measure the relative work function. It works on a contact potential difference between two metals in electrical contact, which is equal to the work function difference between two metals (sample and reference plate). If an external potential is introduced in series with the capacitor plates, the Fermi levels of two plates are equalized due to thermodynamic equilibrium. The charge flows from one plate to the other and the plates become equally and oppositely charged. The potential difference between the plates or the contact potential difference is the difference between the work function of the two metals. If a back potential ( $V_b$ ) is applied in the external circuit to restore the initial condition, then this back potential gives the work function difference between the sample and reference plates. If the work function of the reference plate remains constant, then the back potential will show the relative work function of the sample plate. This phenomenon is illustrated in fig. 3.9.

The vibrating capacitor method was first developed by Lord Kelvin in 1898 and the improvements to the method led to the development of Kelvin probe method. As the distance between the plates is changes, the capacitance between the plates

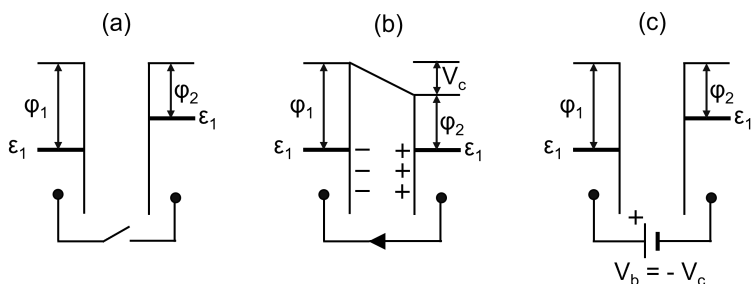


Figure 2.8: The electron energy diagram for two conducting materials,  $\phi$  and  $\epsilon$  represent the work function and the Fermi level of the materials, respectively. (a) The plates are isolated and charge free (b) The plates are connected electrically, which equalizes the Fermi levels of the materials and induces a charge transfer from one plate to another. As a result, a potential gradient or contact potential,  $V_c$  is produced. (c) Applying a back potential,  $V_b$  which is equal to  $V_c$  restores the initial condition. (Adapted from Woodruff and Delchar<sup>[56]</sup>)

also changes by

$$C = \frac{\epsilon A}{d} \quad (2.10)$$

where  $C$  is capacitance,  $\epsilon$  is permittivity,  $A$  is the surface area of parallel plates and  $d$  is the distance between plates. Varying the capacitance causes the potential difference between plates to vary as

$$C = \frac{Q}{V} \quad (2.11)$$

where  $Q$  is the charge on the plates and  $V$  is the potential difference between the plates. If an external potential is introduced in series with the capacitor plates with equal magnitude and opposite sign to the contact potential difference, then the net charge on the plates becomes zero and no potential occurs even if the reference plate is vibrated. At this point, the external potential or back potential gives the work function difference between the sample plate and the reference plate and any change in the physical and chemical nature of the surface is reflected in the work function.

We have used a UHV kelvin probe device to in-situ monitor the work function change of Co(0001), Co(10 $\bar{1}$ 9), and Co(11 $\bar{2}$ 9) during adsorption and desorption of molecules and during surface reaction. Reactants were adsorbed at 100 K and the work function was measured continuously as the crystal was heated with a rate of 1 Ks<sup>-1</sup>. Concurrently, desorption products were monitored with a mass spectrometer. Resistive heating causes a potential gradient over the sample during heating which affects the work function measurements significantly. To compensate for this the sample was grounded via an adjustable resistor bridge so that the sample was

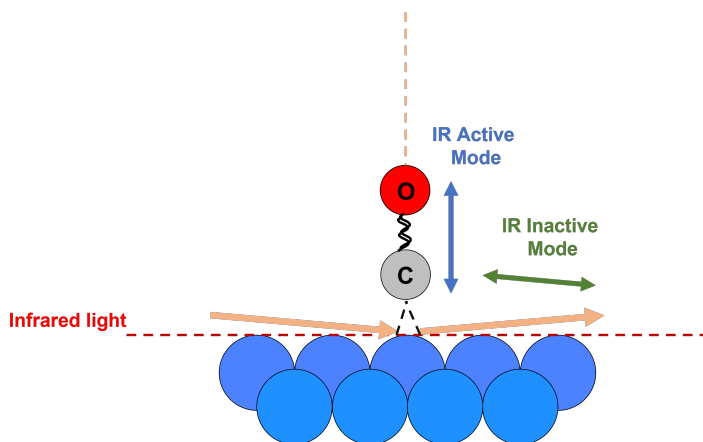


Figure 2.9: The principle of RAIRS: Infrared light is reflected near grazing angle from the crystal surface. Due to the surface dipole selection rule, only perpendicular component of p-polarized light can interact with an adsorbed molecule, exciting vibrations with a component perpendicular to the surface (Adapted from Çağlar<sup>[78]</sup>)

approximately at ground potential in the center. The resistors were adjusted such that a minimal offset of the work function was found during heating. With the aid of this arrangement, measurement were carried out with an accuracy of  $>50$  meV.

## 2.8 Reflection Absorption Infrared Spectroscopy (RAIRS)

RAIRS is a vibrational spectroscopy that is based on the interaction of infrared light with infrared active modes of adsorbed molecules as depicted in fig. 2.10. Molecules have specific frequencies at which they rotate or vibrate corresponding to discrete energy levels. Transitions between vibrational levels occurs by absorption of photons with frequency in the infrared range ( $10000 - 10 \text{ cm}^{-1}$ ). The C-O stretch vibration, for example, is at  $2143 \text{ cm}^{-1}$ . A measurement of the vibrational modes of adsorbed molecules can be utilized to identify them and to obtain details about the bonds in the molecule and between the adsorbed molecule and the surface.

A high surface sensitivity is achieved by reflecting the infrared radiation from the metallic sample surface with a low angle of incidence. The vibrational selection rule is that the molecular dipole must change during the transition<sup>[79]</sup> when stimulated by infrared light. The vibrating dipole of the adsorbate molecule is accompanied by an image dipole in the metal. A dipole vibrating normal to the metal surface gives rise to a parallel image dipole in the metal, which reinforces the molecular dipole. In contrast, a dipole vibrating parallel to the metal surface generates an antiparallel

image dipole in the metal surface, resulting in cancellation of the molecular dipole moment<sup>[80]</sup>. As a result, only dipole moments perpendicular to the surface are detectable, which means that only p-polarized light will be adsorbed by on a flat metallic surface.

An infrared spectrum shows the sample absorption as function of the wavenumber, expressed as absorbance or transmittance. The transmittance is defined as the ratio between the radiation intensity reflected from the adsorbate-covered sample ( $I$ ) and the clean sample ( $I_o$ ), the absorbance is the negative logarithm of the transmittance:

$$\text{Transmittance} = \frac{I}{I_o} \quad (2.12)$$

$$\text{Absorbance} = -\log\left(\frac{I}{I_o}\right) \quad (2.13)$$

Absorbance is used more often than transmittance because it varies linearly with the concentration of the adsorbate, whereas transmittance varies exponentially with the adsorbate concentration. Even though absorbance is better for quantification, effects like dipole-dipole coupling complicates quantitative analysis, as explained in the next section.

### 2.8.1 Vibrational frequency and line shape of the infrared absorption bands

In the present work RAIRS is used to study the C-O stretching mode of adsorbed CO, which is affected by adsorption on the surface and is sensitive to the exact adsorption site. Here we use CO adsorption on the Co(0001) surface as an example to discuss important phenomena in IR spectroscopy. Fig. 2.11 shows IR spectra obtained for different CO coverages on the close-packed surface.

The vibrational frequency of an adsorbed molecule on a metal surface differs from its value in the gas, liquid and solid phase or in an inert solid matrix due to several contributions. The vibrational frequency of absorbance can be calculated as a wavenumber using equation 2.14.

$$\nu = \frac{1}{2\pi c} \sqrt{\frac{k}{\mu}} \quad (2.14)$$

Where  $k$  is the force constant equal to the strength of C=O,  $c$  is the speed light and  $\mu$  is the reduced mass of the C=O system. A classical model used to rationalize this for CO adsorption is the Blyholder model<sup>[81,82]</sup>. This model takes into account

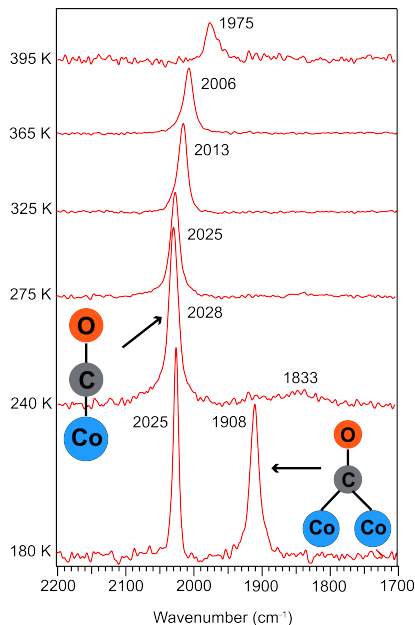


Figure 2.10: RAIRS spectra of CO adsorbed on Co(0001) at several temperatures

that the chemical bond between CO and metal is formed by a combination of charge transfer from the  $5\sigma$  MO of CO into the metal and by backdonation from metal d-bands into the unoccupied ( $2\pi^*$ )-MO of CO. Since the  $5\sigma$  MO is only weakly bonding and ( $2\pi^*$ )-MO strongly antibonding, the C-O bond is weakened by chemisorption as the amount of backdonation into ( $2\pi^*$ ) orbital increases. Filling of the bonding  $5\sigma$  MO contributes to the bonding of the adsorbate to the surface, but concurrently it weakens the internal bond of the adsorbate, resulting a lower frequency for the internal mode of the adsorbate.

The vibrational frequency of adsorbed molecules depends on the adsorption site and geometry<sup>[83]</sup>. For CO, the vibrational frequency is lowered for adsorption in higher coordination sites: CO on top sites is observed between 2100 and 2000  $\text{cm}^{-1}$ , CO on bridge sites is observed between 2000 and 1900  $\text{cm}^{-1}$  and CO in three and four-fold position is observed below 1900  $\text{cm}^{-1}$ <sup>[52]</sup>. The reason for that is also explained by the Blyholder model. When CO adsorbs in a higher coordination site (i.e. twofold bridge, threefold), the overlap between the LUMO of CO ( $2\pi^*$ ) and d orbitals of metal becomes higher, causing a lower CO stretching frequency for molecules bonded in a higher coordination sites<sup>[84]</sup>. This is clearly seen in fig. 2.11 in the spectrum after heating to 180 K, in which the frequency of CO on the top site (2015  $\text{cm}^{-1}$ ) is higher than that of CO on the bridge site (1908  $\text{cm}^{-1}$ ).

The vibrational frequency of adsorbed CO molecules also depends on the coverage due to intermolecular interactions: chemical interaction (e.g. repulsive interac-

tion) and vibrational coupling (or dipole-dipole coupling). The chemical interaction can be understood on the basis of the chemical shift described above. Dipole-dipole coupling is based on the fact that a vibrating molecule gives rise to a long range oscillations in the dipole field which is sensed by the other adsorbate molecules<sup>[85]</sup>. As a result, dipole-dipole coupling becomes effective, which leads to an increase in frequency of CO on the top site. This can be seen in fig. 2.11 where at high coverage (lower sample temperature) the peak corresponding to occupation of top sites is at  $2025\text{ cm}^{-1}$ . As CO coverage decreases by desorption from the surface during heating, the peak maximum is seen to shift to lower wavenumbers reaching  $1975\text{ cm}^{-1}$  at 400 K.

The intensity of an infrared band differs from one adsorbate to another and is proportional to the dynamic dipole moment of the adsorbed molecule. The intensity cannot directly be translated to a relative amount of adsorbed species by comparison. Moreover, the adsorption bands of a single adsorbate in different sites differ in intensity. A striking example can be seen in the data in fig. 2.11. On the basis of other techniques a top/bridge ratio of 1:6 was derived<sup>[86]</sup>, but the ratio of the IR peaks is around 1.33:1. The infrared band intensity of an adsorbate increases with coverage, but there is no linear relation between the intensity increase and the adsorbate coverage. At high coverage, the gradient of the intensity increase is reduced<sup>[87]</sup>. According to a model developed by Persson and Ryberg for CO adsorbed on a transition metal<sup>[85]</sup>, this is attributed to dipole-dipole coupling between adsorbed CO molecules. For larger molecules (i.e. hydrocarbon, oxygenates), the linear relation between the infrared band intensity for a specific mode of molecule and coverage can also be broken by the change in molecular orientation as the coverage increases. This follows from the surface selection rule stated above since only the component of dipole moment perpendicular to the surface contributes to the band intensity. Inhomogeneous broadening can be caused by an inhomogeneous distribution of individual oscillator frequencies determined by the adsorption site of molecules or inhomogeneity of the intermolecular distance (between adsorbates). For our study, it is sufficient to know that a well ordered adsorbate layer results in a narrow symmetric peak, while a broadened and asymmetric peak is expected for a distorted adsorbate layer. In summary, IR spectroscopy is good to gain qualitative insights on CO adsorption sites, but for quantitative interpretation it is best used in conjunction with another quantitative technique like XPS or TPD.

## 2.9 Abbreviations

1. DFT	Density Functional Theory
2. EDX	Energy dispersive x-ray analysis
3. HCP	Hexagonal close packed
4. IR	Infrared
5. KP	Kelvin Probe
6. L	Langmuir
7. LEED	Low energy electron diffraction
8. LUMO	Lowest unoccupied molecular orbital
9. ML	Monolayer
10. QMS	Quadrupole mass spectrometer
11. RAIRS	Reflection absorption infrared spectra
12. STM	Scanning tunneling microscopy
13. TPD	Temperature programmed desorption
14. TPR	Temperature programmed reaction
15. UHV	Ultrahigh Vacuum
16. XPS	X-ray photoelectron spectroscopy
17. A	Surface area of parallel plates
18. C	Capacitance (F)
19. M	Molar mass of the gas ( $\text{kg} \cdot \text{mol}^{-1}$ )
20. P	Pressure of the gas ( $\text{kg} \cdot \text{m}^{-1} \cdot \text{s}^{-2}$ )
21. Q	Charge (A.s)
22. R	Universal gas constant ( $\text{m}^3 \cdot \text{Pa} \cdot \text{K}^{-1} \cdot \text{mol}^{-1}$ )
23. T	Absolute temperature (K)
24. k	Force constant
25. c	Speed of light ( $\text{m s}^{-1}$ )

26. $\mu$	Reduced mass
27. $V_b$	Contact potential (V)
28. $V_b$	Back potential (V)
29. $d$	Distance between plates (m)
30. $\phi$	Work function (eV)
31. $\epsilon$	Fermi level of the material (eV)
32. $\epsilon$	Permittivity ( $F m^{-1}$ )
33. $N_A$	Avogadro's number
34. $E_k$	Kinetic energy of the emitted electron (eV)
35. $h\nu$	Photon energy (eV)
36. $E_b$	Binding energy of the photoelectron (eV)
37. $\phi_{sample}$	Work function of the sample (eV)
38. $I_x$	Peak intensity of x
39. $s_x$	Sensitivity factor of x
40. $x_A$	Fraction of component A
41. $b^*$	Beam splitting distance
42. $a^*$	Distance between the nearest columns of spots in LEED
43. $r_{des}$	Desorption rate
44. $\nu_d$	Pre-exponential factor
45. $\theta$	Surface coverage of the desorbing species (ML)
46. $E_a^{des}$	Activation energy of desorption ( $kJ mol^{-1}$ )
47. $N_S$	Number of adsorption sites per unit area
48. $P_A$	Dipole moment of the adsorbate
49. $\Delta\phi$	work-fuction change
50. $\text{\AA}$	Angstorm

## Chapter 3

# Influence of defect sites on CO adsorption at low coverage

### 3.1 Abstract

In studies aimed at understanding the chemical bonding of CO to metal surfaces in the context of Fischer-Tropsch synthesis, the influence of the crystallographic orientation is often considered critical. In this chapter, we examine CO chemisorption in the low coverage regime on defect rich Co surfaces and compare it with a flat Co(0001) surface. We provide experimental data on the adsorption of CO on different sites by identifying and quantifying the CO adsorbed on terrace and defect sites based on their respective core-level lines in XPS. The analysis of XPS and TPD results allows us to detect the undercoordinated site species and follow their thermal behavior to show weaker adsorption on the kink sites compared to the terrace sites of the kinked Co surface but with a similar strength on the step sites as the terrace sites on the stepped Co surface. Experimental evidence is combined with DFT calculations to provide fundamental insights into the lack of driving forces for CO induced surface reconstruction of Co nanoparticles.

### 3.2 Introduction

The conversion of CO and H<sub>2</sub> into long chain hydrocarbon molecules, Fischer-Tropsch (FT) synthesis<sup>[8,88]</sup>, over a heterogeneous catalyst is of great industrial and academic importance. Interest in FT synthesis has recently been revived due to demand for clean fuels for a carbon neutral society. Instead of traditional FT synthesis feedstocks (e.g. coal, oil, gas), sustainable carbon sources such as CO<sub>2</sub>, agricultural and municipal waste, combined with green hydrogen generated from water electrolysis

using renewable energy, presents a practical trajectory to a more sustainable future. The metals Fe, Co, Ru and Rh are known to be FT active. Of these Ru and Rh are too expensive, leaving only Fe and Co as the predominately used FT catalysts. Fe-based FT synthesis is generally performed at high temperatures with the catalytically active phase being iron carbides/oxides. Co-based catalysts are adopted for low temperature FT synthesis where metallic Co is the active phase. The application of metallic Co leads to higher selectivity toward long chain paraffins making it the preferred FT catalyst<sup>[9-11]</sup>.

For efficient atom utilization of the active metallic cobalt as well as high catalyst surface area per reactor volume, supported Co nanoparticles are used. These nanoparticles expose a range of surface terminations directly to the reaction atmosphere. The most stable crystallographic phases of metallic cobalt nanoparticles under FT-relevant synthesis conditions are the face-centered cubic (fcc) followed by the hexagonal close-packed (hcp) phase<sup>[89,90]</sup>. Wulff construction of both these phases show the presence of various surfaces with a wide range of coordination numbers for surface cobalt atoms<sup>[91]</sup>. Whilst the proportion of different catalytic sites on cobalt nanoparticle surfaces may depend on numerous factors, the role of defect sites has been placed at the center of CO activation in the FT synthesis process. Following CO activation, a complex network of elementary reaction steps are involved in the chain initiation and propagation. Defect sites are argued to be at the center of both the FT reaction activity as well as catalyst deactivation<sup>[14,92]</sup>.

The adsorption of CO on defect sites, is therefore of great importance in the quest to understand their role in FT synthesis. The adsorption of various atomic and molecular species on metallic surfaces has been shown to depend strongly on the electronic structure of adsorption sites and consequently on the coordination environment of such sites<sup>[93]</sup>. In some reaction systems, this relationship has often been cited in arguing that edge and defect sites are poisoned/ blocked by reaction intermediates<sup>[94-96]</sup>. In the case of FT synthesis, numerous experimental and theoretical studies<sup>[21,97-104]</sup> have been conducted to understand the adsorption and activation of CO on the flat cobalt surface, i.e. Co(0001), which represents over 65% of the available surface of hcp-Co nanoparticles<sup>[52]</sup>. On the contrary, steps and defect sites have mostly been explored using theoretical methods where they are often represented as high Miller-index surfaces. Aside from well-established challenges of local and generalized gradient density functional theory (DFT) methods in predicting accurately the adsorption energy and site preference of CO on metallic surfaces, there remains disagreement in the reported reactivity of defect sites compared to terrace sites. While some theoretical studies indicated stronger CO adsorption on defect sites of Co(10 $\bar{1}$ 6), when compared to the terrace sites<sup>[105]</sup>, more recent evidence on hcp Co(11 $\bar{2}$ 0) and Co(10 $\bar{1}$ 2) surfaces<sup>[25]</sup> and fcc Co(111), Co(100) and Co(110) surfaces<sup>[94]</sup> show strong CO adsorption on all Co surfaces with a weak dependence of

adsorption strength on the surface structure.

A typical consequence of strong adsorption of CO to the defect sites of metal nanoparticles is their reconstruction to more stable highly faceted particles. Co nanoparticles have been found to be more robust under the FT reaction conditions whereas Pt nanoparticles undergo reconstruction when exposed to high pressure of CO<sup>[94]</sup>. The adsorption strength of CO on metal surfaces as well as its bond stretching frequency have been explained using various models including the Blyholder model<sup>[81]</sup>. Based on the Blyholder model, the adsorption strength and CO stretching frequency are dependent on factors such as metal substrate, local coordination environment as well as surface coverage. This dependence is preserved in more recent models such as the d-band theory and its improved version<sup>[81,82,106]</sup>. The behavior of CO on one surface is unlikely to match that on a different surface due to differences in backdonation and/or hybridization energies.

Experimentally, Böller et al. did not observe significant reconstruction of a defect rich Co(0001) surface when exposed to atmospheric pressure of H<sub>2</sub>/CO gas mixtures at 500 K in STM. Weststrate et. al. also compared the CO adsorption strength on fcc and hcp Co surface and Co foils<sup>[107]</sup> and found that the CO desorption temperature that is independent of surface structure. Available experimental data is incomplete and scattered over different studies where the different experimental approaches used make comparisons difficult. Therefore, we present this work to develop an understanding of different CO adsorption sites on different facets under reaction conditions and comment on the adsorption strength on sites which can act as a driving force for surface reconstruction. We use single crystals as models of stepped and kinked facets available on a Co catalyst nanoparticle. We also study CO adsorption and desorption on the defect-rich Co surfaces and compare them with the flat Co(0001) surface on the basis of CO adsorption strength on different adsorption sites. The results show that CO prefers to adsorb more strongly to on-top sites but does not preferentially adsorb on the defect sites, a finding that is supported by the DFT simulations.

### 3.3 Experimental setup

Temperature programmed desorption (TPD), LEED, and Infrared (IR) spectroscopy experiments were performed in a home-built stainless steel UHV chamber with base pressure of  $1 \times 10^{-10}$  mbar as described in chapter 2 of this thesis. The chamber is equipped with a sputter gun, LEED/Auger optics (Vacuum Microengineering, Inc.), and two quadrupole mass spectrometers (QMS). The flat Co(0001) and one of the three high index surfaces - stepped Co(10 $\bar{1}$ 9) or kinked Co(11 $\bar{2}$ 9) or Co(11 $\bar{2}$ 0)<sup>[51]</sup> were mounted on an xyz manipulator with a rotary feedthrough in an identical manner

allowing switching between samples without breaking the vacuum. Both crystals could be heated by passing DC through a u-shaped tungsten wire (0.5 mm dia) which contacted the crystal through two slits (width - 0.51 mm) on opposite sides of the crystal. Sample temperature was measured using a chromel-alumel thermocouple spot-welded to the back of the crystal close to the center. The samples were heated to a maximum of 670 K to avoid the hcp-fcc phase transition (690 K). The tungsten wire was in thermal contact with a liquid nitrogen reservoir so that the lowest sample temperature can be reached in  $\sim 3$  min after sample annealing. The single crystals were prepared in vacuum by repeated cycles<sup>[52]</sup> of 1 kV Ar+ sputtering (15 min) and annealing (670 K, 15 min). The samples were cleaned at 300 K right after exposure to air followed by subsequent O<sub>2</sub> treatment (670K,  $1 \times 10^{-7}$  mbar, 5 min) and cleaning cycle (670 K) until the samples were clean. Sample cleanliness was checked by LEED/AUGER electron spectroscopy.

A QMS (Hiden HAL 301) is located in a separately pumped compartment with an aperture (dia - 5mm) that can be brought close in close proximity (2-3 mm) of the sample surface. This suppresses the signal due to desorption from other parts of the sample holder resulting in a background which is a straight line that can be reliably subtracted. The drawback of this arrangement is that the signal intensity is a function of the exact position of the sample relative to the aperture. As there were differences in positioning of the two samples, the shielded MS data was not suited for quantification of the CO coverage on the Co samples. Therefore, in order to determine the CO coverages, the samples were placed outside the line of sight of another QMS (Pfeiffer Vacuum QME 200) installed in the main chamber. This QMS functions as a residual gas analyzer and the signal intensity is insensitive to the sample position. The well-ordered ( $\sqrt{3} \times \sqrt{3}$ )R30° structure corresponding to 0.33 ML CO coverage that forms on Co(0001) at 320 K was used as a reference to calibrate the desorption peak areas of the other Co surfaces<sup>[51]</sup>. More details on this procedure are provided in the SI.

Reflection absorption infrared spectra (RAIRS) were obtained using a Fourier-Transform infrared spectrometer equipped with a KRS-5 wire grid polarizer to selectively detect the p-polarized component of the light. A mercury cadmium telluride (MCT) detector was used with a spectral range of 4000-450  $\text{cm}^{-1}$ . The spectra shown were recorded using a spectral resolution of 4  $\text{cm}^{-1}$  and the signal from the clean sample was used as a background. An average of 256 scans is typically shown whereas an average of 30 scans was used for time-resolved experiments. Each experiment was repeated several times to verify reproducibility.

High-resolution (HR) photoemission experiments on the well-annealed Co(0001) and sputtered Co(0001) surface were performed at the superESCA beam-line (ELETTRA, Trieste)<sup>[108]</sup> while the FlexPES beamline at MAXIV (Lund, Sweden) was used to

obtain medium resolution (MR) photoemission spectra on the Co(10 $\bar{1}$ 9), and Co(11 $\bar{2}$ 9) surfaces. All the photoemission experiments were carried out at normal emission. C1s core level spectra were taken using a photon energy of 380 eV and binding energies are reported with respect to the Fermi edge. Sample cleanliness was confirmed by photoemission experiments. For the XPS measurements at the SuperESCA beamline a Ta rod was spotwelded to the back of the sample and used to fix the sample to the manipulator. The thermocouple was spotwelded to the side of the sample. The sample was heated radiatively via two W filaments placed at the backside of the sample. At the FlexPES beamline, the samples were clamped onto a Ta flat plate by thin tantalum wires spotwelded to the sample plate and the thermocouple was directly connected to the sample. The as-measured temperatures in a temperature-programmed XPS experiment were compared with a TPD experiment performed with the same heating rate in the home laboratory and corrected for any discrepancy. Intensity and energy of different components of C1s spectra can be extracted by integrating the C1s signals following the subtraction of Shirley<sup>[109]</sup> background on the data collected at the SuperESCA beamline. For the data obtained at FlexPES the spectrum corresponding to the clean surface is subtracted. The C1s spectra corresponding to  $\theta_{CO} = 0.33$  ML was used to deconvolute the spectra obtained on heating the CO covered sputtered Co(0001), Co(10 $\bar{1}$ 9), and Co(11 $\bar{2}$ 9) surfaces.

### 3.4 Computational methods

Atomistic insights into the interaction of CO with various cobalt surfaces were obtained from spin-polarized density functional (DFT) calculations, using the Vienna Ab initio Simulation Package (VASP)<sup>[110,111]</sup> and an implemented vdw-DF exchange-correlation functional<sup>[112,113]</sup>. The latter was found to predict a correct adsorption site preference for CO on Co(0001) as well as a reasonably accurate adsorption energy, in contrast to standard DFT functionals<sup>[114–116]</sup>. The electronic and geometry optimization steps were converged to within  $10^{-5}$  eV and 0.01 eV/Å, respectively. The 2<sup>nd</sup> order Mathfessel-Paxton (MP) method<sup>[117]</sup> with a smearing width of 0.2 eV was used for all adsorbed state calculations. Dipole correction was applied along the surface normal in all slab calculations. The ground state electronic energies were extrapolated to zero smearing.

The adsorption energy of CO on each surface site was defined as,

$$E_{ads,CO} = E_{CO/Slab} - E_{Slab} - E_{CO(g)} \quad (3.1)$$

with  $E$  being the ground state electronic energy of CO adsorbed on a slab (CO/Slab), clean slab (slab) and gas phase CO (CO(g)). Furthermore, vibrational analysis calculations were performed using the finite differencing method in order to guide

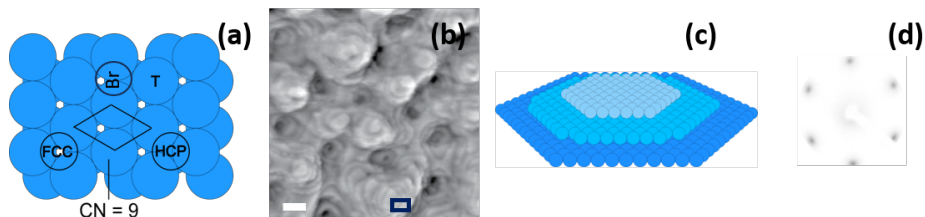


Figure 3.1: (a) Ball model of Co(0001), (b) STM image of sputtered surface adapted from Böller et al.<sup>[65]</sup>. The scale bar is 4nm. (c) ball model as perceived from (b) showing a section of (b) as represented by the blue rectangle (d) LEED of a clean sputtered surface. Blurred spots represent poor ordering of the surface atoms.

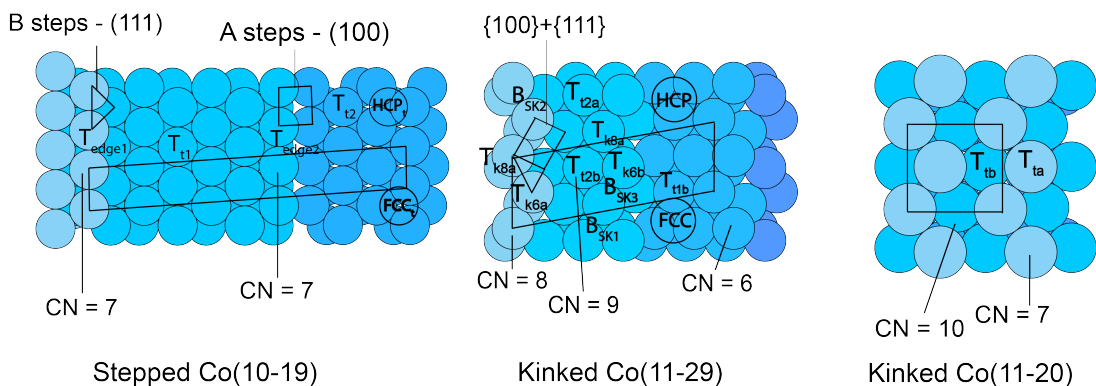


Figure 3.2: Ball model of Co( $10\bar{1}9$ ), Co( $11\bar{2}9$ ), and Co( $11\bar{2}0$ ) surfaces exhibiting A and B type steps and kinks. The coordination number of different atoms is indicated in the figure

assignment of experimentally measured IR absorption bands and related them to theoretically calculated adsorption states. Fig. 3.1 and 3.2 show the structure of the various cobalt surfaces used in the present computational study. The Co(0001)-p(3x3), Co( $10\bar{1}9$ )-p(1x3) as well as the Co( $11\bar{2}9$ )-p(1x2) slab supercells were modelled from bulk optimized hexagonal close-packed (HCP) cobalt with the lattice parameters,  $a = 2.526\text{\AA}$  and  $c/a = 1.613$ . The Co(0001), Co( $10\bar{1}9$ ) and Co( $11\bar{2}9$ ) slabs had 5, 4 and 4 atomic layers, respectively. In all cases the top two layers were allowed to fully relax during geometry optimization calculations and the adsorbed CO was introduced atop the relaxed surfaces. A  $15\text{\AA}$  vacuum gap was maintained between periodic slabs. The Monkhorst-Pack grid was adjusted to give a k-point sampling density of ca.  $0.030\text{\AA}^{-1}$  for each slab system.

### 3.5 Surface Structures

The Co(0001) surface exposes large close-packed terraces with only four unique high-symmetry adsorption sites. The defect density on flat, well-annealed single crystals is typically in the order of 1%.<sup>[41]</sup> Surface sputtering (1 keV Ar<sup>+</sup>, 300 K – 350K, 5 min) creates a corrugated surface with a high density of undercoordinated sites. STM images (adapted from ref. Böller et al.<sup>[65]</sup>) show that the holes created by sputtering expose small, close-packed terraces with a broad distribution of terrace widths separated by mono-atomic steps running in different directions<sup>[65]</sup>. The roughened surface has a high density of step edges with very small terraces prevalent over the surface<sup>[118]</sup>. Since it is not well defined, a blurred hexagonal pattern was observed in LEED (fig. 3.1(d)).

The Co(10 $\bar{1}$ 9) surface consists of 4-5 atom wide (0001) terraces separated by mono-atomic steps that run along the [10 $\bar{1}$ 0] direction. The atoms at the step edge, which account for 20% of all surface atoms, have a coordination number (CN) of 7. It should be noted that the step edge structure alternates between A-type (100-like microfacets) and B-type (111-like microfacets) as a consequence of the HCP bulk structure. Each terrace has four high-symmetry adsorption sites at different proximity to the step-edge region. In addition, there are also edge-bridge and edge-top sites for each step-edge type.

The Co(11 $\bar{2}$ 9) sample resembles that of the FCC-Co(321) surface<sup>[119]</sup> and contains 2-3 atom wide (0001) terraces separated by monoatomic steps that run along [11 $\bar{2}$ 0] direction. The steps consist of kink sites composed of alternating 111 and 100-like micro-facets which expose 6 and 8-coordinated atoms in equal amounts that together account for 40% of all surface atoms. In addition to the terrace sites on Co(11 $\bar{2}$ 9) there are also step-kink atop and bridge sites. Two different step-kink atop sites are distinguishable by their coordination numbers of 8 (k8a/b) and 6 (k6a/b). The Co(11 $\bar{2}$ 0) surface is of particular interest as a sample for comparison in the present study since it only exposes zigzag rows of 7-coordinated atoms<sup>[51]</sup> without exposing any close-packed terraces and thus gives clear information about CO adsorption on step sites only. Hence, the desorption data on Co(10 $\bar{2}$ 0) is obtained as a part of the collaboration with Strømsheim et al.<sup>[51]</sup> and is used as a good surface for comparison with kinked Co(11 $\bar{2}$ 9) surface.

The LEED pattern of the sputtered surface (fig. 3.1(d)) show weak, broad spots at the (1 $\times$ 1) positions which reflects the small size of the close-packed terraces after sputtering. The diffraction patterns of the stepped and kinked Co surfaces show spot splitting characteristic of stepped surfaces (shown later in fig. 3.6 (d) and (f)). The direction of the splitting confirms that the step edges run along the [10 $\bar{1}$ 0] direction on Co(10 $\bar{1}$ 9) and along the [11 $\bar{2}$ 0] direction on Co(11 $\bar{2}$ 9). The average terrace widths de-

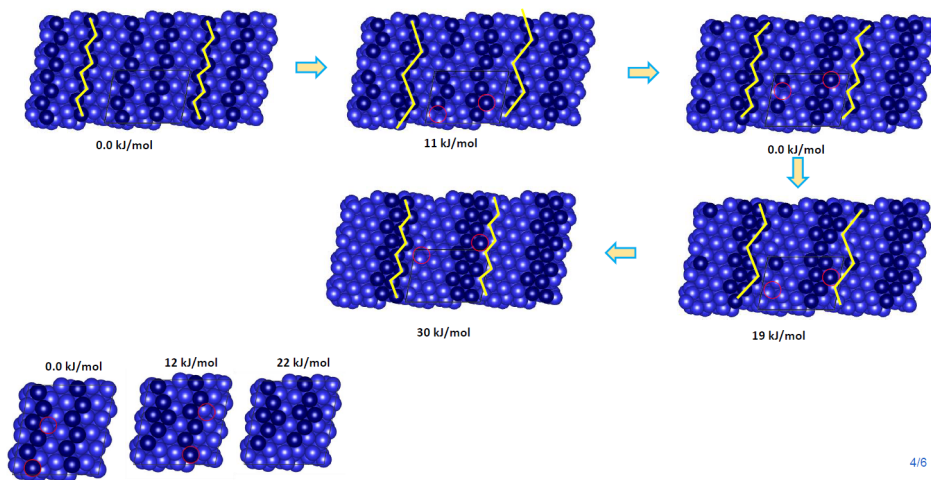


Figure 3.3: Two pathways shown exploring surface reconstruction of Co(11 $\bar{2}$ 9)

rived from the spot splitting were 1.25 nm for Co(10 $\bar{1}$ 9) 0.75 nm for Co(11 $\bar{2}$ 9), which are close to the expected values. We note that the HCP bulk structure results in an alternating step structure and the spot splitting distance corresponds to the distance between two equivalent steps, that is, twice the terrace width. As a consequence, the LEED pattern cannot exclude that step doubling occurs<sup>[63]</sup> and the susceptibility to this specific surface reconstruction was considered further. STM studies on flat and sputter-damaged Co(0001) typically show monoatomic steps that predominantly follow the  $\langle 10\text{-}10 \rangle$  directions of the substrate<sup>[65,120]</sup>. This is taken as evidence that step doubling on the Co(10 $\bar{1}$ 9) surface is unlikely and the sample surface has the bulk-terminated structure.

The Co(11 $\bar{2}$ 9) surface atoms have a wide range of coordination numbers ranging from 6 to  $> 9$  and conventional wisdom suggests a tendency to reduce the concentration of undercoordinated atoms. Migration of the 6-coordinated atoms may lead to formation of more 7-coordinated surface Co atoms at the expense of 6- and 9-coordinated sites and it is not immediately obvious whether this is energetically favorable. Fig. 3.3 shows the two potential pathways considered by DFT, where 6-coordinated Co atoms migrate along (intra-) and across (inter-) the terrace leading to fewer 6-/9-coordinated sites and more 7-coordinated sites. It is found that both reconstruction pathways are energetically unfavorable, i.e.  $\Delta E_{\text{diffusion}} = \pm 10 \text{ kJ mol}^{-1}$ , and reconstruction of the clean surface is therefore deemed unlikely.

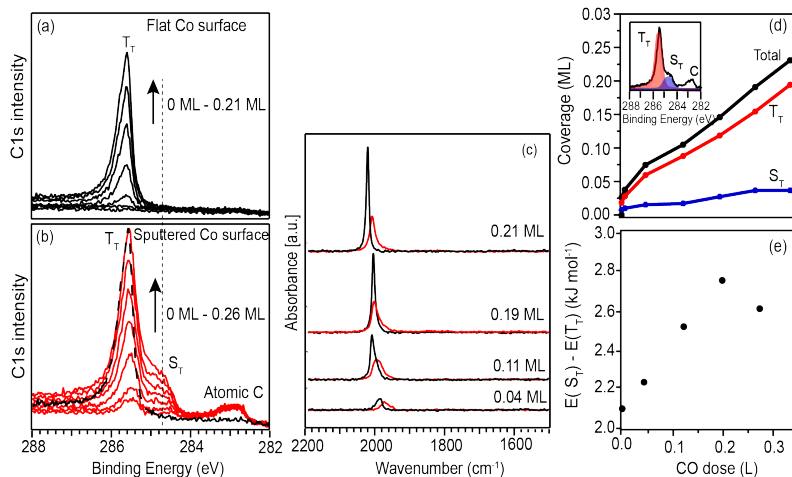


Figure 3.4: Selected C1s spectra at 100 K, acquired on (a) Co(0001) and (b) sputtered Co(0001) surfaces. (c) Individual IR spectra during CO adsorption depicting only intensity increasing in the top-bound region on flat Co(0001) (solid black lines - divided by a factor of 2) and sputtered Co(0001) surface (solid red lines), shown for comparison. The corresponding CO coverage is indicated alongside each spectra. (d) Evolution of peak area with CO exposure after individual fits to all C1s spectra in uptake curves of panel (b). (e) Difference in adsorption energy of CO on  $S_T$  and  $T_T$  sites during CO adsorption with increasing CO dose

### 3.6 CO adsorption on flat and sputtered Co(0001)

Fig.3.4 (a), and (b) shows the series of high resolution C1s spectra acquired during CO exposure on Co(0001) and sputter-damaged Co(0001) at 100K. On Co(0001), lateral interactions between CO molecules cause population of the hollow sites along with top sites when the coverage increases beyond 0.33 ML. We here limit the discussion to the coverage regime  $<0.33$  ML where only top sites are populated on flat Co(0001) and where site occupation is not affected by lateral interactions.

Only one photoemission peak is observed at 285.5 eV on the flat Co(0001) surfaces which is attributed to CO chemisorbed on top sites of close-packed terraces<sup>[97]</sup> (hereafter, referred to as  $T_T$ ). The spectra on the sputter-damaged Co(0001) surface shows an additional low binding energy (B.E.) shoulder around 284.8 eV, the intensity of which increases together with the main peak located at 285.5 eV. Studies on stepped Rh and Pt surfaces show that CO adsorbed at step-top (hereafter, referred to as  $S_T$ ) sites give rise to a separate photoemission peak in the C1s spectrum at a  $\Delta$ BE of -0.35 eV for Rh<sup>[121]</sup> and -0.28 eV for Pt<sup>[122]</sup> relative to the terrace-top peak. In line with this, we attribute the low BE shoulder at 284.8 eV to CO adsorbed on top of undercoordinated surface atoms at the steps and kink sites that were introduced during sputtering. The peak at 283 eV is attributed to a small (0.03 ML) atomic C

contamination that was deposited during sputtering.

The assignment of top-CO is confirmed by the IR absorption spectra shown in fig. 3.4 (c). Both flat and sputter-damaged Co(0001) show only a single peak around  $2000\text{ cm}^{-1}$ , attributed to the C-O stretching frequency of top-bound CO<sup>[52]</sup>. Presence of CO on top of terrace and step sites leads to a broader absorption peak on sputter-damaged Co(0001) and is found at a comparatively lower wavenumber.

Fig. 3.4 (d) shows the evolution of different photoemission peaks (obtained by deconvoluting the spectra as shown in the inset) with CO dose on the sputter-damaged Co(0001) surface. The simultaneous emergence of both  $S_T$  and  $T_T$  components suggests no strong preference for either adsorption site. In contrast, CO adsorption on stepped Pt and Ni surfaces<sup>[122-124]</sup> show a clear preference towards the undercoordinated sites. Assuming that no significant photoelectron diffraction (PED) effects are associated with species adsorbed at defects, the C1s intensity is proportional to the CO coverage in the same way on all vicinal surfaces.

When we assume that there are no kinetic or diffusion limitations for CO and thus it can arrange itself in the most stable configuration, we can use Boltzmann distribution to estimate the difference in adsorption strength of CO on  $S_T$  and  $T_T$  of the sputtered surface at 100 K. Boltzmann distribution states that the adsorption site with the lowest energy (higher adsorption strength) will have the highest probability of being occupied<sup>[125]</sup>. With the defect site concentration assumed to be 15%<sup>[65]</sup>, eq. 3.2 results into a higher CO adsorption strength on defect sites than on the terrace sites by  $2\text{--}3\text{ kJ mol}^{-1}$  during CO adsorption. This difference, while measurable, is relatively small compared to values typically associated with CO-induced surface reconstruction.

$$\frac{0.85 * p_{T_T}}{0.15 * p_{S_T}} = e^{\frac{\epsilon_{S_T} - \epsilon_{T_T}}{RT}} \quad (3.2)$$

Where  $p_{T_T}$  is the probability of CO occupying the  $T_T$  sites,  $p_{S_T}$  is the probability of CO occupying the  $S_T$  sites,  $\epsilon_{S_T}$  is the adsorption strength of CO on the  $S_T$  sites,  $R$  is the gas constant, and  $T$  is the surface temperature (K). Fig. 3.4 (e) shows a higher preference for CO adsorption on defect sites at very low coverage. With increasing CO exposure, the CO molecules on  $T_T$  experience lateral interaction. Greater initial flexibility of CO molecules on  $S_T$  weakens their lateral interactions and explains the increase in the difference between  $S_T$  and  $T_T$  adsorption energies as the coverage increases. This difference in adsorption energies decreases before attaining a plateau as the defect sites saturate with CO.

CO adsorption on various defect rich Co surfaces was also investigated using

Table 3.1: Adsorption energy and vibrational frequency of CO on differently coordinated sites of Co(0001), Co(10 $\bar{1}$ 9) and Co(11 $\bar{2}$ 9)

Co(0001)-p(3x3)			Co(1019)-p(1x3)			Co(1129)		
Site	$E_{ads}$ [kJ mol $^{-1}$ ]	$\nu_i$ [cm $^{-1}$ ]	Site	$E_{ads}$ [kJ mol $^{-1}$ ]	$\nu_i$ [cm $^{-1}$ ]	Site	$E_{ads}$ [kJ mol $^{-1}$ ]	$\nu_i$ [cm $^{-1}$ ]
T	-138	1918	T $_{edge-1}$	-140	1897	T $_{k8a}$	-143	1884
FCC	-128	1704	T $_{edge-2}$	-138	1910	T $_{k8b}$	-141	1882
HCP	-126	1693	T $_{terrace-1}$	-134	1909	T $_{k6a}$	-131	1900
Bridge	-123	1880	T $_{terrace-2}$	-135		T $_{k6b}$	-132	1899
			FCC $_{terrace}$	-125	1701	T $_{t2a}$	-124	1874
			HCP $_{terrace}$	-124		T $_{t1b}$	-126	1871
						T $_{t2b}$	-136	1884

DFT. Table 3.1 shows the calculated adsorption energies of CO on different sites as well as the associated C=O stretching modes. On the flat Co(0001) surface, CO adsorbs strongest on atop sites with an adsorption energy of  $-138 \text{ kJ mol}^{-1}$  compared to  $-128 \text{ kJ mol}^{-1}$  and  $126 \text{ kJ mol}^{-1}$  for adsorption on the three-fold FCC and HCP sites, respectively. On bridge sites CO adsorbs with an even lower adsorption energy of  $-123 \text{ kJ mol}^{-1}$ . This predicted adsorption site preference is in good agreement with experimental observation<sup>[126]</sup>. Moreover, the magnitude of the adsorption strength is also in reasonable agreement with experimental values of  $-115$  to  $-128 \text{ kJ mol}^{-1}$ <sup>[99,126]</sup>.

In contrast, terrace sites on the Co(10 $\bar{1}$ 9) surface binds CO relatively weakly, ca.  $\pm 3 \text{ kJ mol}^{-1}$  compared to the edge sites. On atop sites at the central region of the wide terrace CO adsorbs with an energy of  $-134 \text{ kJ mol}^{-1}$  whilst on nearby FCC and HCP the adsorption energy is  $-125$  and  $-124 \text{ kJ mol}^{-1}$ , respectively. This small difference is likely an attribute of finite structure effects—the presence of the edges affects adsorption on terraces. Consistent with adsorption on Co(0001), the atop sites are still more preferred than three-fold and bridge adsorption sites. The atop sites nearer to the edge region of Co(10 $\bar{1}$ 9) binds CO slightly more strongly. The edge atop sites bind CO with adsorption energies of  $-140 \text{ kJ mol}^{-1}$  and  $-138 \text{ kJ mol}^{-1}$ , at edges terminating wide and narrow terraces, respectively. These adsorption energies are  $\sim 4 \text{ kJ mol}^{-1}$  higher than adsorption on terrace atop sites of the same slab surface.

Finally, the Co(11 $\bar{2}$ 9) surface has a larger number of unique adsorption sites given the presence of step-kink edge and the small size of the intervening (111) terraces. Adsorption of CO on these sites was considered. As was the case for the Co(11 $\bar{2}$ 9) surface, atop adsorption was preferred over bridge and three-fold adsorption states. The two 9-coordinated atop sites on the wide terrace adsorb CO with an adsorption energy of  $-126 \text{ kJ mol}^{-1}$  and  $-136 \text{ kJ mol}^{-1}$ , with the lower value being closer to the step-kink terminating the narrow terrace. On the narrow terrace there is only one 9-coordinated atop site which binds CO with an energy of  $-124 \text{ kJ mol}^{-1}$ —this site is located at an equivalent proximity to the step-kink as the weakly binding atop site on the wide terrace.

Compared to these terrace sites, on the step-kink edge CO can adsorb atop either

6- or 8-coordinated Co atoms. The adsorption on 8-coordinated Co atoms (k8a/b) was found to be more favorable with adsorption energies of  $-141$  to  $-143$   $\text{kJ mol}^{-1}$  compared to adsorption on the 6-coordinated Co atoms (k6a/b) where CO adsorbs with an adsorption energy of ca.  $-132$   $\text{kJ mol}^{-1}$ . Adsorption on bridge and three-fold sites only lead to energies in the range of  $-100$  and  $-132$   $\text{kJ mol}^{-1}$ . Vibrational analyses were conducted for all considered adsorption states (see table 3.1). In general, adsorption on atop sites was found to be in the range of  $1890$  and  $1950$   $\text{cm}^{-1}$  compared to adsorption on fcc ( $1700$   $\text{cm}^{-1}$ ), and hcp ( $1690$   $\text{cm}^{-1}$ ) sites. These C=O stretching modes although lower in wavenumber compared to experimental observations, are different enough for the different adsorption states to enable a confident assignment (interpretation of the experimentally measured modes). Focusing only on the atop adsorption states, no discernable trend was observed.

### 3.7 CO desorption

Fig. 3.5 (b,c) shows the HR C1s spectra recorded while slowly heating the CO covered sputter-damaged Co(0001) and flat Co(0001) in vacuum. CO desorption from  $T_T$  and  $S_T$  with increasing temperature can be explored by following the reduction in the intensity of the photoemission peaks ( $285.5$  eV and  $284.8$  eV) as shown in fig. 3.5 (j,k) with increasing temperature. On the sputter-damaged Co(0001), the peak representing CO adsorption on  $S_T$  disappears 50 K before the  $T_T$  peak. This can be explained by smoothening of the sputtered Co(0001) surface during heating  $>350$  K when the surface starts to restructure itself and consequently leads to disappearance of the defect sites.

Furthermore, the same desorption experiments were performed on the well-defined Co( $10\bar{1}9$ ) and Co( $11\bar{2}9$ ) surfaces. Fig. 3 (a,d) show characteristic MR XPS spectra obtained while heating the CO covered Co( $10\bar{1}9$ ) and Co( $11\bar{2}9$ ). Selected spectra measured at 300 K from panels (a,d) in fig. 3.5 are deconvoluted into a peak associated with adsorption on terraces and a low binding energy peak associated with adsorption on steps/kinks and shown in the fig. 3.5 (e,h). The changes in the CO coverage represented by the integrated intensity of the photoemission peaks with increasing temperature is shown in fig. 3.5 (i,l). The experiment shows that both species are completely desorbed at 420K on the various Co surfaces. Comparison of the CO desorption temperature of  $T_T$  and  $S_T$  species suggests equal probability of CO to occupy either the terrace or defect sites on Co( $10\bar{1}9$ ). These results suggest structure insensitive adsorption of CO on the Co surfaces which is also supported by theoretical calculations. No significant CO dissociation and eventual build-up of surface carbon was observed on the defect-rich surfaces during adsorption and desorption, hence it has been left out of the systematic coverage analysis. As explained in sec-

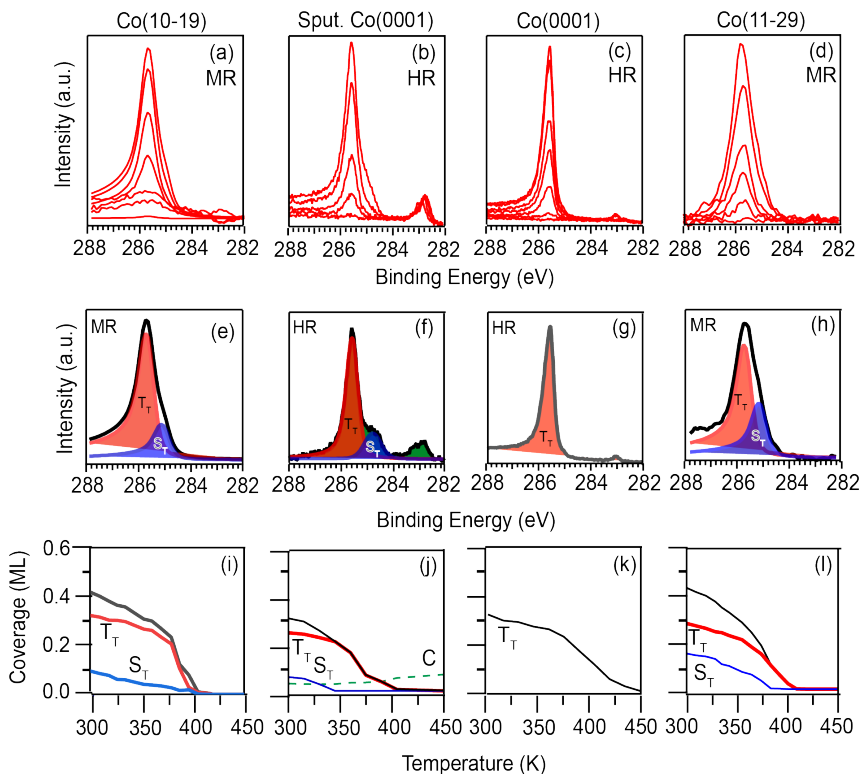


Figure 3.5: (a) - (d) C1s spectra recorded during CO desorption ( $0.3 \text{ Ks}^{-1}$ ) from Co(10-19), sputtered Co(0001), Co(0001) and Co(11-29) surfaces. (e-h) Selected spectra measured at 300 K, showing fitting lines for different chemisorption sites. (i-l) Changes in peak area with increasing temperature, after individual fits to all C1s spectra in the desorption curves of panels (a-d). The black, red and blue lines represent total CO coverage, CO coverage on terrace top sites and CO coverage on step top sites, respectively. The green dashed line on roughened Co(0001) in panel j shows evolution of atomic C during heating

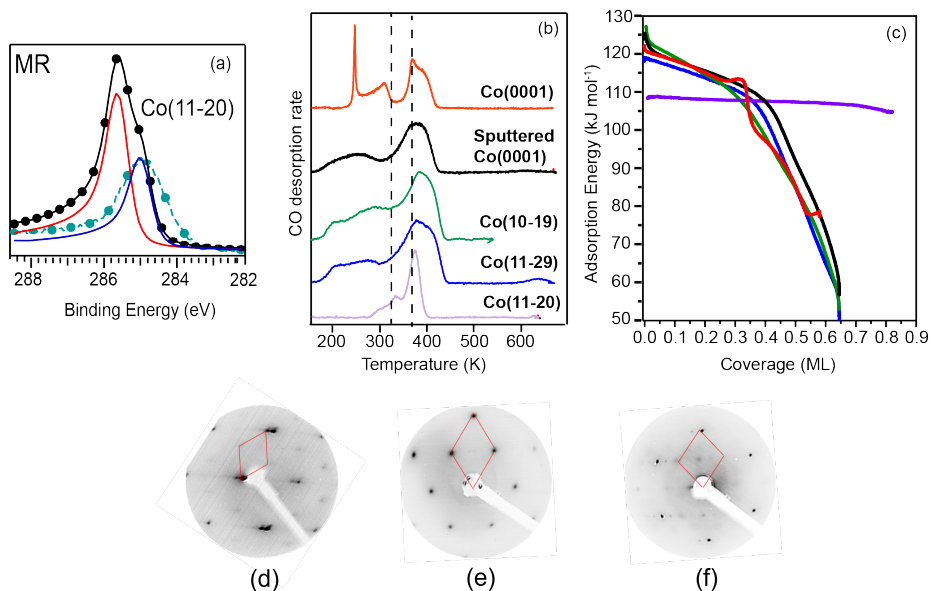


Figure 3.6: (a) Comparison of C1s spectra on CO covered  $\text{Co}(11\bar{2}9)$  and  $\text{Co}(11\bar{2}0)$  (green dashed line) at 300 K. The red and blue curve represent the deconvolution of the total black curve on  $\text{Co}(11\bar{2}9)$  surface. (b) CO TPD curves on heating CO saturated  $\text{Co}(0001)$ , sputtered  $\text{Co}(0001)$ ,  $\text{Co}(10\bar{1}9)$ ,  $\text{Co}(11\bar{2}9)$  and  $\text{Co}(11\bar{2}0)$  surfaces in vacuum at  $1 \text{ K s}^{-1}$ . (c) Variation of CO desorption energy with increasing coverage on  $\text{Co}(0001)$ (red curve), sputtered  $\text{Co}(0001)$  (black curve),  $\text{Co}(10\bar{1}9)$  (green curve),  $\text{Co}(11\bar{2}9)$  (blue curve) and  $\text{Co}(11\bar{2}0)$  (purple curve). (d-f) LEED images of CO covered  $\text{Co}(10\bar{1}9)$ ,  $\text{Co}(0001)$  and  $\text{Co}(11\bar{2}9)$  at 100 K after heating to 300 K.

tion 3.6, the small (0.03 ML) atomic C contamination on the sputtered  $\text{Co}(0001)$  was deposited during sputtering.

In order to confirm the attribution of the photoemission peaks in XPS, C1s spectra recorded on CO covered unreconstructed  $\text{Co}(11\bar{2}0)$  were compared with the current data set on  $\text{Co}(11\bar{2}9)$ .  $\text{Co}(11\bar{2}0)$  consists of zig-zag row of Co atoms and misses the terraces present on  $\text{Co}(11\bar{2}9)$ . Therefore, the core-level line on  $\text{Co}(11\bar{2}0)$  arises from CO adsorption solely on defect sites which compares with the  $S_T$  peak in the C1s spectra of  $\text{Co}(11\bar{2}9)$  surface (fig. 3.6 (a)).

Separate desorption features in the TPD spectra are observed on  $\text{Pt}(355)$ <sup>[115,124]</sup>,  $\text{Pt}(322)$ <sup>[124]</sup>,  $\text{Pt}(112)$ <sup>[127]</sup>, and residual steps on  $\text{Pt}(111)$ <sup>[128,129]</sup> attributed to desorption from terraces at lower temperature and from defects at higher temperature supporting the notion of stronger adsorption on the undercoordinated sites. Although on stepped  $\text{Rh}(553)$ <sup>[48]</sup> and  $\text{Rh}(311)$ <sup>[49]</sup>, stronger CO adsorption on steps was established by techniques like IR and XPS, there was no additional high-temperature feature

observed in the TPD spectra. Many CO chemisorption studies that have been performed through these years have found that more open surfaces provide a larger adsorption energy as compared to the closed pack surfaces. Examples of this are Ru(10 $\bar{1}0$ )<sup>[130]</sup>, ( 150 kJ mol<sup>-1</sup>) and Ru(0001)<sup>[131]</sup> ( 122 kJ mol<sup>-1</sup>), Rh (111)<sup>[132]</sup> (130 kJ mol<sup>-1</sup>) and Rh(110) (125 kJ mol<sup>-1</sup>), and Pd(111)<sup>[133]</sup> (143 kJ mol<sup>-1</sup>) and Pd(110) (150 kJ mol<sup>-1</sup>). However, no distinctive high temperature desorption feature was observed on heating the CO saturated defect-rich Co surfaces when compared to the flat Co(0001) surface (fig. 3.6 (a)). Fig. 3.6 (c) compares the activation energy of CO desorption ( $E_{des}$ ) as a function of coverage and temperature from the various Co surfaces using the rate of desorption expression.

$$r = -\frac{d\theta}{dt} = \nu e^{\frac{E_{des}}{RT}} \theta \quad (3.3)$$

assuming a pre-exponential factor of 10<sup>13</sup> s<sup>-1</sup>. We arrive at an initial adsorption energy  $E_{ads}$  of 112 kJ mol<sup>-1</sup> on the flat Co(0001), 114 kJ mol<sup>-1</sup> on the roughened Co(0001) and stepped Co(10 $\bar{1}9$ ) surfaces, 110 kJ mol<sup>-1</sup> on the kinked Co(11 $\bar{2}9$ ) and, 100 kJ mol<sup>-1</sup> on the kinked-only Co(10 $\bar{2}0$ ) surface. The values of  $E_{des}$ , thus obtained are in agreement with the adsorption energy determined by Weststrate et. al. on Co(0001) surface<sup>[52]</sup>. The desorption curve in fig. 3.6 (b) of Co(0001) exhibit a respective increase in  $E_{des}$  or decrease in the slope at about 330K, suggesting that at this CO coverage, the well ordered ( $\sqrt{3} \times \sqrt{3}$ )R30° structure is formed (fig. 3.6 (e)). The large terraces on Co(0001) allow the formation of this ordered structure to relieve the repulsive lateral interactions between the CO molecules with increasing CO coverage. This ordering is also reflected in narrowing of the TPD curve on Co(0001) between 300 K - 330 K (fig. 3.6 (b) – dashed lines).

Conversely, ordering of CO molecules becomes difficult on the defect rich surfaces as increasing defect concentration is accompanied by shortening of the terrace width. The consequence of CO molecules' inability to arrange themselves in large ordered structure on the defect rich surfaces is an increase in the repulsive interactions between the molecules with increasing coverage and broad TPD curves. CO forms a ( $\sqrt{3} \times \sqrt{3}$ )R30° structure on the terraces of Co(10 $\bar{1}9$ ) (fig. 3.6 (d)) and Co(11 $\bar{2}9$ ) (fig. 3.6 (e)) accompanied by increasingly blurred spots with decreasing width of the terraces. No traces of reconstruction was found on Co(10 $\bar{1}9$ ) and Co(11 $\bar{2}9$ ) surfaces in the presence of CO in the corresponding LEED images.

### 3.8 Discussion

Sputtered surfaces have previously been used as a model for a defect rich surfaces in CO adsorption on Pt<sup>[129]</sup> and Au<sup>[134]</sup> and dissociation studies on Ni<sup>[135]</sup>. The different electronic structure of the defect and terrace atoms makes it possible to distinguish between CO adsorption on those sites. C1s peak positions from XPS were used to determine the hierarchy of CO adsorption sites on sputtered Co(0001), Co(10 $\bar{1}$ 9), and Co(11 $\bar{2}$ 9) and compared with Co(0001). The two C1s components varying in relative intensity with CO coverage indicate the presence of two inequivalent types of CO molecules ( $T_T$  and  $S_T$ ) on the defect-rich surfaces. Absence of atomic C peak on the well defined Co surfaces during CO adsorption rules out the role of C in the origin on the low binding energy  $S_T$  peak. CO adsorption on Pt(111) curved crystal<sup>[122]</sup>, comprising of A and B-type steps and Rh(553)<sup>[48]</sup> results in a core-level line at a higher binding energy when adsorbed on terrace site as compared to the defect sites with preference for adsorption on defect sites. However, from the high resolution C1s adsorption spectra on the roughened Co(0001) (fig. 3.5) it can be concluded that CO shows slight preference for defect than the terrace sites on Co surface.

No evidence to support a CO-driven reconstruction of surface defect site was found in either the experimental data or in DFT calculation on the Co(11 $\bar{2}$ 9). Therefore, under both CO and UHV conditions, Co(11 $\bar{2}$ 9) remains unreconstructed.

Calculations confirm the preferred adsorption site for CO to be the atop at both terrace and defect sites, consistent with experimental IR measurements in the present study. Moreover, the calculated IR frequencies are in agreement with experiments suggesting atop adsorption as being the most preferred state, albeit with small differences in the actual magnitude of the calculated modes. The adsorption on defect top sites is only ca. 6 kJ mol<sup>-1</sup> more stable than on terrace sites. This difference is at first glance in the range of error expected from computational factors such as slab thickness. However, since from experiments two adsorption states are resolved, i.e. terrace and defect atop, with a comparable energy difference in the range 4 – 6 kJ mol<sup>-1</sup>, this calculated difference supports the results. Therefore, computational calculations confirms the suggested weak dependence of CO adsorption on the surface structure of cobalt.

The idea of CO adsorbing with equal (or slightly higher) adsorption strength on defect sites than terrace sites on Co surface is not previously reported in the experimental work in the literature. The work discussed in this paper present a strong proof of identification of CO adsorption on defect sites of Co with the help of XPS. This study is helpful to understand and extrapolate the influence of defect sites on the FTS reaction on the catalyst nanoparticles which consists of both terraces and defect edges. The results reported are obtained under UHV conditions which are far

from real FTS conditions where high pressure of CO prevails. The catalyst nanoparticle (relevant for catalysis) are prone to be blocked for CO dissociation by the strongly adsorbing CO or its dissociated products C and O during FTS. However, we propose that CO molecules do not prefer defect sites over the terrace sites for adsorption and adsorb more or less with the same adsorption strength on both the undercoordinated and terrace sites of the Co surface. Thus, even under high pressure defects can still remain available for CO and H<sub>2</sub> dissociation unless blocked by other intermediates and reaction products. As outlined in the introduction, stronger adsorption of CO on defect sites might lead to the reconstruction of Co nanoparticles into highly faceted nanoparticles. A small difference in adsorption strength on defect and terrace sites also means small driving force for surface reconstruction. We note that the CO adsorbs most strongly to kink sites as compared to terrace and step sites. Therefore, the reconstruction of a Co catalyst under reaction conditions would lead to a surface exposing lesser highly undercoordinated sites like kinks than the other way round.

### 3.9 Conclusions

In this work we have compared the adsorption of CO on flat Co(0001), sputtered Co(0001), stepped Co(10 $\bar{1}$ 9), and kinked Co(11 $\bar{2}$ 9) single crystal surfaces in the regime of low CO coverage. The flat surface is used as reference to get detailed insight into the influence of defects on the adsorption of CO. The TPD spectra of CO from the sputtered surface and the kinked Co surface are very similar to the TPD from Co(0001) at low CO coverage at the first glance. However, a separate desorption feature was observed on the defect-rich and kinked surface which made the desorption spectra broader at the lower temperature end. This could be attributed to CO desorbing from the defect sites. Infrared spectroscopy and X-ray photoelectron spectroscopy show that at low coverages both terrace-top and step-top sites are occupied simultaneously. However, a very sharp distinction between the two sites cannot be made using just IR. The IR experiments in combination with temperature programmed XPS and desorption data suggest that the defect sites have only a small influence on CO adsorption. No under-coordinated-site preference is observed on the defect-rich surfaces for CO adsorption. Hence, Co catalyst nanoparticles are not expected to reconstruct into highly faceted nanoparticles and the defect sites can remain available for further adsorption during Fischer-Tropsch synthesis.

## 3.10 Supplementary Information

### 3.10.1 TPD measurements

#### CO coverage determination on defect-rich Co(0001), stepped Co(10 $\bar{1}$ 9) and kinked Co(11 $\bar{2}$ 9)

Several studies show that adsorption of CO at room temperature on Co(0001) leads to the formation of an ordered ( $\sqrt{3} \times \sqrt{3}$ )R30° adsorbate overlayer with a coverage of 0.33 ML<sup>[52]</sup>. This coverage was used as a reference point in our work to determine the CO coverage on the other Co surfaces. We made use of the fact that Co(0001) and one of the defect-rich could be simultaneously mounted on the sample holder. In this way, it was possible to change between the two samples in less than a minute without breaking vacuum. Fig. 3.7 summarizes the results of the TPD experiments that were performed to quantify the CO coverage on Co(11 $\bar{2}$ 9) (for eg.) using CO desorption from Co(0001) as a reference. The samples were intentionally placed far away from the entrance of the QMS (Hiden HAL 301) compartment as indicated in the figure and the QMS (Pfeiffer Vacuum QME 200) installed in the main chamber is used for quantification of the signal intensity, instead. In this way, it is possible to compare the TPD peak areas from the two samples since the signal intensity is no longer sensitive to the exact sample position. Fig. 3.7 (a) shows a schematic of the sample position relative to the QMS compartment opening for this series of experiments. This arrangement led to a loss of signal intensity in the QMS so that the signal-to-noise ratio for a single TPD measurement is relatively high. We therefore repeated the TPD experiment several times. The desorption spectra for repeated experiments (with a cleaning step between each experiment for Co(11 $\bar{2}$ 9)) were very similar both in terms of peak shape and in signal intensity. The average of a number of such TPD spectra was used to evaluate the peak area and to derive coverages.

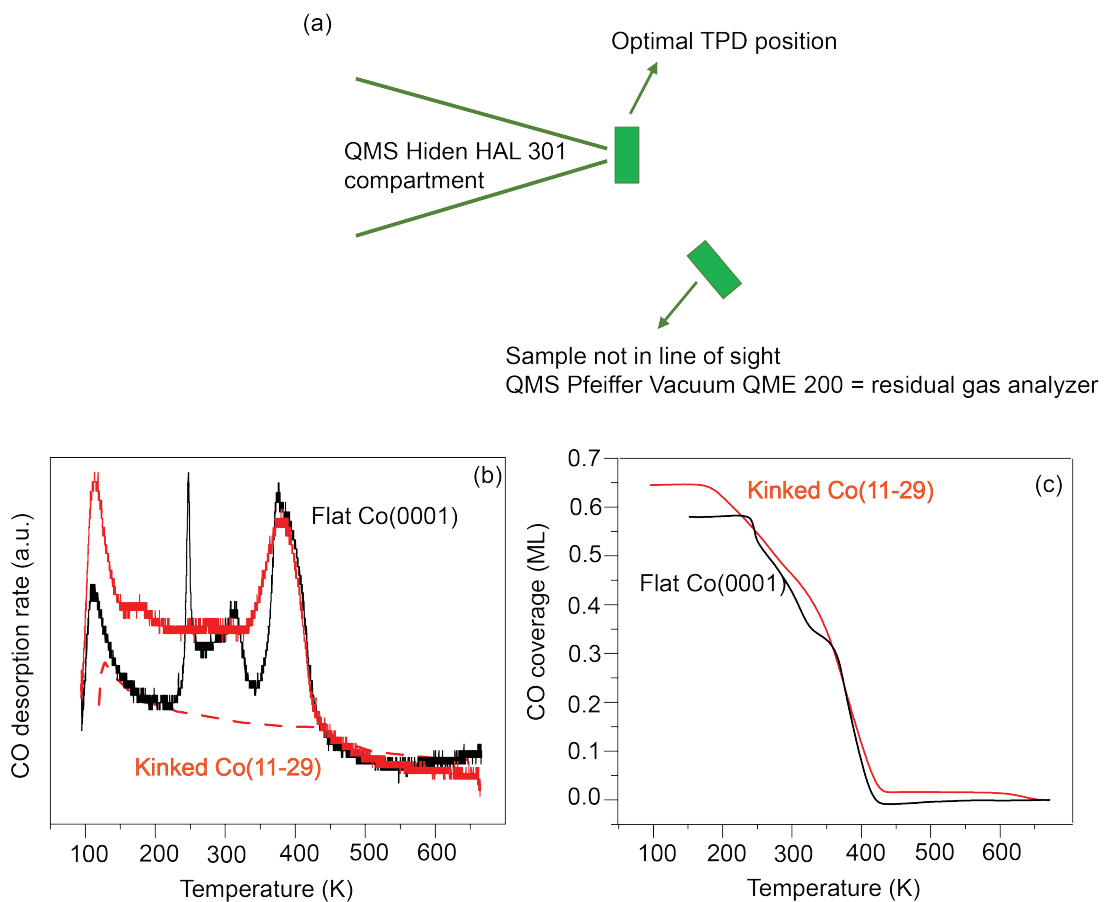


Figure 3.7: (a) Illustration of the two sample positions for the TPD measurements; (b) MS desorption spectra, without background subtraction, acquired with sample not in line of sight of QMS; (c) corrected areas with respect to sample size and atom density.

### 3.11 Abbreviations

1. BE	Binding Energy (eV)
2. CN	Coordination number
3. DFT	Density Functional Theory
4. FCC	Face-centered cubic
5. FTS	Fischer-Tropsch synthesis
6. HCP	Hexagonal close packed
7. HR	High resolution
8. IR	Infrared
9. LEED	Low energy electron diffraction
10. MR	Medium resolution
11. $r$	Rate of desorption
12. $R$	Universal gas constant ( $\text{m}^3 \cdot \text{Pa} \cdot \text{K}^{-1} \cdot \text{mol}^{-1}$ )
13. RAIRS	Reflection absorption infrared spectra
14. QMS	Quadrupole mass spectrometer
15. $T$	Absolute temperature (K)
16. $T_T$	Top site of steps
17. STM	Scanning tunneling microscopy
18. TPD	Temperature programmed desorption
19. $T_T$	Top site of close-packed terraces
20. $E_{des}$	Activation energy of desorption ( $\text{kJ mol}^{-1}$ )
21. VASP	Vienna Ab initio Simulation Package
22. vdw-DF	van der Waals - Density Functional
23. XPS	X-ray photoelectron spectroscopy
24. $\theta$	Surface coverage of the desorbing species (ML)

## Chapter 4

# CO and hydrogen co-adsorption on Co(0001)

### 4.1 Abstract

The interaction between hydrogen and CO on cobalt surfaces is of fundamental interest for Fischer-Tropsch synthesis. In this chapter, the adsorption and co-adsorption of hydrogen and CO on the Co(0001) surface is studied under UHV conditions using a combination of TPD, LEED, and IR. The present work delves into the influence of lateral interactions between CO and hydrogen adsorbed on the Co(0001) surface as reflected in the TPD spectra of both species. Our investigation explores the different overlayer structures formed to accommodate both CO and hydrogen on the surface and how their stability is affected by the lateral interactions. The co-adsorption study reveals that hydrogen and CO form segregated islands on Co(0001). Several distinct phases with specific stability were identified for different hydrogen and CO coverages. Dosing CO onto a surface covered with 0.5 ML  $H_{ad}$  produces CO islands with a  $(2\sqrt{3} \times 2\sqrt{3})R30^\circ$  structure and a local coverage of 0.58 ML while hydrogen is compressed into  $(1 \times 1)$  H islands. Desorption of CO and hydrogen during heating results in an intermediate phase where CO islands with a  $(\sqrt{3} \times \sqrt{3})R30^\circ$  structure co-exist with  $(2 \times 2)$ -2H islands with a local hydrogen coverage of 0.5 ML. The presence of pre-adsorbed CO inhibits the dissociative adsorption process of hydrogen and when the surface is covered with 0.33 ML of CO, dissociative hydrogen adsorption is blocked. Analysis of the co-adsorption structure formed for lower CO pre-coverages shows the presence of  $(\sqrt{3} \times \sqrt{3})R30^\circ$  CO islands co-existing with  $(2 \times 2)$ -2H islands. Although the H and CO phases are segregated the hydrogen desorption temperature is still lowered by the presence of CO islands nearby, indicating a destabilizing effect that is attributed to the repulsive interactions at the CO-H island interface. When hydrogen is dosed with help of a filament, 'hot' hydrogen molecules

and atoms capable of surmounting the dissociation barrier are generated resulting in high hydrogen coverages on the surface. In this case, a structure with  $(\sqrt{3}\times\sqrt{3})R30^\circ$  CO islands and (1x1) H islands with a local coverage 1 ML is formed.

## 4.2 Introduction

Given the significance of cobalt catalysts in Fischer-Tropsch synthesis, it is important to investigate the interaction of adsorbed hydrogen and  $\text{CO}_{ad}$  on cobalt. Even, non-reactive interactions can affect surface coverages and binding strengths, which ultimately influences the overall reaction rates and selectivity. Understanding non-reactive interactions gives fundamental insight into the molecular phenomena that occur on the surface of the catalyst and ultimately translate to overall activity and selectivity<sup>[91,136,137]</sup>. CO and H co-adsorption is an attractive topic for surface science studies. The adsorption of CO and hydrogen on their own has been extensively investigated<sup>[43,44,52,99]</sup> on Co(0001), but co-adsorption is more complex than the single adsorbate studies. The complexity of co-adsorption systems arises from the introduction of a number of new phenomena such as site blocking, segregation, and mixing<sup>[138,139]</sup>. Under FT high pressure reaction conditions, a high coverage of hydrogen and CO is expected. To simulate this scenario at low pressure, we employ low temperatures, which also yield high adsorbate coverages. This enables us to explore how high coverage of CO influences adsorption of hydrogen and vice-versa. It is important to note that although not identical to the real reaction conditions, this approach can provide valuable insights into the nature of interactions between H and CO<sup>[21]</sup>.

Earlier research on the simultaneous adsorption of hydrogen and CO on transition metal surfaces has revealed that the nature of their interaction (attractive or repulsive) varies depending on the specific metal catalyst and surface structure. Studies have shown that on Pt(111)<sup>[140,141]</sup> and Pd(111)<sup>[142]</sup> surfaces, hydrogen tends to segregate and form a compressed phase, coexisting with CO ad-islands. This segregation is similar to what has been observed on other close-packed metal surfaces<sup>[141]</sup>. Studies on Ir, Ni, Ru and Pd<sup>[142-145]</sup> have proposed that when a surface is already covered with CO, the presence of CO inhibits the adsorption of hydrogen<sup>[146]</sup>. This inhibition occurs because CO raises the barrier for dissociative hydrogen adsorption, either through geometric site blocking or by altering the electronic structure of the substrate. In addition, studies have shown that CO can displace hydrogen on surfaces pre-covered with hydrogen at higher temperatures, as demonstrated on Ir(111)<sup>[143]</sup>, Ni(111)<sup>[144]</sup>, and Pd(111)<sup>[142]</sup>. Morkel et. al.<sup>[147]</sup> reported that on Pd(111), hydrogen adsorption is suppressed by  $\text{CO}_{ad}$  at low surface temperature, while CO replaces hydrogen at higher temperatures (150 K). They also found that  $\text{CO}_{ad}$  hin-

ders the dissociative adsorption of hydrogen by modifying the electronic structure of the substrate and increasing the barrier for hydrogen adsorption. In a temperature and pressure regime where both hydrogen and CO adsorption are in dynamic equilibrium with the gas phase, CO also suppresses dissociative hydrogen adsorption. Similarly, Johansson et al.<sup>[148]</sup> discovered that ppm levels of CO significantly inhibit the formation rate of HD in a 99% H<sub>2</sub>/1% D<sub>2</sub> mixture on evaporated metal films of various metals. This effect is attributed to the presence of CO, which results in a decreased dissociative coefficient. These surfaces are comparable to Co(0001) and have shown segregation of CO and H during co-adsorption while formation of mixed H-CO layer is mostly observed on stepped surfaces (elaborated in the introduction of chapter 5).

For cobalt, Lewis et al.<sup>[145]</sup> found that during CO adsorption on a H<sub>ad</sub> pre-saturated surface, small CO islands form within the H<sub>ad</sub> layer on Co nano-islands exposing a Co(111) surface as revealed by scanning tunneling microscopy (STM) experiments. No diffusion between them occurs because they are locked in place due to the absence of vacant Co sites at high coverages. The same study reported DFT calculations on three mixed phases of CO<sub>ad</sub> and H<sub>ad</sub> which suggest that segregation of CO<sub>ad</sub> and H<sub>ad</sub> is energetically favored over mixing.

The present chapter explores the co-adsorption of hydrogen and CO on the close-packed Co(0001) surface using two different exposure sequences. First, exposing Co(0001) pre-covered with hydrogen to CO and secondly, exposing Co(0001) pre-covered with CO to hydrogen. After a brief description of the experimental setup and procedures, we first investigate the coverages that can be reached with hydrogen (in the absence and presence of a hot hydrogen source) and CO together on the surface to shed light on how CO adsorption properties are affected in a densely packed hydrogen co-adsorbate layer. Finally we gain insight on dissociative adsorption of hydrogen in presence of pre-adsorbed CO.

### 4.3 Experimental

The experiments were carried out in an ultrahigh vacuum (UHV) chamber with a base pressure of  $1 \times 10^{-10}$  mbar equipped with a sputter gun for sample cleaning, LEED/Auger optics, an infra-red spectrometer, and two quadrupole mass spectrometers (QMS). One mass spectrometer was on the main chamber and probed the residual gas while a second mass spectrometer was in a separately pumped compartment. For desorption studies, the sample was placed around 2 mm away from the 5 mm wide opening of the differentially pumped QMS housing (see fig. 2.7). The TPD spectra reported here were taken at  $2 \text{ K s}^{-1}$  with the sample facing the mass spec-

trometer with the separate pumping compartment. This sample placement eliminated desorption from other parts of the sample holder but quantitative evaluation may be affected in cases where desorption occurs preferentially in one direction with respect to the surface normal<sup>[149]</sup>. The mass spectrometer located in the main chamber was used whenever possible to make quantification more reliable.

Hydrogen and CO were passed through a cold trap held at liquid nitrogen temperature and dosed through individual leak valves into the vacuum chamber. A tungsten coil with a wire diameter of 0.38 mm and a total length of about 12 cm was used to generate 'hot' hydrogen. It was operated at 5 – 5.5 A, which resulted in the filament temperature between 1570 and 1640 K, as determined using a pyrometer. The filament was attached to a z-translator and was placed ~10–30 mm away from the sample surface during dosing [see inset fig. 4.2]. The close proximity of the hot filament caused the sample temperature to slowly rise during dosing, and the filament-sample distance was adjusted so that the sample stayed below 130 K during exposure to hydrogen. The filament was degassed prior to use and the background pressure in the system during operation of the filament remained at  $3 \times 10^{-10}$  mbar.

## 4.4 Results and discussion

### 4.4.1 CO adsorption on Co(0001)

The adsorption of CO on Co(0001) has been previously described by several authors and is summarized here to serve as background information for the co-adsorption study. Fig. 4.1(a) shows CO desorption spectra for different CO coverages (0 - 0.58 ML) on Co(0001) while fig. 4.1(b) shows the IR spectra and corresponding LEED patterns for specific coverages (0.33 ML and 0.58 ML). At low pressure saturation coverage ( $\theta_{CO} = 0.58$  ML), the electron diffraction pattern shows a unit cell of  $(2\sqrt{3} \times 2\sqrt{3})R30^\circ$  while the IR spectrum shows occupancy of top ( $2025 \text{ cm}^{-1}$ ) and twofold bridge sites ( $1908 \text{ cm}^{-1}$ ). From the literature studies<sup>[21,52,98]</sup>, the top/bridge ratio is found to be 1:6, that is the  $12$  surface atom large  $(2\sqrt{3} \times 2\sqrt{3})R30^\circ$  unit cell contains 1 CO molecule adsorbed on a top site and 6 CO molecules adsorbed on a bridge site. The narrow desorption peak at 240 K corresponds to a change in the IR spectra, where the disappearance of the signal at  $1908 \text{ cm}^{-1}$  and the appearance of a broad peak around  $1833 \text{ cm}^{-1}$  indicates a shift in site occupancy from bridge-top to top-hollow. Between 250 and 320 K, the gradual desorption of 0.17 ML CO takes place, during which the hollow sites are depopulated and the concentration of CO on the top sites increases. At around 320 K, a  $(\sqrt{3} \times \sqrt{3})R30^\circ$  LEED structure is formed, corresponding to a  $\theta_{CO}$  of 0.33 ML, where CO solely adsorbs on top sites ( $2025 \text{ cm}^{-1}$ ) with an adsorption energy of  $115\text{-}125 \text{ kJ mol}^{-1}$ <sup>[52,99]</sup>. As the temperature

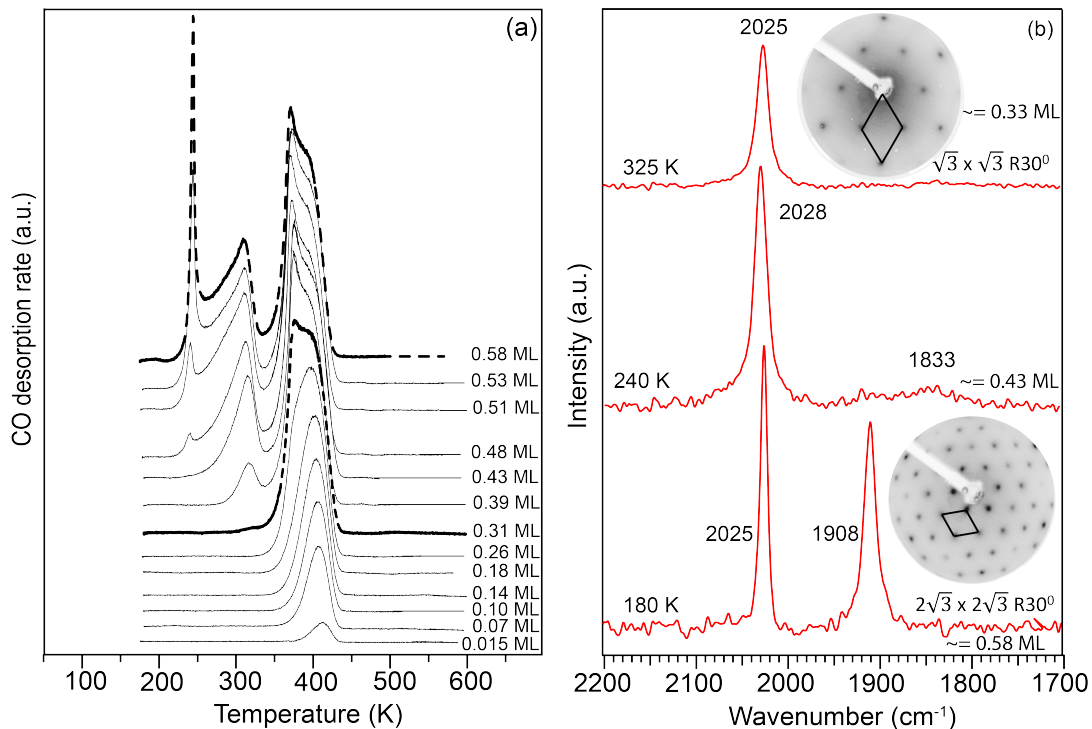


Figure 4.1: (a) Selection of CO TPD spectra obtained by heating the Co(0001) at  $2 \text{ K s}^{-1}$  followed by exposure to CO (b) Illustration of the IR spectra at  $\theta_{CO} = 0.58$  ML CO, 0.43 ML CO and 0.33 ML. LEED patterns corresponding to  $\theta_{CO} = 0.33$  ML and 0.58 ML is shown alongside the corresponding IR spectrum. The LEED structures were recorded at 100 K using 92 eV electron energy

rises further, the surface is gradually depopulated, and by approximately 450 K, all  $\text{CO}_{ad}$  has left the surface.

#### 4.4.2 Hydrogen adsorption on Co(0001)

The adsorption of hydrogen was investigated by introducing  $\text{H}_2$  to the surface maintained at 110 K. At this temperature, hydrogen undergoes dissociation upon adsorption, and a saturation coverage of 0.5 ML of atomic hydrogen ( $\text{H}_{ad}$ ) is observed when UHV-like pressures are used for dosing. The desorption of hydrogen in this coverage regime occurs between 300 to 400 K (as shown in fig. 4.2)<sup>[44,150,151]</sup>. The shifting of the peak maximum towards lower temperature with increasing hydrogen coverage shows second order desorption kinetics as a result of recombinative desorption of two hydrogen atoms to form  $\text{H}_2(\text{g})$ .

Theoretical findings suggest that the process of dissociative hydrogen adsorption on a smooth Co(0001) surface is slightly activated. Additionally, these results indicate that the presence of hydrogen already adsorbed on the surface hinders the dissociative adsorption of additional hydrogen as the coverage approaches  $\theta = 0.5$  ML<sup>[45]</sup>. This phenomenon accounts for the maximum coverage of 0.5 ML of atomic hydrogen ( $\text{H}_{ad}$ ) achieved when hydrogen gas is dosed at UHV-like pressures. Calculations further reveal that hydrogen coverages up to 1 ML remain energetically favorable. However, the adsorption energy of hydrogen on this surface is coverage-dependent, showing a decrease of approximately  $12 \text{ kJ mol}^{-1}$  per hydrogen molecule around  $\theta = 0.5$  ML.

The kinetic limitation of a hydrogen coverage of 0.5 ML can be overcome experimentally by utilizing a hot tungsten filament (as shown in the inset of fig. 4.2). This method generates hot hydrogen molecules and hydrogen atoms which possess a high sticking probability on the surface. As a result, hydrogen coverages above 0.5 ML can be attained. However, the hydrogen exceeding 0.5 ML binds more weakly to the surface and desorbs in a separate low-temperature desorption peak at 280 K as shown in fig. 4.2. This is consistent with the study done by van Helden et. al.<sup>[45]</sup> who showed that heating the sputtered Co(0001) saturated with 0.75 ML hydrogen results in two broad peaks, one centered at 220 K and the other at 310 K, both at significantly lower temperatures than the single desorption peak from the smooth surface, which is centered around 340 K and is equivalent to  $\theta = 0.5$  ML. The LEED pattern for a hydrogen coverage above 0.9 ML only show the  $(1 \times 1)$  diffraction spots of the Co(0001) substrate. The hydrogen most likely forms a  $(1 \times 1)$  overlayer in this regime with adsorption primarily in the fcc hollow sites followed by hcp hollow sites. A faint  $(2 \times 2)$  pattern becomes visible for  $\text{H}_{ad} = 0.8$  ML. The  $(2 \times 2)$  diffraction spots increase in intensity and become sharper with decreasing hydrogen coverage,

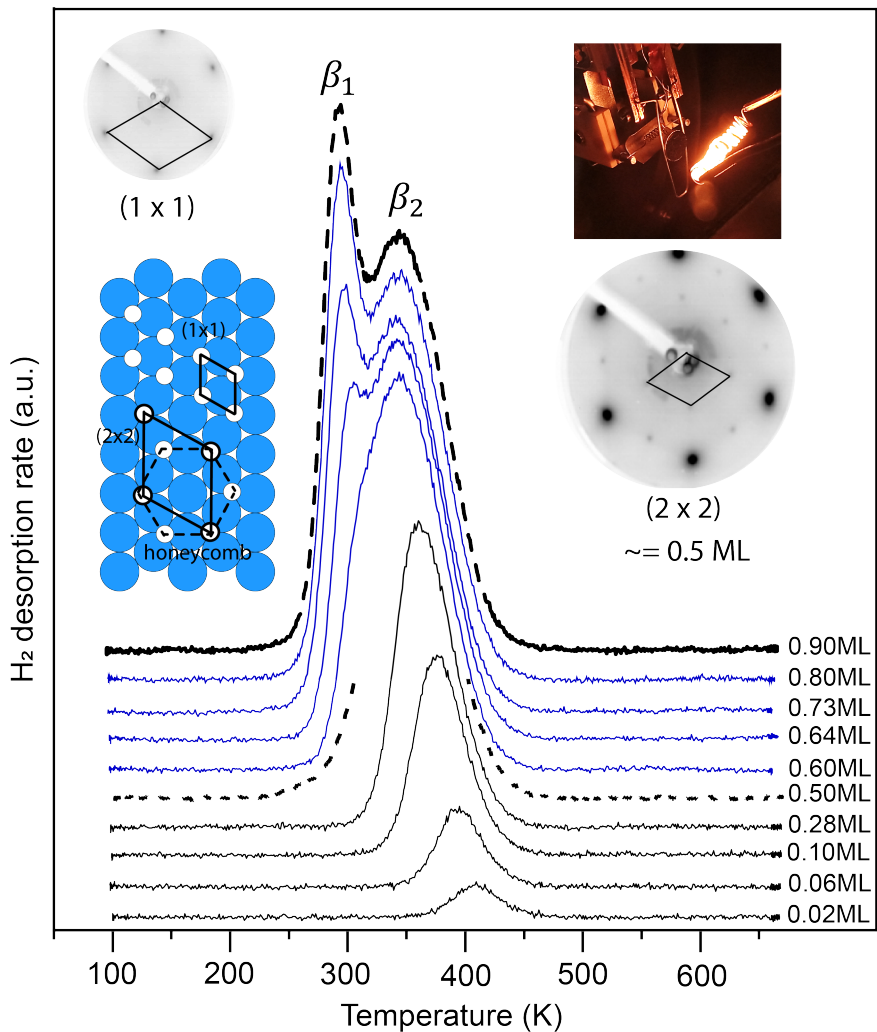


Figure 4.2: A selection of hydrogen TPD spectra obtained by heating the hydrogen covered Co(0001) at  $2 \text{ K s}^{-1}$ . The corresponding LEED structures of the surface covered with 1 ML and 0.5 ML hydrogen on Co(0001) are shown; 1 ML hydrogen on Co(0001) is obtained by dosing hydrogen in presence of a hot W filament, as shown in the inset. The LEED patterns were recorded using 62 eV electron energy. Structure models of the  $(1 \times 1)$ -1H and  $(2 \times 2)$ -2H honeycomb structure are shown on the left.

reaching a maximum intensity around 0.5 ML after which their intensity decreases again<sup>[44]</sup>. In accordance with literature<sup>[44]</sup>, these spots are assigned to (island of) a (2x2)-2H honeycomb structure with local coverage of 0.5 ML.

### 4.4.3 Dosing CO on CO(0001) pre-covered with hydrogen

Here we investigate the amount of CO and  $H_{ad}$  that can co-adsorb on Co(0001) by exposing the sample to varying amounts of hydrogen at 110K followed by a CO dose of around 4 L which is sufficient to populate all the remaining sites with  $CO_{ad}$ . The desorption of hydrogen and CO, recorded while heating the Co(0001) covered with different combinations of  $\theta_H$  and  $\theta_{CO}$ , are presented in fig. 4.3(a,b), where the pure  $H_{ad}$  (1 ML) and pure  $CO_{ad}$  (0.58 ML) layers are represented by dotted spectra, respectively.

For hydrogen coverages below 0.25 ML, a single  $H_2$  desorption peak is observed at 300 K, 50 K lower than for the same quantity of  $H_{ad}$  desorbing from the CO-free surface (see fig. 4.2). The intensity of this peak increases with increasing hydrogen pre-coverage while the peak maximum remains constant around 270 - 280 K which is identical to that of the low temperature peak seen for the pure 1 ML  $H_2$  desorption spectrum. The CO desorption spectra for the co-adsorbed system, provided in fig. 4.3(b), show slight variations compared to the reference case without  $H_{ad}$ . All three desorption peaks show a decrease in intensity as the hydrogen pre-coverage increases, while only the two CO desorption peaks below 350 K change their shape significantly, in particular the sharp desorption peak at 240 K which broadens and shows a slight downward shift.

The desorption spectra show a clear change when the hydrogen pre-coverage exceeds 0.25 ML  $H_{ad}$ : an additional high-temperature shoulder develops in the  $H_2$  desorption spectra, while in the CO desorption spectra, the shape of the peaks below 350 K are more significantly changed as compared to the pure CO spectrum in this coverage regime.

The impact of CO on the  $H_2$  desorption peak temperature decreases with increasing  $H_{ad}/CO_{ad}$  ratios, leading to the emergence of a high-temperature shoulder in the  $H_2$  desorption spectrum for the higher  $H_{ad}/CO$  ratios. These observations can be rationalized when we consider the findings of Lewis et al.<sup>[145]</sup> about co-adsorption of CO and hydrogen on the close-packed cobalt surface. Their STM measurements at low temperature show that CO adsorption onto a hydrogen-covered surface leads to the compression of the hydrogen adlayer into segregated islands with a local (1x1) structure, while the remaining areas are solely covered by CO. In our experiments, the quantities of H and CO that can co-adsorb can also be understood from the seg-

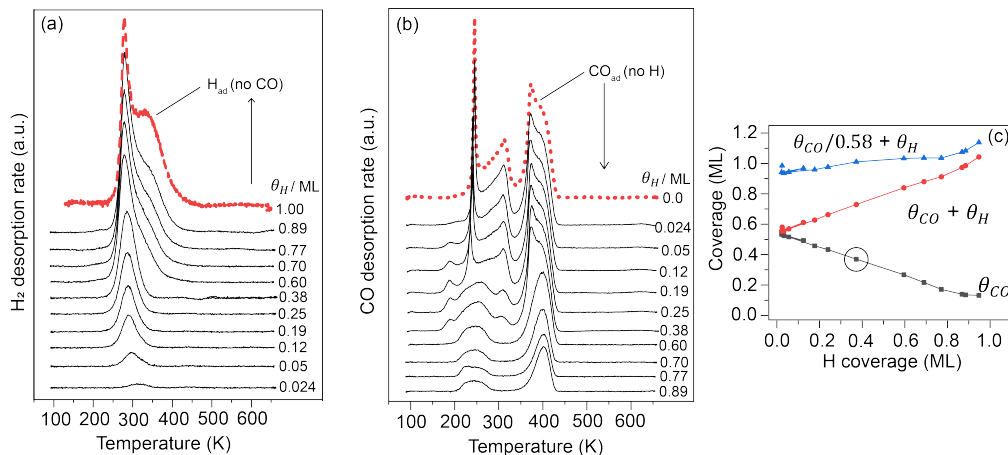


Figure 4.3: Selection of TPD spectra of (a) H<sub>2</sub> and (b) CO, from Co(0001) after pre-adsorbing increasing quantities of H<sub>ad</sub>, followed by a saturation dose of CO. (c) Quantification of the  $\theta_H$  -  $\theta_{CO}$  correlation from the spectra shown in (a)

regation model. Since hydrogen forms islands with a local coverage of 1 ML, the global hydrogen coverage derived from the TPD experiment corresponds to the fraction of the surface taken up by hydrogen. The remaining sites are occupied by CO, and considering that the maximum attainable CO coverage under these conditions is 0.58 ML, the sum of  $\theta_H + (\theta_{CO}/0.58)$  is expected to be unity. Fig. 4.3 (c) indeed demonstrates that this sum remains approximately constant at a value of 1, thereby providing quantitative validation of the segregation model. Hence, our results indicate that a single-site model is not sufficient to explain CO-H coadsorption on the flat Co(0001) surface, as the saturation coverages of the two adsorbates do not add up to unity. In the single-site model each adsorbed species (CO or hydrogen) is considered to interact with the metal surface independently, meaning that only one type of adsorbate can occupy a particular site at a given time, without significant lateral interactions between neighboring adsorbed molecules.

The desorption spectra show a complex evolution as a function of adsorbate coverage. To better understand the underlying dynamics at the surface the co-adsorption system of 0.5 ML H and 0.27 ML CO was chosen for further study by a combination of TPD, IR spectroscopy and LEED. Fig. 4.4(a) shows IR spectra and the corresponding LEED patterns obtained at 110 K after briefly heating the co-adsorbed system to the indicated temperatures. The desorption spectra of H<sub>2</sub> and CO, shown in fig 4.3, were used to derive the CO and H coverage at each temperature during heating, as shown in fig. 4.4 (b).

The LEED after heating to 170 K shows a blurred  $(2\sqrt{3} \times 2\sqrt{3})R30^\circ$  pattern which

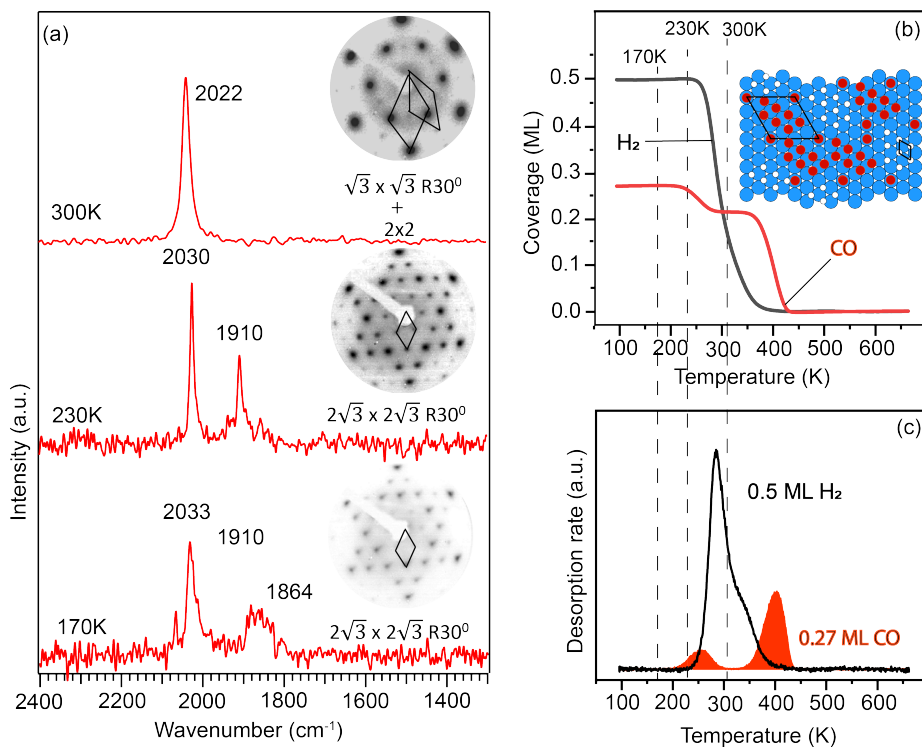


Figure 4.4: IR spectra recorded at 110 K after heating the Co(0001) covered with first hydrogen followed by CO to the temperature indicated alongside each spectra. The corresponding LEED structures are shown next to the IR spectrum, (b) Change in  $\theta_H$  (black) and  $\theta_{CO}$  (red) with temperature derived by integrating the desorption curves in (c); inset - Structure models of Co(0001) covered with CO and hydrogen arranged into separate islands with (1x1) - H and  $(2\sqrt{3} \times 2\sqrt{3}) R30^\circ$  structure are shown in the inset on top right. The dotted lines are presented to aid the ease of comparing different states in the desorption curves with the corresponding IR spectrum

indicates that the  $(2\sqrt{3}\times 2\sqrt{3})R30^\circ$  structure is somewhat disordered. The IR spectra show peaks at  $2033\text{ cm}^{-1}$ ,  $1910\text{ cm}^{-1}$ , and  $1864\text{ cm}^{-1}$  attributed to CO adsorption on-top, bridge, and hollow sites, respectively<sup>[52]</sup>. In the well-ordered  $(2\sqrt{3}\times 2\sqrt{3})R30^\circ$  structure only top and bridge sites are occupied, and the presence of hollow site occupation is taken as an indication that the  $(2\sqrt{3}\times 2\sqrt{3})R30^\circ$  structure is not present everywhere and co-exists with a disordered CO phase in which hollow sites are also occupied.

Heating the co-adsorbed system to 230 K causes a small quantity of CO to desorb (shown by the decrease in the integrated spectra of CO in fig. 4.4 (b) and fig. 4.4 (c)) and the sharpening of the  $(2\sqrt{3}\times 2\sqrt{3})R30^\circ$  LEED pattern. The corresponding IR spectra of this state shows that CO occupies only top (peak at  $2030\text{ cm}^{-1}$ ) and bridge (peak at  $1910\text{ cm}^{-1}$ ) sites, an indication that the  $(2\sqrt{3}\times 2\sqrt{3})R30^\circ$  (local coverage of 0.58 ML) structure is now the dominant CO phase. The fraction of the surface covered by CO at this point is  $0.23/0.58 = 0.40$ . Therefore, 60% of surface is left for hydrogen adsorption. Since hydrogen did not desorb yet, the 0.5 ML  $H_{ad}$  that was initially present occupies 60% of the surface so that the local coverage is 0.83 ML, i.e. hydrogen will predominantly form a local (1x1) structure (as illustrated in the inset of fig. 4.4 (b)).

Hydrogen desorption starts at 250 K, which is accompanied by the desorption of 0.15 ML CO. The hydrogen atoms are more weakly bound in the compressed  $H_{ad}$  islands with 1 ML coverage which explains the downward shift of the  $H_2$  desorption peak maximum caused by  $CO_{ad}$ . At  $\sim 300$  K, the CO desorption stops while a change in the slope of the integrated hydrogen curve is seen. The IR spectra at this stage shows one peak at  $2022\text{ cm}^{-1}$  due to CO adsorbed on top, and the LEED pattern shows the presence of a  $(\sqrt{3}\times\sqrt{3})R30^\circ$  structure alongside a (2x2) structure. The amount of CO left on the surface after desorption is 0.214 ML, which, according to the LEED arranges itself in  $(\sqrt{3}\times\sqrt{3})R30^\circ$  islands with a local coverage of 0.33 ML. The fraction of the surface left for hydrogen adsorption =  $1 - (0.214/0.33) = 0.35$ . The global coverage of hydrogen at 300 K is 0.20 ML and since it sits on 35% of the surface, the local coverage is  $0.2/0.35 = 0.57$  ML  $H_{ad}$  which then explain the (2 x 2) spots in LEED. This implies that the shoulder at high temperature in the hydrogen desorption curve represents hydrogen desorbing from the parts covered by the (2x2)-2H islands<sup>[146]</sup> and it is therefore expected to be similar to the desorption of 0.5 ML pure hydrogen from the Co(0001) surface (fig. 4.2), which also forms a (2x2) structure. However, a detailed comparison shows that the presence of CO has a slight destabilizing effect on the (2x2) hydrogen islands. This destabilizing effect is more prominently visible in fig. 4.5. and will be discussed there in the next section. For the CO desorption spectrum, no further changes with respect to peak shape or position compared to spectra without co-adsorption can be noted for the desorption peak above 300 K.

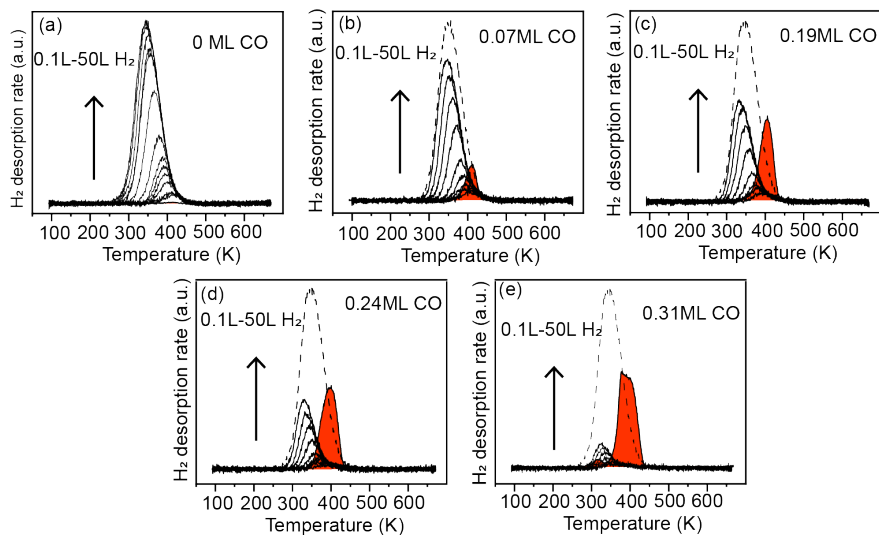


Figure 4.5: (a) Thermal desorption spectra from Co(0001) of hydrogen adsorbed at 110K on various fractional coverages of CO. The initial coverage of CO was accomplished by exposing the surface to CO at 110K :  $\theta_{CO}$  (a) 0 ML, (b) 0.07 ML, (c) 0.19 ML, (d) 0.24 ML, (e) 0.31 ML. the corresponding CO TPD spectra are shaded in red

In summary, our investigation reveals an initial surface state marked by segregation of pure CO and pure hydrogen islands, characterized by a  $(2\sqrt{3} \times 2\sqrt{3})R30^\circ$  arrangement with a local coverage of 0.58 ML for CO, and a  $(1 \times 1)$  structure with a local coverage of 1 ML for hydrogen. The desorption spectrum's profile can be understood from the composition of this surface layer. Upon raising the surface temperature, CO molecules begin to desorb at a temperature slightly lower than the desorption temperature observed for the  $(2\sqrt{3} \times 2\sqrt{3})R30^\circ$  structure. Simultaneously, hydrogen molecules start to desorb at a temperature consistent with desorption from the H-only covered surface when the coverage is around 1 ML. As the coverage of both hydrogen and CO decreases, CO molecules form  $(\sqrt{3} \times \sqrt{3})R30^\circ$  islands, and hydrogen forms  $(2 \times 2)$ -2H islands. The desorption of CO stops, while hydrogen desorption continues at a temperature typical for surfaces covered with  $(2 \times 2)$ -2H structures, albeit at a slightly reduced temperature due to the presence of CO islands, which destabilize the hydrogen islands.

#### 4.4.4 Dosing H<sub>2</sub> on Co(0001) pre-covered with CO

Several studies on other metals indicate that CO suppresses dissociative H<sub>2</sub> adsorption<sup>[142-145]</sup>. The effect of CO<sub>ad</sub> on the dissociative adsorption of hydrogen on

Co(0001) was investigated at 110 K by first dosing a specific quantity of CO, followed by exposure to increasing doses of hydrogen. Fig. 4.5 (a-e) shows a selection of hydrogen TPD spectra for different CO pre-coverages. The dotted spectra represent the spectrum of a 0.5 ML  $H_{ad}$ -covered surface for reference, while the CO desorption peak, which remains constant irrespective of hydrogen coverage, is provided by the red-filled spectra. The area under each hydrogen desorption spectrum was used to quantify the hydrogen adsorbed alongside pre-adsorbed CO in fig. 4.6 and is plotted for different quantities of CO in fig. 4.7 (a).

Firstly, we observed a decrease in the total amount of hydrogen that can co-adsorb with CO as the CO coverage increases. This trend is clearly visible when comparing spectra in fig. from 4.5 (a) to 4.5 (e). For  $\theta_{CO} \geq 0.31$  ML (fig. 4.5 (e)), the amount of hydrogen adsorbed is negligible, with only 0.05 ML of  $H_{ad}$  adsorbed alongside 0.31 ML of CO. This is significantly lower than the 0.38 ML of  $H_{ad}$  (blue curve in fig. 4.7 (a)) that could co-adsorb alongside 0.38 ML CO when hydrogen was dosed first. It is clear from the results that adsorbed CO has a significant impact on the hydrogen adsorption process. More specifically, we see that the maximum coverage reached on the surface pre-covered with CO is lower than when hydrogen is dosed first as illustrated in fig. 4.7 (b). In the previous section it was found that hydrogen and CO form segregated islands where different local coverages are possible. For the dataset where  $H_2$  was dosed after CO, it can be seen in fig. 4.7 (b) - red trace that the combined fraction of the surface covered with CO and H ad-islands is always unity when we assume that a combination of  $(\sqrt{3} \times \sqrt{3})R30^\circ$  CO islands and  $(2 \times 2)$  hydrogen islands is formed on the surface. This assumption was corroborated by IR and LEED for the co-adsorption system with 0.19 ML pre-adsorbed CO followed by a high dose of  $H_2$  (which results in 0.24 ML  $\theta_H$ ), as shown in the fig. 4.8.

The LEED pattern showed a well-ordered  $(\sqrt{3} \times \sqrt{3})R30^\circ$  and  $(2 \times 2)$  structures. The IR spectrum in fig. 4.8 after heating to 210 K shows a narrow peak at  $2015 \text{ cm}^{-1}$  attributed to CO adsorbed on top sites while LEED showed a well-ordered  $(2 \times 2)$  pattern superimposed with a  $(\sqrt{3} \times \sqrt{3})R30^\circ$  pattern. These observations are consistent with the presence of CO islands with a local  $(\sqrt{3} \times \sqrt{3})R30^\circ$  structure and a local coverage of 0.33 ML while a  $(2 \times 2)$  structure was formed with the local coverage of 0.5 ML within the H-islands<sup>[44]</sup>. For a CO coverage of 0.19 ML, this model implies that the fraction of the Co(0001) covered with CO-islands is 52% (0.19 ML/0.33 ML), leaving 48% of the surface available for hydrogen to adsorb. TPD quantification shows a global coverage of 0.24 ML  $H_{ad}$  on 48% of the surface, i.e. a local coverage of 0.5 ML within the hydrogen islands.

In summary, the quantity of H that can be adsorbed when  $H_2$  is dosed on CO-covered Co(0001) can be rationalized from the segregation model where CO blocks part of the surface by forming a local  $(\sqrt{3} \times \sqrt{3})R30^\circ$  structure.  $H_2$  can only disso-

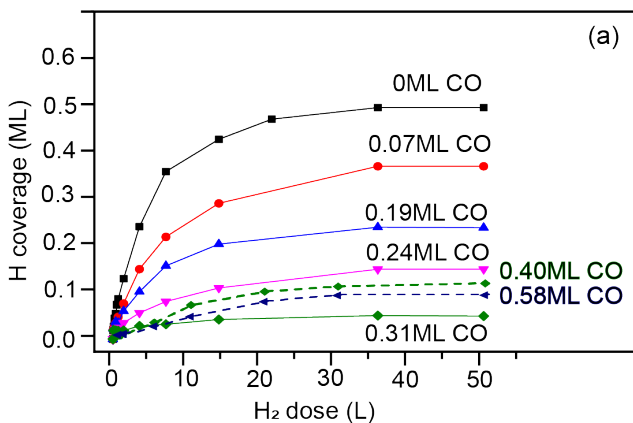


Figure 4.6: (a) Uptake curves (solid) of  $\theta_H$  determined by quantification of the area under the curves in fig. 4.5 (a) to (e) with corresponding pre-adsorbed CO mentioned alongside each curve, dotted curves represent the uptake curves obtained by dosing hydrogen in the presence of the filament

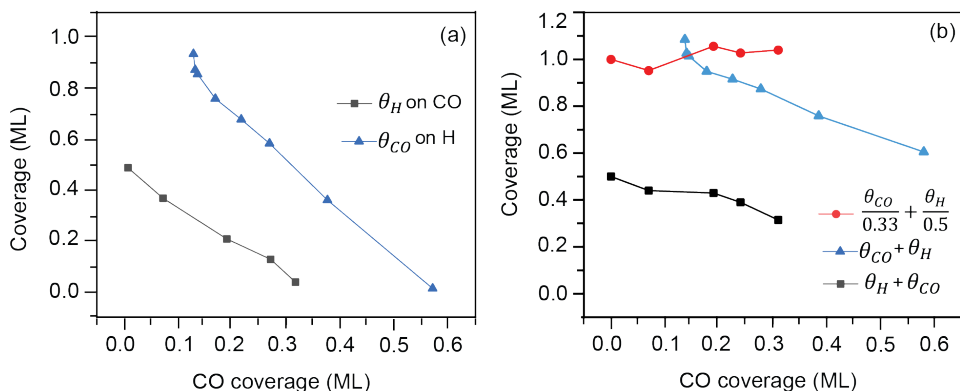


Figure 4.7: (a) CO adsorption followed by hydrogen adsorption (black curve) and hydrogen adsorption in the presence of the tungsten filament followed by CO adsorption (blue curve) (b) Summation of the fraction of the surface covered with CO and hydrogen islands (red trace), total  $\theta_{CO}$  and  $\theta_H$  when hydrogen is dosed on the Co(0001) surface before CO and total  $\theta_{CO}$  and  $\theta_H$  when CO is dosed on the Co(0001) before hydrogen

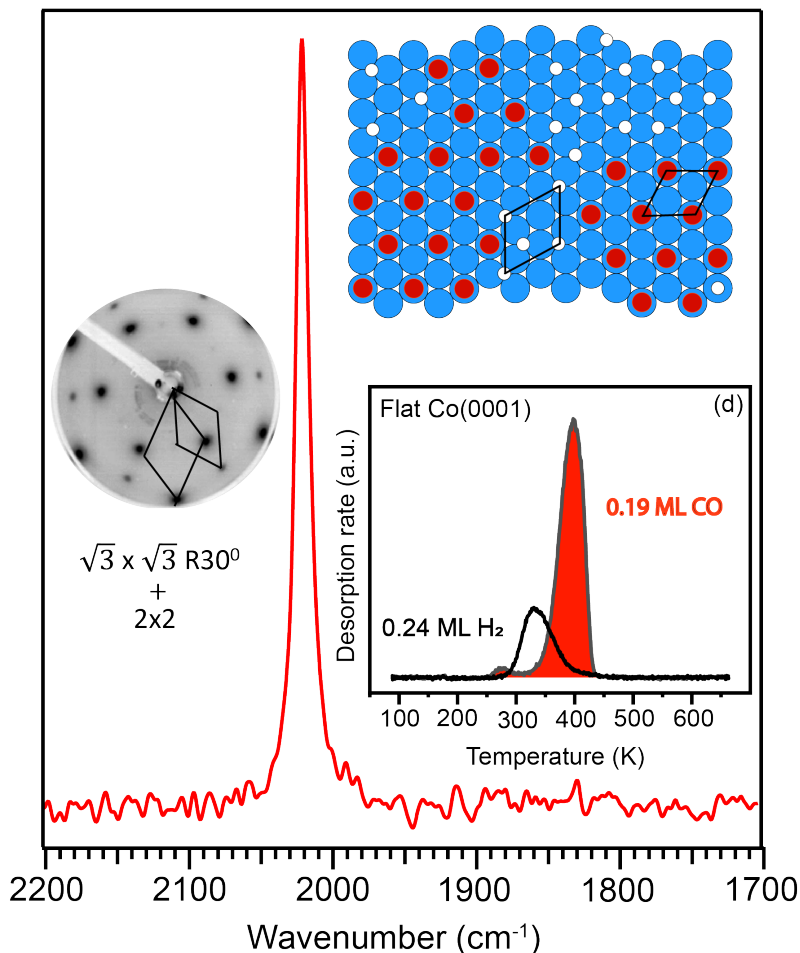


Figure 4.8: IR spectrum of Co(0001) covered with 0.19 ML CO followed by 0.24 ML hydrogen. The corresponding LEED image of the cold sample after heating the surface to 210 K is shown on the left side of the IR spectrum, inset on the bottom right. Comparison of CO and hydrogen TPD spectra obtained by heating this co-adsorbed system at  $2\text{Ks}^{-1}$ . Structure models of Co(0001) covered with 0.19 ML CO and 0.24 ML hydrogen arranged into separate islands with  $(2 \times 2)\text{-}2\text{H}$  and  $(\sqrt{3} \times \sqrt{3})R30^\circ$  structure are shown in the inset on top right.

ciate on the remaining part of the surface and, just like on the clean surface, it can only populate the surface up to a local coverage of 0.5 ML. This also makes the basis of calculating the data points of the red curve in fig. 4.7(b). The adsorbed hydrogen does not compress the pre-adsorbed CO layer into more compact high local coverage ( $2\sqrt{3} \times 2\sqrt{3}$ )  $R30^\circ$  CO islands to free up the space.

The desorption spectra show that hydrogen desorption from the (2x2) hydrogen islands is still affected by the concentration of CO, despite the fact that the two adsorbates are segregated. It can be seen in fig 4.5 that the hydrogen desorption peak maximum shifts to the lower temperature as the CO/H ratio increases, indicating a progressive weakening of the hydrogen adsorption strength. We rationalize this as follows: the segregation of CO and hydrogen into distinct ad-islands suggests that repulsive interactions exist between CO and  $H_{ad}$ . A higher CO/H ratio in the segregated system means that the hydrogen islands are comparatively smaller so that the fraction of H at the interface between the islands, which is in direct contact with the CO, is also larger. Their weaker binding causes them to desorb at a lower temperature so that the desorption spectrum shifts to lower temperature with increasing CO coverage. These findings align with previous studies conducted on Ru(001)<sup>[152]</sup>, where it was suggested that CO inhibits hydrogen adsorption, as well as on similar closely packed transition metal surfaces like Rh(111)<sup>[153]</sup>, where it was concluded that hydrogen and CO undergo near-complete segregation.

To gain a deeper understanding of the influence of CO on the kinetics of dissociative  $H_2$  adsorption, the hydrogen uptake curves in the presence of CO were recorded. As the surface pre-coverage of CO increases, the global hydrogen coverage decreases, as evidenced in fig. 4.7 (a) by the decreasing slope as the CO coverage increases. This raises the question whether this decrease is primarily caused by CO blocking adsorption sites or by alterations to the electronic structure of the surface leading to changes in the barrier for hydrogen dissociation, or a combination of both factors. To shed light on potential electronic effects, we analyze the normalized uptake curves (fig. 4.9), which accounts for the maximum coverage achievable at a specific  $\theta_{CO}$ . As shown in the inset of fig. 4.9, the curves have a similar uptake slope up to a hydrogen dose of 2L, indicating the same sticking probability for hydrogen before repulsive interactions begin except for the  $\theta_{CO}$  of 0.31 ML. Thus, for total surface coverage of  $\leq 0.5$  ML, the rate of adsorption primarily depends on the impinging hydrogen molecule finding an empty site. However, for total surface coverage  $> 0.5$  ML, CO appears to somewhat impede dissociation by altering the electronic structure of the surface in addition to simple site blocking. The results displayed in fig. 4.9 exhibit some scatter, making it challenging to draw definitive conclusions. Therefore, further detailed studies are needed to elucidate how pre-adsorbed CO influences the dissociative adsorption of  $H_2$ .

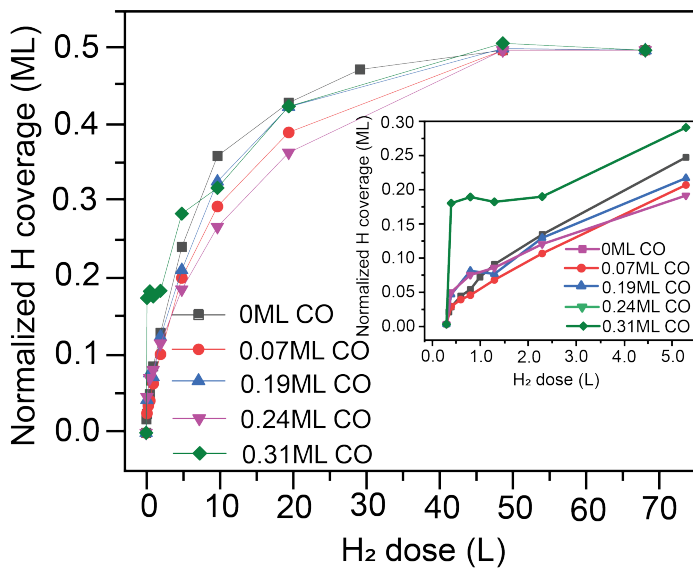


Figure 4.9: Plot of normalized hydrogen coverage versus hydrogen dose, illustrating the impact of changes in electronic structure of Co(0001) due to CO co-adsorption on the dissociative adsorption of hydrogen on Co(0001). The hydrogen uptake curves, normalized to the  $\theta_H$  obtained when hydrogen is adsorbed alone, allow for direct comparison of the slopes across different CO co-adsorption conditions. The inset illustrates the curves zoomed in upto 5L of hydrogen dose. Because of the normalization procedure and low hydrogen signal at 0.31 ML, this data set is unreliable

When CO is dosed first followed by hydrogen, we find that that 0.24 ML  $H_{ad}$  can be adsorbed alongside 0.19 ML  $CO_{ad}$ . Conversely, when H is dosed first 0.19 ML of CO can be adsorbed on a surface precovered with 0.7 ML of H - a factor of 3 increase in the coadsorbed H coverage. To investigate this phenomenon further, we conducted experiments where the Co(0001) surface pre-covered with 0.19 ML CO was exposed to hydrogen in the presence of a tungsten filament. The IR spectrum after heating to 210 K shows a narrow peak at  $2015\text{ cm}^{-1}$  attributed to CO adsorbed on top sites while LEED showed a well-ordered  $(\sqrt{3}\times\sqrt{3})R30^\circ$  pattern as shown in fig. 4.10. The observed phenomena can be explained by the formation of CO islands exhibiting a local  $(\sqrt{3}\times\sqrt{3})R30^\circ$  structure with a local coverage of 0.33 ML<sup>[154]</sup>. According to this model, when the CO coverage is 0.19 ML, approximately 52% of the Co(0001) surface is covered by CO islands (0.19 ML/0.33 ML), leaving 48% of the surface available for hydrogen adsorption. Through TPD quantification, a global coverage of 0.42 ML of hydrogen is observed on this 48% region of the surface, indicating a local coverage of approximately 1 ML within the hydrogen islands. This interpretation is consistent with the presence of the low temperature desorption peak (280 K) in the hydrogen spectra which is comparable to hydrogen desorption from a surface covered by 1 ML  $H_{ad}$ . Consequently, if the segregation model holds true, the local coverage of 1 ML within the H-islands<sup>[44]</sup> would result in a (1x1) structure within the hydrogen islands.

In summary, we find that when hydrogen is dosed after CO, the hydrogen only occupies the space that is left by the  $(\sqrt{3}\times\sqrt{3})R30^\circ$  islands of CO. When  $H_2$  is dosed, only half of the potentially available area for hydrogen on the Co(0001) surface is covered with hydrogen. However, using a hot filament increases hydrogen coverage up to 1 ML on these areas also corresponding to (1x1) islands of hydrogen. When CO is dosed on Co(0001) after hydrogen, it can compress hydrogen into (1x1) islands while simultaneously forming a  $(2\sqrt{3}\times 2\sqrt{3})R30^\circ$  structure within the CO islands. When hydrogen is dosed in the presence of a hot filament onto Co(0001) pre-covered with CO, it does not compress CO into the  $(2\sqrt{3}\times 2\sqrt{3})R30^\circ$  structure. We do not observe compression of the CO layer into denser structures to accommodate more hydrogen. This indicates that the hot hydrogen molecules with a higher reactivity for dissociation generated by dosing the hydrogen in the presence of a hot tungsten filament enhances the overall global coverages of hydrogen on the Co(0001) surface.

Although the method of dosing hydrogen in the presence of a tungsten filament is not applicable during FTS, it allows surface scientists to study structures forming under 'real' hydrogen pressures which may lead to similar coverages on the catalyst surface relevant to FTS. It is essential to note that not all CO molecules and hydrogen atoms segregate into islands. Consequently, a minor discrepancy in determining  $\theta_H$  from the fraction of the surface covered by CO may arise. The majority of

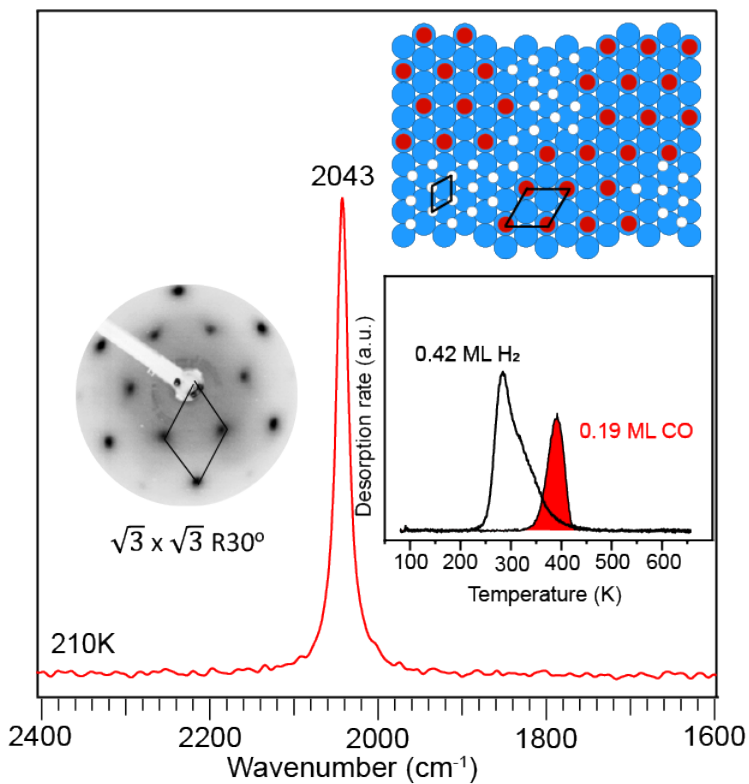


Figure 4.10: IR spectrum of Co(0001) covered with 0.19 ML CO followed by 0.42 ML hydrogen. The corresponding LEED image is shown on the left side of the IR spectrum, inset - Comparison of CO and hydrogen TPD spectra obtained by heating this system at 2Ks<sup>-1</sup>. Structure models of the (1x1)-1H and ( $\sqrt{3} \times \sqrt{3}$ )R30° structure are shown on the inset

CO molecules and hydrogen atoms, however, preferentially segregate into islands, establishing ordered structures that are discerned through LEED analysis.

## 4.5 Summary and conclusions

This chapter provides a detailed investigation into the non-reactive interaction between CO and hydrogen on the Co(0001) using TPD, IR and LEED surface which is crucial for understanding the fundamental steps involved in FTS. For CO alone, the site occupancy of top, hollow, and bridge sites on the surface undergoes significant variations as the CO coverage increases. Up to a coverage of 0.33 ML, only the top sites are occupied. Subsequently, between 0.33 and 0.55 ML, a combination of top and hollow site occupation is observed. As the coverage approaches 0.55 - 0.58 ML, a transition to a bridge-top configuration occurs. The sequential depopulation of the CO-covered surface during heating in vacuum mirrors the occupancy sequence observed during the  $\text{CO}_{ad}$  build-up upon exposure to CO at low temperatures. The high-coverage bridge-top structure, corresponding to 0.58 ML, exhibits stability up to 180 K. Upon further heating additional CO desorbs around 240 K, resulting in a configuration with 0.5 ML  $\text{CO}_{ad}$  in a top-hollow arrangement. Further heating results into a gradual desorption of CO, accompanied by an increase in the top/hollow ratio. At 320 K, the remaining 0.33 ML  $\text{CO}_{ad}$  is adsorbed in the top position, ultimately desorbing during continued heating up to 400 K.

Exposure to hydrogen at low temperatures, shows that dissociative hydrogen adsorption is activated, resulting in a low dissociative sticking probability at low surface temperature. This kinetic limitation also makes it difficult to reach a hydrogen coverage above 0.5 ML in UHV experiments. When hydrogen is dosed in the presence of a high-temperature tungsten filament (1600 K), placed close to the sample surface, 'hot' hydrogen molecules and atoms capable of surmounting the dissociation barrier are generated. This approach allows the attainment of hydrogen coverages beyond 0.5 ML. Excess hydrogen above 0.5 ML desorbs in a distinct low-temperature desorption peak. LEED shows the formation of adsorbate islands exhibiting a (2x2)-2H honeycomb structure within the 0.3 to 0.8 ML coverage range, signifying a broad coverage regime indicative of the special stability of this structure. As the hydrogen coverage approaches 1 ML, a transition to a (1x1)-1H structure is observed.

Our results indicate that a model assuming that each surface site is occupied by CO and hydrogen (single-site model) is not sufficient to capture the complexity of CO-H co-adsorption, as the saturation coverages of the two adsorbates do not add up to unity. By considering adsorbate segregation into ad-islands, we were able to

obtain a reasonable quantitative description of the correlation between  $\theta_H$  and  $\theta_{CO}$  values in our model system. Our proposed model shows that the co-adsorption of hydrogen and CO on Co(0001) can yield high adsorbate coverages ( $\sim 1$  ML). The segregation model suggests that, irrespective of exposure sequence or surface coverage, CO and H segregate into islands on the Co(0001) surface, with the adsorption capacity of the surface determined by the local coverage within these islands. The co-adsorption system are effectively studied using LEED patterns and corresponding IR spectra, highlighting the local coverages of CO and hydrogen.

We observed a reduction in the adsorption capacity for CO as the hydrogen coverage increases, particularly at a temperature of 110 K where CO desorption is impossible. When hydrogen is dosed first followed by CO, the CO compresses the hydrogen into  $(1 \times 1)$  islands and forms a  $(2\sqrt{3} \times 2\sqrt{3})R30^\circ$  structure in the islands itself. This is shown by IR peaks at  $2033 \text{ cm}^{-1}$ ,  $1910 \text{ cm}^{-1}$ , and  $1864 \text{ cm}^{-1}$ , attributed to CO adsorption on-top, bridge, and hollow sites, respectively. When heated, during desorption the structure within the CO islands transitions from  $(2\sqrt{3} \times 2\sqrt{3})R30^\circ$  structure to a  $(\sqrt{3} \times \sqrt{3})R30^\circ$  pattern when the local  $\theta_{CO}$  is  $\leq 0.33$ . This is seen by an IR peak at  $2015 \text{ cm}^{-1}$ . When hydrogen is introduced after CO, hydrogen atoms occupy the parts of Co(0001) not occupied by CO islands. Specifically, only 0.5 ML of hydrogen is adsorbed on the available part of the surface when  $H_2$  is dosed. The CO forms a  $(\sqrt{3} \times \sqrt{3})R30^\circ$  structure within the CO islands. When hydrogen is dosed in the presence of a hot filament on the CO covered Co(0001), we see that hydrogen arranges itself in  $(1 \times 1)$  structure with H islands whereas CO forms a  $(\sqrt{3} \times \sqrt{3})R30^\circ$  pattern, i.e. H does not compress the CO into  $(2\sqrt{3} \times 2\sqrt{3})R30^\circ$  structure. This suggests that the existing CO arrangement remains unchanged to accommodate additional hydrogen adsorption. The arrangement within hydrogen islands is determined via LEED, namely  $(1 \times 1)$ -1H and  $(2 \times 2)$ -2H, corresponding to local  $\theta_H$  values of 1 ML and 0.5 ML, respectively. The  $\theta_H$  is determined by the available surface space following CO island formation. Our description of the co-adsorption system, grounded in the segregation model, integrates these CO and H local structures within the islands. This shows that the interactions between CO-CO and H-H are stronger than the interaction between CO-H.

It is worth noting that a significant amount of CO can still be adsorbed on Co(0001) surface that is covered with the amount of  $H_2$  obtained under UHV-like conditions with  $(H_{ad})$ , while very little H adsorption occurs on a surface saturated with COad. This can be attributed to the fact that the sites for dissociative hydrogen adsorption may be occupied by CO or rendered inaccessible by neighboring CO molecules, leading to an increased barrier for dissociative adsorption of hydrogen. These findings offer insights into the behavior of CO and hydrogen on Co(0001) surfaces, which can aid in the optimization of FTS.

## 4.6 Abbreviations

1.  $\text{CO}_{ad}$  Adsorbed CO
2.  $\text{H}_{ad}$  Adsorbed hydrogen
3. IR Infrared
4. LEED Low energy electron diffraction
5. ML Monolayer
6. QMS Quadrupole mass spectrometer
7. STM Scanning tunneling microscopy
8. TPD Temperature programmed desorption
9.  $\theta_{CO}$  CO coverage
10.  $\theta_H$  Hydrogen coverage

## Chapter 5

# CO and hydrogen co-adsorption on Co(11 $\bar{2}$ 9)

### 5.1 Abstract

Cobalt catalysts play a pivotal role in large-scale production of synthetic fuels through the Fischer-Tropsch synthesis process. During this reaction, long chain hydrocarbons are formed by reaction of adsorbed CO molecules and hydrogen atoms on a catalyst surface that is covered with these adsorbates. Thus, it is interesting to study how lateral interactions between these adsorbates affect the stability and reactivity of the catalyst. In this investigation, we explore the adsorption of hydrogen, CO, and their co-adsorption on the kinked Co(11 $\bar{2}$ 9) surface and draw comparisons with the flat Co(0001) surface to elucidate the influence of the undercoordinated sites on the dissociative adsorption of hydrogen and its co-adsorption with CO. The desorption temperature of hydrogen is lower on kinked surfaces compared to the Co(0001) surface because the stepped and kinked sites offer a barrierless route for dissociative adsorption of hydrogen, unlike the small barrier present on the flat Co(0001) surface. It is also found that the presence of pre-adsorbed CO molecules impedes dissociative hydrogen adsorption on both Co(0001) and Co(11 $\bar{2}$ 9) surfaces. This is either due to the occupation of the sites for dissociative hydrogen adsorption by CO or that the sites rendered inaccessible by neighboring CO molecules, leading to an increased barrier for dissociative adsorption of hydrogen. However, even when the Co(11 $\bar{2}$ 9) surface is saturated with CO, we observed that some hydrogen molecules can still dissociate, unlike the flat Co(0001) surface where hydrogen adsorption is completely blocked on the surface covered with 0.33 ML CO. This phenomenon is attributed to the step sites on the Co(11 $\bar{2}$ 9) surface, which remain vacant, allowing hydrogen to adsorb onto a CO-saturated surface.

## 5.2 Introduction

This chapter investigates the dissociative adsorption of hydrogen, the influence of CO on this process, and the interaction between adsorbed CO and hydrogen atoms. The goal is to understand how the kinked sites of Co catalyst influence the lateral interactions between these reactants and affect their adsorption during Fischer-Tropsch synthesis (FTS). Using single-crystal surfaces, we examine the individual and combined adsorption behaviors of CO and hydrogen under conditions (UHV) where the formation of hydrogenated products is negligible. These surfaces expose well-defined sites with known concentrations, allowing us to study how atomic structure influences reactivity. This simplified context provides insights into surface reactions at the molecular level, exceeding what is currently achievable in more complex reaction systems.

It is well-established that defects, such as step sites, significantly influence surface reactivity<sup>[77,133,155]</sup> as the sites often exhibit a pronounced propensity to induce the dissociation of molecules upon adsorption<sup>[156–158]</sup> and stronger bonding of the adsorbates due to their lower atomic coordination. However, when multiple adsorbates are co-adsorbed on a surface, their mutual interactions can modify the adsorption landscape, leading to site blocking, which can impede the occupation of critical active sites.

The co-adsorption of CO and H can lead to the emergence of either a segregated layer, where the adsorbates form isolated islands on the surface, or a mixed layer characterized by randomly mixing or ordering of CO and H<sup>[159]</sup>. The outcome is determined by the relative strength of the adsorbate-adsorbate and adsorbate-substrate interactions<sup>[159]</sup>. Since a segregated layer consists of patches of pure component, its properties (vibrational and electronic) are expected to be the (weighted) sum of the properties of the pure CO and H systems. Synergistic effects are, however, likely in a mixed adlayer due to CO-H interactions. In a mixed layer, each hydrogen atom is influenced by adjacent adsorbed CO molecules<sup>[160]</sup>. Other effects contribute to complex behavior such as blocking of hydrogen adsorption by CO<sup>[154,161,162]</sup>, displacement of adsorbed H by CO<sup>[154,163–165]</sup>, changes in the hydrogen desorption temperature upon adsorption of CO<sup>[154]</sup>, and formation of subsurface H and H absorption<sup>[161,166–169]</sup>.

Studies<sup>[159]</sup> on the co-adsorption of CO and hydrogen have been carried out on transition metal surfaces like Pt<sup>[170,171]</sup>, Ir<sup>[172]</sup> and Ni<sup>[173,174]</sup>. In a study conducted by Wang et al.<sup>[170]</sup>, a comparative analysis of CO and hydrogen co-adsorption was carried out on Pt(335)<sup>[170]</sup> and Pt(111) surfaces using electron energy loss spectroscopy (EELS) and TPD. Both CO and hydrogen bind more strongly on the step sites on Pt(335) surface – this observation was used to study the mutual influence by switching the exposure sequence. Dosing hydrogen followed by CO resulted in blocking of the edge sites with H which allowed CO adsorption on the terrace sites. They found that when hydrogen was co-adsorbed on the step sites, it exerted a strong influence on the vibrational spectrum of CO, due to the CO adsorption changing site from

atop to bridge positions on the terrace. Since CO prefers to adsorb on the edge sites on the Pt(335), when hydrogen is dosed after CO, co-adsorbed hydrogen exhibited virtually no effects on CO's vibrational spectrum, even at very high hydrogen coverage. On Pt(111) surface, regions of mixed H and CO one-dimensional islands coexist along the edge of one-dimensional islands of pure CO, mirroring observations on other densely packed surfaces<sup>[175-179]</sup>.

Pd surfaces have exhibited unique characteristics in CO and hydrogen coadsorption, primarily due to the exceptionally strong interaction between Pd and hydrogen, which results in the dissolution of hydrogen into the bulk. Matthias et al. studied CO and hydrogen coadsorption on Pd(111) and revealed that the mutual site blocking of CO and H critically depends on factors such as the type of gas exposure (sequential versus gas mixture) and the exposure temperature<sup>[147]</sup>. When hydrogen was adsorbed on CO-precovered Pd(111) it was shown that CO coverages above 0.33 ML were very effective at preventing dissociative hydrogen adsorption, presumably by increasing the dissociative adsorption barrier because purely geometric considerations cannot explain the observed site blocking<sup>[147]</sup> but can be explained by the electronic site blocking. When CO was adsorbed on hydrogen-precovered Pd(111) the site-blocking ability of hydrogen strongly depended on the substrate temperature. While at 100 K the energy barrier for hydrogen bulk dissolution cannot be overcome hence hydrogen stays on or near the surface and blocks adsorption of CO. At 150 K, the energy barrier can be overcome, allowing CO to displace hydrogen to bulk Pd sites. In contrast, Pd(110) surfaces have been found to exhibit weaker mutual interactions between CO and hydrogen<sup>[166]</sup>.

Experimental evidence supporting the formation of surface complex species like H<sub>2</sub> and CO has been documented on W(100)<sup>[180]</sup> and Ru(110)<sup>[181]</sup> surfaces. However, only limited reports<sup>[182]</sup> are available regarding similar investigations conducted on stepped cobalt surfaces. By conducting co-adsorption experiments on kinked Co(1129) surface and leveraging insights from well-studied low-index Co(0001) surface as described in the previous chapter, we can delve into how the mutual interactions between CO and hydrogen are influenced by step sites.

### 5.3 Experimental setup

The experimental methodology closely resembled the procedure outlined in chapter 4, which focused on the co-adsorption of CO and hydrogen on Co(0001). For monitoring changes in the partial pressure of CO or hydrogen during sticking probability measurements or TPD experiments, a differentially pumped quadrupole mass spectrometer (QMS) was employed. The CO coverage was determined using TPD experiments using Co(0001) as a reference, as explained in section 3.3 of this thesis. The desorption spectrum of 0.5 ML H<sub>ad</sub> on the close-packed surface<sup>[136,150,151,183]</sup> was used as a quantitative reference to determine the hydrogen coverage on the Co(1129)

surface<sup>[175]</sup>.

During the adsorption and desorption experiments, the sample was positioned in close proximity to the small aperture of the quadrupole mass spectrometer (QMS) compartment as shown in fig. 3.7(a), ensuring that a significant proportion of molecules that reach the QMS compartment have interacted with the surface. This configuration enabled a focused examination of the kinetics of adsorption. To illustrate, we discuss a representative experiment depicted in the Fig. 5.1, where CO was introduced into the main chamber, and the  $m/e=28$  mass signal is concurrently monitored by the shielded QMS.

Initially, a substantial fraction of impinging CO molecules adheres to the cold surface, preventing their entry into the QMS compartment. As the surface becomes progressively populated with adsorbed molecules, a growing number of CO molecules rebound from the surface and enter into the QMS compartment, leading to an increase in the  $m/e=28$  signal. From this, we calculated the fraction of impinging molecules that stick to the surface. It is essential to acknowledge that our measurements of the adsorption kinetics are not absolute. Some molecules may directly enter the QMS compartment from the main chamber without undergoing interactions with the surface. Despite this limitation, maintaining a constant sample position allows us to discern relative trends.

The sticking coefficient is defined as the ratio of particles that adsorb to the total number of particles arriving at the surface during the adsorption process. It serves as a key indicator of the influence of adsorbate coverage on subsequent adsorption phenomena. The sticking probability at a specific adsorption time, denoted as "t," can be calculated using the following equation:

$$S(t) = 1 - \frac{P_{shieldedQMS}}{P_{mainchamber}} \quad (5.1)$$

Variables are shown in Fig. 5.1.  $P(t)$  is the increase in partial pressure of the impinging gas over and above  $P_o$ ,  $P_o$  is the initial pressure in the chamber before the introduction of CO and  $P(f)$  is the pressure when the surface is saturated with gas. The numbers presented in Fig. 5.1 correspond to different stages within the experimental sequence: (1) The initial state before gas introduction into the chamber. (2) The subsequent entry of gas into the chamber, leading to molecules impacting the surface. (3) The adsorption of gas on the surface. (4) The point of surface saturation, marking the cessation of further adsorption. The data extracted from the P-t plot can be further transformed into a sticking probability-dose plot, visually depicted in the fig. 5.1 (b) and further on in the chapter, in fig. 5.4 (d) and 5.5 (d). This plot serves as a tool for unraveling insights into the underlying adsorption mechanisms, such as distinguishing between Langmuir dissociative adsorption and precursor-type kinetics, as discussed in subsequent sections.

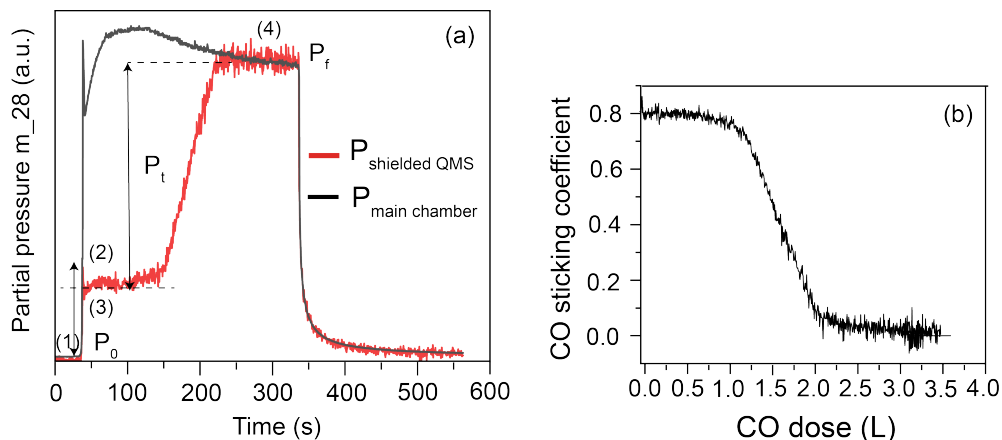


Figure 5.1: MS signal of CO (mass 28) measured by the differentially pumped QMS during a sticking probability measurement at 100 K (red trace). This trace represents the pressure in the shielded QMS chamber. The black trace represents the pressure in the main chamber (b) Sticking coefficient computed using the data in (a) and eq. 5.1

## 5.4 Results

### 5.4.1 CO adsorption on Co(11 $\bar{2}$ 9)

The adsorption of CO on Co(11 $\bar{2}$ 9) was previously discussed in chapter 3 of this thesis where the focus is on the low coverage of CO, and it serves as essential background information for the co-adsorption study presented here. In fig. 5.2, we present CO desorption spectra for various CO coverages, ranging from 0 to 0.645 ML. Inset (a) provides IR spectra acquired at specific temperatures: 310 K (approximately 0.35 ML  $\theta_{CO}$ ), 250 K (approximately 0.42 ML  $\theta_{CO}$ ) and 95 K (around 0.645 ML  $\theta_{CO}$ ). Inset (b) showcases the temperature-induced changes in  $\theta_{CO}$ , as determined by integrating the desorption curve for the 0.645 ML case.

At saturation coverage ( $\theta_{CO} = 0.645$  ML), the IR spectrum exhibits characteristic peaks indicating the occupancy of top sites ( $2080\text{ cm}^{-1}$  and  $2040\text{ cm}^{-1}$ ), twofold bridge sites ( $1920\text{ cm}^{-1}$ ), and hollow sites ( $1830\text{ cm}^{-1}$ ). Notably, no discernible LEED patterns were observed during CO adsorption on Co(11 $\bar{2}$ 9) at 100 K, signifying the absence of long-range ordered structures. As the sample temperature is raised, CO desorption starts at around 140 K. The desorption peak at 250 K corresponds to a shift in the IR spectra, where the signal at  $1920\text{ cm}^{-1}$  disappears, and a distinct peak emerges at approximately  $1825\text{ cm}^{-1}$ , indicating a transition in site occupancy from bridge-top to top-hollow sites. Between 250 and 320 K, a gradual desorption of 0.12 ML CO takes place, leading to the depopulation of the hollow sites and an increase in CO concentration on the top sites. With further temperature increase, the surface undergoes progressive depopulation, and by approximately 450 K, all CO molecules

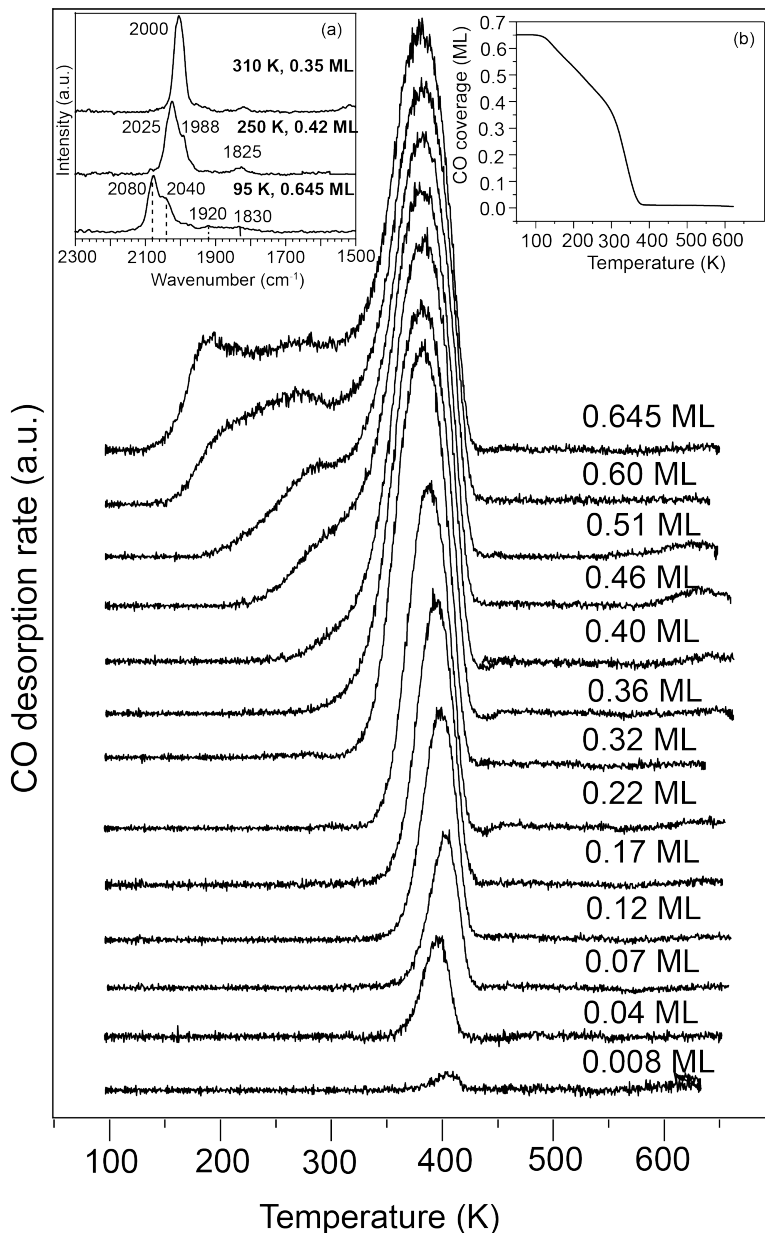


Figure 5.2: Selection of CO TPD spectra obtained by heating the Co(11 $\bar{2}$ 9) covered with CO at 2 Ks<sup>-1</sup>; inset (a) Illustration of the IR spectra at  $\theta_{CO}$  = 0.645 ML CO at 95 K, 0.42 ML CO at 250 K and 0.35 ML CO at 310 K; inset (b) Change of  $\theta_{CO}$  on Co(11 $\bar{2}$ 9) with increasing temperature

have desorbed from the surface.

### 5.4.2 Hydrogen adsorption on Co(11 $\bar{2}$ 9)

Hydrogen adsorption on the kinked Co(11 $\bar{2}$ 9) was studied by dosing H<sub>2</sub> at 110 K. At this temperature, hydrogen molecules undergo dissociation upon adsorption, resulting in a saturation coverage of  $\sim 1$  ML of atomic hydrogen (H<sub>ad</sub>) (inset Fig. 5.3). Weststrate et. al.<sup>[44]</sup> systematically examined a collection of regularly stepped and kinked cobalt surfaces to investigate the influence of undercoordinated sites on dissociative hydrogen adsorption. Their study showed that the sticking probability correlates with the step density, demonstrating approximately a tenfold enhancement on surfaces with around 10% step site atoms, and up to a fortyfold enhancement for surfaces with roughly 40% kinked steps.

Theoretical findings suggest that the process of dissociative hydrogen adsorption on a smooth Co(0001) surface is slightly activated. Additionally, these theoretical results indicate that the presence of hydrogen already adsorbed on the surface hinders the dissociative adsorption of additional hydrogen as the coverage approaches  $\theta_H = 0.5$  ML<sup>[181]</sup>. This phenomenon accounts for the maximum coverage of 0.5 ML of atomic hydrogen (H<sub>ad</sub>) that can be achieved on flat Co(0001) when hydrogen gas is dosed at UHV-like pressures (see chapter 4). When dosing H<sub>2</sub> with a hot tungsten filament (1600 K) placed close to the sample surface, higher coverages on Co(0001) can be achieved since the filament gives the molecules more energy so they have a higher probability to dissociate manifesting as higher sticking coefficient and hence more hydrogen adsorption on the surface. The resultant higher coverage is akin to the influence of steps on the hydrogen adsorption on the kinked Co(11 $\bar{2}$ 9) surface. Hence, hydrogen was not dosed in the presence of a tungsten filament on the Co(11 $\bar{2}$ 9) surface because proximity to the hot filament raises the surface temperature to approximately 130 K, which is near the temperature for the onset of hydrogen desorption. This would risk unintended desorption of hydrogen from the surface.

On heating the kinked Co(11 $\bar{2}$ 9) surface dosed with hydrogen (Fig. 5.3) we see that for  $\theta_H \leq 0.5$  ML, the desorption spectra shows a single desorption peak with second-order desorption characteristics similar to that obtained on Co(0001). The peak for the coverage below 0.5 ML is labeled as the  $\beta_2$  peak, adopting nomenclature akin to Ni(111)<sup>[149,182]</sup>. When the hydrogen coverage exceeds  $> 0.5$  ML, a second desorption peak, labeled as  $\beta_1$ , emerges, at around 240 K. The coverage appears to stabilize at approximately 1 ML after dosing 3L on Co(11 $\bar{2}$ 9). The desorption of hydrogen in the coverage range between 0 ML – 1 ML occurs within a temperature range of 180 to 420 K. The shift of the peak maximum of both  $\beta_1$  and  $\beta_2$  peaks toward lower temperatures with increasing hydrogen coverage is indicative of second-order desorption kinetics, arising from recombinative desorption where two hydrogen atoms recombine to form H<sub>2</sub>(g).

Comparing the desorption spectra obtained from Co(0001) (red spectrum in fig.

5.3) covered with 1 ML of hydrogen to those from the Co(11 $\bar{2}$ 9) surface saturated with hydrogen, the  $\beta_1$  peak exhibit a substantial downward shift relative to its position on Co(0001). This shift is associated with the hydrogen adsorption barrier and can be elucidated by the principle of microscopic reversibility: step sites offer an alternative barrierless pathway to the pathway with barrier on terraces for dissociative adsorption, and by the principle of microscopic reversibility, the desorption barrier is also lowered by an equivalent amount.

### 5.4.3 Dosing CO on Co(11 $\bar{2}$ 9) pre-covered with hydrogen

This section investigates the co-adsorption behavior of CO and  $H_{ad}$  on Co(11 $\bar{2}$ 9). To achieve this, the sample was exposed to varying quantities of hydrogen at 110 K, followed by a CO dose ( $\sim 4$  L) sufficient to occupy all remaining sites with  $CO_{ad}$ . The desorption profiles of both hydrogen and CO for different hydrogen and the associated CO coverages are depicted in fig. 5.4 (a) and (b). In these figures, the spectra corresponding to pure  $H_{ad}$  (0.98 ML) and pure  $CO_{ad}$  (0.645 ML) layers are shown by a dotted green trace for reference.

For a hydrogen coverage of 0.31 ML, a single desorption peak ( $\beta_1$ ) is observed at 260 K after post-dosing CO, which is 50 K lower than the desorption temperature for an equivalent quantity of  $H_{ad}$  on a CO-free surface (as shown in fig. 5.3). The intensity of this peak increases with increasing hydrogen pre-coverage, and the peak maximum shifts to lower temperatures. This behavior is consistent with that of the low-temperature peak ( $\beta_1$ ) observed in the pure  $H_2$  desorption spectrum. The CO desorption spectra for the co-adsorbed system, presented in fig. 5.4 (b), exhibit only subtle variations when compared to the reference case without  $H_{ad}$ . The desorption peaks, except the peak at 380 K, show a decrease in intensity with notable changes observed in the shape of the two CO desorption peaks below 350 K. Specifically, the desorption peak at 180 K vanishes entirely, and the peak at 240 K first experiences an intensity increase and subsequently disappears as the co-adsorbed hydrogen coverage increases.

The hydrogen desorption spectra undergo significant changes when the hydrogen pre-coverage surpasses 0.64 ML  $H_{ad}$ . At this point, an additional high-temperature shoulder emerges in the  $H_2$  desorption spectra which has been attributed to the hydrogen atoms adsorbed in the  $\beta_2$  state in chapter 4 of this thesis. No CO desorption occurs  $< 350$  K once this state emerges.

The decrease in the amount of CO that can co-adsorb with increasing pre-adsorbed hydrogen coverage is shown in fig. 5.4 (c). The sticking coefficient was determined using eq. 5.1. The results, provided in fig. 5.4 (d), reveal distinct stages in the CO adsorption process. During the initial CO dosing, a plateau is present in all CO signals for the first few L of CO. The CO adsorbs with the same sticking probability irrespective of the H pre-coverage at the start of the dosing sequence. The initial plateau in the sticking coefficient can be understood from a mobile precursor state<sup>[184]</sup>. When

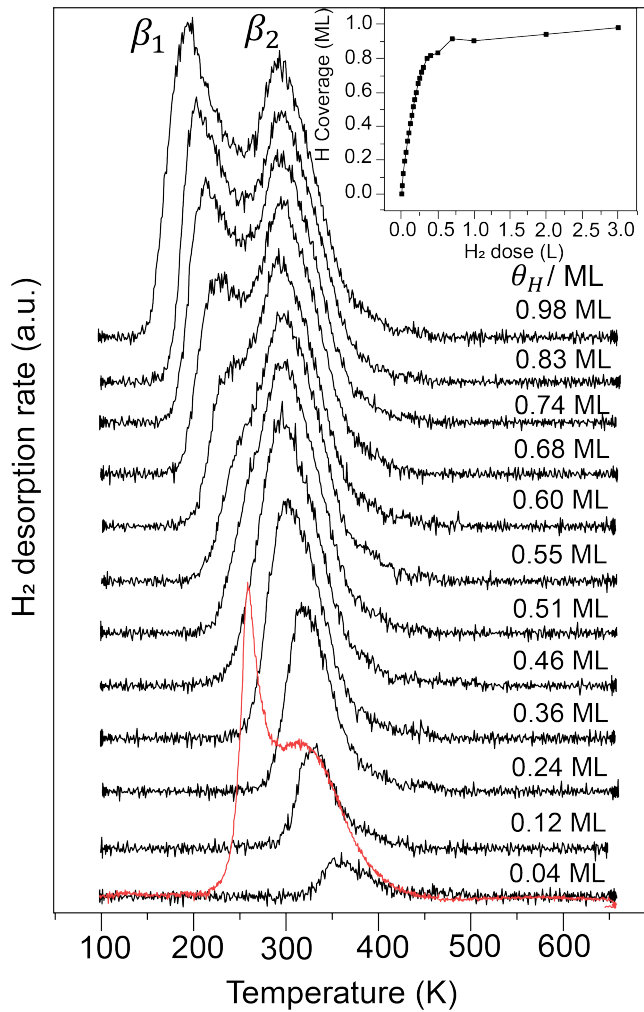


Figure 5.3: A selection of hydrogen TPD spectra obtained by heating the hydrogen covered Co(11 $\bar{2}$ 9) at 2 Ks<sup>-1</sup>. The red desorption spectrum is obtained by heating the Co(0001) surface covered with 1 ML hydrogen at 2 Ks<sup>-1</sup> and is shown here for comparison. The inset shows the growth of hydrogen coverage with increasing hydrogen dose

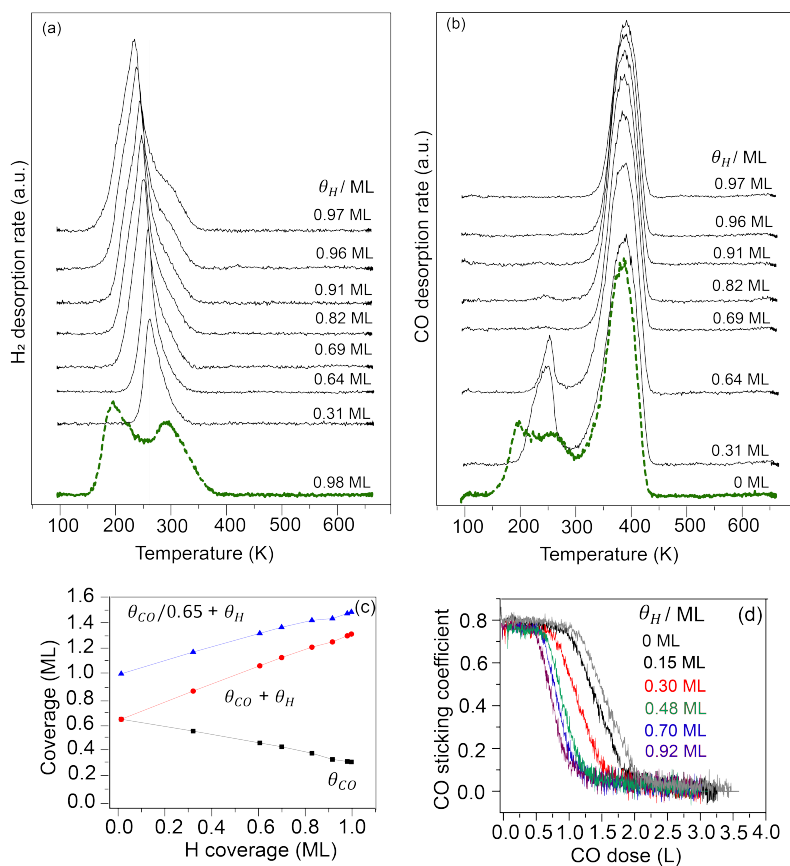


Figure 5.4: Selection of TPD spectra of H<sub>2</sub> (a) and CO (b) (2 Ks<sup>-1</sup>) from Co(11 $\bar{2}$ 9) after pre-adsorbing increasing quantities of H<sub>adr</sub>, followed by a saturation dose of CO. (c) Quantification of the  $\theta_H$ - $\theta_{CO}$  correlation from the spectra shown in (a). (d) Sticking coefficient of CO on hydrogen covered Co(11 $\bar{2}$ 9) surface with increasing hydrogen pre-coverage

a CO molecule collides with an occupied adsorption site, it can either rebound into the gas phase, following Langmuir's predictions, or form a weak van der Waals-type bond with the surface. At low temperature, the CO molecules can remain physisorbed on the surface long enough for it to diffuse across the surface. Upon encountering a vacant adsorption site, it chemisorbs onto the surface. This is followed by a decline in the value of the sticking coefficient, which is attributed to adsorbed molecules filling up the surface. The sticking coefficient reaches 0, signifying that the surface is filled up and no additional surface space is available for further CO adsorption. The CO dose required to reach saturation decreases with increasing H pre-coverage. With increasing H pre-coverage, the rate at which the surface gets saturated after CO dose also increases as represented by the slope of the curves.

Our aim is to determine whether the co-adsorption of H and CO on the kinked Co(11 $\bar{2}$ 9) surface can be explained using the segregation model. As discussed in Chapter 4, if CO and H segregate into islands, the sum of  $\theta_H + (\theta_{CO}/0.65)$  in fig. 5.4 (c) is expected to be unity considering that the maximum attainable CO coverage under these conditions is 0.65 ML. This assumption holds only if the adsorption sites are uniformly equivalent across the entire surface. In contrast to the predominantly flat structure of Co(0001), the Co(11 $\bar{2}$ 9) surface exhibits numerous small terraces and step sites. This structural difference allows for a more accommodating arrangement of H and CO on the surface and hence allows higher coverages of H and CO compared to the relatively flat Co(0001) surface. Building on the insights from prior studies<sup>[159]</sup> regarding CO and hydrogen co-adsorption, the formation of a mixed layer requires that the interactions between CO and H in the adlayer are either more attractive or less repulsive compared to CO-CO and H-H interactions. This balance of interactions would be reflected in the desorption spectra of individual species in a co-adsorption system. However, if this condition is not met, the system is likely to segregate into distinct CO and H regions, as observed on the Co(0001) surface. While the desorption spectra alone do not provide a definitive picture of the adlayer structure on the more complex Co(11 $\bar{2}$ 9) surface, a co-adsorption model can still be proposed.

For instance, for a subsaturation pre-dose of H followed by CO exposure, CO tends to adsorb in the hydrogen-free areas. When the surface becomes saturated with hydrogen, CO compresses the hydrogen adlayer into segregated islands into due to repulsive H-CO and attractive CO-CO interactions, leading to a total surface coverage of > 1ML (blue trace in fig. 5.4 (c)). The CO desorption peak for the saturated H dose aligns with that of CO desorbing independently from the Co surface, as hydrogen fully desorbs by 350 K and hence does not influence CO desorption. Additionally, no new peaks appear in the desorption spectra of either CO or H over the entire range of H coverage ( $\theta_H$ ), indicating that a mixed CO-H layer does not form on the Co(11 $\bar{2}$ 9) surface. This segregation, however, does not result in long-range ordered structures, likely due to the small size of the terraces on Co(11 $\bar{2}$ 9), as also evidenced by the absence of ordered patterns in LEED observations.

#### 5.4.4 Dosing H<sub>2</sub> on Co(11 $\bar{2}$ 9) pre-covered with CO

Numerous studies on various metal surfaces have indicated that CO inhibits the dissociative adsorption of H<sub>2</sub> [142–145] on Co(0001). It was also found that steps on the Co surface enhance hydrogen dissociation [52]. This makes it interesting to explore the influence of both CO and steps on the dissociative adsorption of hydrogen on the kinked Co(11 $\bar{2}$ 9) surface. To investigate the impact of CO<sub>ad</sub> on the dissociative adsorption of hydrogen on Co(11 $\bar{2}$ 9) at 110 K, we performed a series of experiments involving the sequential dosing of a specific quantity of CO followed by the introduction of hydrogen. In fig. 5.5 (a) and (b), we present CO and hydrogen TPD spectra, respectively for different CO pre-coverages. For reference, the dotted hydrogen spectrum represents the desorption from the surface with  $\sim 1$  ML H<sub>ad</sub> ( $\theta_{CO} = 0$  ML). The area under each hydrogen desorption spectrum in fig. 5.5 (b) was used to determine the amount of hydrogen that could dissociatively adsorb on a CO-precovered surface, as shown in fig. 5.5 (c).

The amount of hydrogen that could dissociatively adsorb in the presence of the pre-adsorbed CO decreases with increasing  $\theta_{CO}$ . This trend is clearly visible when comparing spectra in fig. 5.5 (c). Only 0.05 ML of hydrogen can fit with 0.65 ML CO on the surface (fig. 5.5 (b)) which is a significant reduction compared to the 0.38 ML of H<sub>ad</sub> adsorbed that can fit alongside 0.645 ML CO when hydrogen is dosed first (see fig. 5.4 (c) for comparison). The results clearly indicate that adsorbed CO exerts a significant influence on dissociative hydrogen adsorption. More specifically, the maximum coverage ( $\theta_{CO} + \theta_H = 1.12$  ML) reached on a surface pre-covered with CO is lower than when hydrogen is dosed first (1.5 ML), compare fig. 5.4 (c) and 5.5 (c). On carefully analyzing the desorption spectra from the co-adsorbed system we find that in the coverage regime of  $0 < \theta_{CO} < 0.27$ , the  $\beta_1$  peak not only decreases in intensity, but it also shifts towards higher temperatures with decreasing  $\theta_H$  and increasing  $\theta_{CO}$ . However, the  $\beta_2$  feature remains unchanged within this coverage range, indicating that hydrogen desorption from this state is relatively unaffected. In the range of  $0.27 < \theta_{CO} < 0.645$ , the  $\beta_2$  feature experiences a decrease in intensity, but no shift in peak maximum occurs with increasing co-adsorbed  $\theta_{CO}$ , similar to the results for the clean surface ( $\theta_{CO} = 0$  ML). There are no changes in the CO desorption spectra obtained while heating the co-adsorption system when compared to the pure CO/Co(11 $\bar{2}$ 9) system (fig. 5.2).

In the previous section it was postulated that hydrogen and CO form segregated islands on the kinked Co(11 $\bar{2}$ 9) surface. For the dataset where H<sub>2</sub> was dosed after CO, it can be seen in fig. 5.5 (c) that the combined fraction of the surface covered with CO and H ad-islands is  $\leq$  unity. This can be rationalized by a co-adsorption model where CO occupies its favourable sites on the kinked surface and hydrogen adsorbs in the CO-free areas. The similarity between the CO and hydrogen desorption spectra from a co-adsorption system to the pure CO and H spectra, respectively suggests the absence of a mixed H-CO layer.

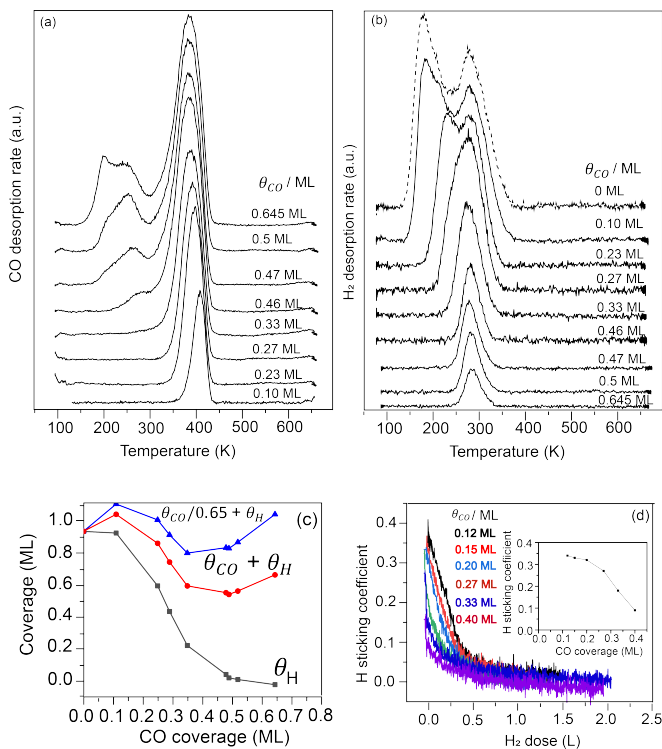


Figure 5.5: Selection of TPD spectra of CO (a) and H<sub>2</sub> (b) (2 Ks<sup>-1</sup>) from Co(11 $\bar{2}$ 9) after pre-adsorbing increasing quantities of CO<sub>ad</sub>, followed by a saturation dose of hydrogen. (c) Quantification of the  $\theta_H - \theta_{CO}$  correlation from the spectra shown in (a) and (b). (d) Sticking coefficient of hydrogen on CO covered Co(11 $\bar{2}$ 9) surface with increasing CO pre-coverage

To gain a deeper insight into the impact of CO on the dissociative adsorption of hydrogen, we conducted a more detailed study of the hydrogen sticking coefficient in the presence of CO. As the surface coverage of CO increases, a reduction in the overall sticking coefficient of hydrogen is observed, as depicted in the inset of fig. 5.5 (d). The data points in the inset are the average of the first few points of all the traces. Importantly, the slopes of the curves, which represent the rate of surface saturation, remains constant. This can be explained by the preference of CO to adsorb on the terraces slightly before the steps rather than selectively poisoning step sites first. As the CO coverage increases H adsorption is rather effectively blocked. The steps may be still available up to a high coverage, but they are certainly less effective at letting H onto the surface.

The dissociative hydrogen adsorption can be explained by the Langmuir dissociative adsorption model where every gas phase molecule that impinges upon the surface becomes chemisorbed when it encounters two adjacent empty surface sites. To illustrate, if we symbolize an empty site as "o" and a site filled with adsorbate as "x," the molecule will solely adsorb when it discovers a landing position of "oo" (signifying two unoccupied nearest neighbor sites). In contrast, the molecule will be repelled when landing on "ox" or "xx." At the beginning of the co-adsorption experiment in the absence of pre-adsorbed CO or low CO coverages, the two empty adjacent sites can be found on the terraces. As the CO coverage increases on the terraces of the kinked surface, the probability of two vacant sites occurring adjacent to one another on the terraces decreases proportionally to the square of the CO coverage. However, the trend in the inset of the fig. 5.5 (d) does not show an inverse quadratic dependence of the sticking coefficient on the CO coverage. This suggests the presence of other favorable reaction paths like the one through the steps that can act as a catalyst for H<sub>2</sub> dissociation and hence maintain high sticking coefficient during the experiment.

Weststrate et al.<sup>[43]</sup> observed that, in the case of sputter-damaged Co(0001) and Co nano-islands, defect sites adjacent to extended close-packed terraces act as efficient catalysts for H<sub>2</sub> dissociation. The dissociation products, H<sub>ad</sub>, binds more strongly on the edge of the defect sites than on the defect sites themselves. Given the high mobility of adsorbed hydrogen atoms on a metal surface, the energetically most favorable site occupation prevails at practical temperatures. Consequently, the heightened stability of H<sub>ad</sub> on terrace sites induces its diffusion away from the defects, the primary active sites for H<sub>2</sub> dissociation. This effective displacement of H<sub>ad</sub> prevents the poisoning of active sites, allowing H<sub>2</sub> dissociation to persist even at elevated total adsorbate coverages. The observed reduction in the sticking coefficient of hydrogen on the surface with increasing CO coverage, as depicted in fig. 5.5, can be predominantly attributed to CO obstructing adsorption sites, inducing modifications in the electronic structure of the surface that alter the barrier for hydrogen dissociation, or a combination of both factors. As described in chapter 3, the CO molecules do not have a strong preference to adsorb on the uncoordinated sites

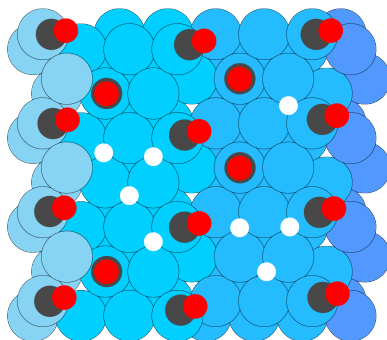


Figure 5.6: A cartoon depicting how CO and hydrogen can co-adsorb in high quantities on the kinked Co(11 $\bar{2}$ 9) surface. This is purely based on hypothesis which can not be confirmed due to the absence of ordered structures of CO and hydrogen alone and co-adsorbed system in LEED. The carbon atoms are represented in gray, oxygen in red and hydrogen in white. Different layers of Co atoms are shown in different shades of blue, lightest shade being the topmost layer of Co atoms

over adsorption on the terrace sites. Hence, the defect sites can remain available for further dissociative adsorption of hydrogen. Nevertheless, the results obtained are inconclusive, necessitating further investigations to comprehensively explore the impact of pre-adsorbed CO on the sticking coefficient of H<sub>2</sub>.

### 5.4.5 Discussion

It is interesting to compare the co-adsorption of CO and H on the kinked surface with the flat Co(0001) (as described in chapter 4 of this thesis). A comparison of CO and hydrogen co-adsorption between Co(0001) and Co(11 $\bar{2}$ 9) has been conducted, for the two exposure sequences: (a) hydrogen followed by CO and (b) CO followed by hydrogen, as summarized in fig. 5.7. A closer analysis of the comparison presented in fig 5.7 (a) reveals that CO adsorption capacity on the Co(0001) surface diminishes more rapidly in the presence of H<sub>ad</sub> when contrasted with the kinked Co(11 $\bar{2}$ 9) surface. This phenomenon can be attributed to the presence of undercoordinated atoms, which potentially provide sites for CO adsorption in a tilted position, particularly at the step sites. This implies that a significant amount of CO can be co-adsorbed alongside hydrogen, thereby achieving a higher total coverage on the kinked surface. This is a hypothesis based on the high coverages of co-adsorbed CO and hydrogen that can be achieved on the Co(11 $\bar{2}$ 9) also depicted in the cartoon in fig. 5.6.

Upon examining fig. 5.7 (b), it becomes evident that dosing CO followed by hydrogen results in a similar total final coverage on both Co(0001) and Co(11 $\bar{2}$ 9). Furthermore, we observe that the rate of decrease in H<sub>ad</sub> alongside CO when hydrogen is dosed following CO, is comparable on both the flat and kinked Co surfaces. Study by Weststrate et al.<sup>[43]</sup> have previously established that during adsorption, hydrogen

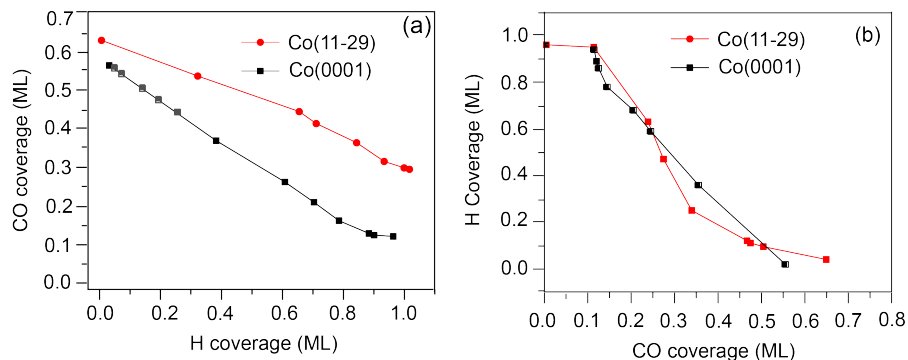


Figure 5.7: Comparison between CO and hydrogen co-adsorption on both Co(0001) and Co(11 $\bar{2}$ 9), examining two exposure sequences: (a) hydrogen followed by CO and (b) CO followed by hydrogen. In both cases, hydrogen was dosed in the presence of the tungsten filament on Co(0001) to enable comparison of co-adsorption behavior with similar hydrogen coverages

initially utilizes the step sites for dissociative adsorption and subsequently diffuses to the terrace of the surface. Furthermore, as previously established in Chapter 4 of this thesis, CO exhibits no clear preference for either step or terrace sites for adsorption. This characteristic implies that CO can freely diffuse to both types of sites since it adsorbs with almost an equal adsorption energy on step and terrace sites. Consequently, on the Co(11 $\bar{2}$ 9) surface, the step sites can remain unoccupied until the maximum surface coverage is reached. As a result, these step sites not only facilitate hydrogen adsorption but also remain available for additional CO adsorption.

### 5.4.6 Summary and conclusions

We investigated the influence of surface structure on the co-adsorption of hydrogen and CO. For pure hydrogen, our study demonstrates a significant enhancement in the dissociative adsorption of H<sub>2</sub> on Co(11 $\bar{2}$ 9) compared to the flat Co(0001) surface, attributed to the barrierless route for dissociative adsorption provided by the kinks on the surface. For CO, we found that a higher saturation coverage of CO can be achieved on the kinked Co(11 $\bar{2}$ 9) surface (0.65 ML) compared to the flat Co(0001) surface ( $\sim$ 0.58 ML) at 110 K. At low-pressure saturation coverage ( $\theta_{CO} = 0.645$  ML), the IR spectrum exhibits characteristic peaks indicating the occupancy of top sites (2100 cm<sup>-1</sup> and 2075 cm<sup>-1</sup>), twofold bridge sites (1930 cm<sup>-1</sup>), and hollow sites (1860 cm<sup>-1</sup>). Notably, no discernible LEED patterns were observed during CO adsorption on Co(11 $\bar{2}$ 9) at 100 K, indicating the absence of long-range ordered structures.

Additionally, this chapter explores the non-reactive co-adsorption of CO and hydrogen on the Co(11 $\bar{2}$ 9) surface, comparing it to the flat Co(0001) surface to highlight the role of step sites on the co-adsorption process. Two adsorption sequences are in-

vestigated: hydrogen followed by CO, and CO followed by hydrogen. In the first sequence, where hydrogen is dosed before CO at 110 K (a temperature where desorption is impossible), our findings reveal a decreasing adsorption capacity for CO as hydrogen coverage increases. Our results suggest that the co-adsorption of CO and hydrogen on the kinked Co(11 $\bar{2}$ 9) surface can be explained by the formation of a segregated layer, as H-H and CO-CO interactions are stronger than H-CO attraction. However, this observation does not fully capture the complexity of CO-H co-adsorption, as the combined saturation coverages of these two adsorbates exceed unity. The exact structures of CO and hydrogen at the terraces and steps remain unclear and require further investigation. This contrasts with the flat Co(0001) surface, where findings align well with the segregation model.

We show that a significant amount of CO can still be adsorbed on the Co(11 $\bar{2}$ 9) surface, even when it is saturated with  $H_{ad}$ . In contrast, a surface saturated with  $CO_{ad}$  exhibits minimal hydrogen adsorption. This inhibition of hydrogen adsorption by CO can be attributed to CO occupying step sites or obstructing these sites due to the presence of neighboring CO molecules, as hydrogen dissociation primarily occurs at step sites. CO can adsorb on both terrace and step sites without a clear preference, so adsorbate coverage at the steps follows the trend of overall CO coverage. Thus, steps remain available for hydrogen dissociation up to high CO coverages but the adsorption of hydrogen atoms depends on the available hollow sites on the surface. In the context of Fischer-Tropsch Synthesis (FTS) catalysis, we propose that steps on the kinked surface can remain unoccupied and serve as primary sites for dissociative  $H_2$  adsorption as long as the surface is not fully saturated. This feasibility arises from CO's slightly higher preference for adsorbing on terrace sites rather than step sites, thereby avoiding the poisoning of step sites and allowing them to facilitate dissociative hydrogen adsorption.

## 5.5 Abbreviations

1. EELS            Electron Energy Loss Spectroscopy
2. FTS            Fischer-Tropsch Synthesis
3. IR             Infrared
4. L              Lagmuir
5. LEED          Low energy electron diffraction
6. ML            Monolayer
7. QMS          Quadrpole mass spectrometer
8.  $P_o$           Initial pressure in the chamber before the introduction of CO
9.  $P_f$           Pressure after surface saturation
10. TPD          Temperature Desorption Spectroscopy
11. UHV          Ultrahigh Vacuum
12.  $\theta_{CO}$         CO coverage (ML)
13.  $\theta_H$           H coverage (ML)
14. "o"          empty site
15. "x"          occupied site

## Chapter 6

# CO dissociation

### 6.1 Abstract

This study systematically explores the reactivity of a stepped cobalt surface in comparison to a kinked cobalt surface for CO dissociation which is an important elementary step in the mechanism of Fischer-Tropsch synthesis. The dissociation reaction of CO was studied on the two Co surfaces between room temperature and 500 K, at pressure of  $\times 10^{-5}$  mbar. The surface concentrations were monitored mainly by the variation of the work function during the experiment, while the reactant (CO) and product (atomic O and C) composition was determined using AES and XPS. Experiments show that CO dissociation can occur on defect sites at around 390 K and leads to a surface covered by both atomic O and C. The product concentrations reach 90% of the total step/kink site concentration of the surface. The dissociation kinetics were modeled using the coverage of CO molecules adsorbed in equilibrium with the gas and by the availability of active sites for the dissociation of adsorbed mobile CO molecules. Fitting the experimental data with a set of rate equations revealed an average CO dissociation barrier of  $112 \text{ kJ mol}^{-1}$  on the stepped Co(10 $\bar{1}$ 9) surface. Both types of active sites on the stepped surface, present in equal concentration, showed similar reactivity for CO dissociation. On the kinked Co(11 $\bar{2}$ 9) surface, the CO dissociation barrier was slightly lower at  $110 \text{ kJ mol}^{-1}$ , indicating a marginally higher activity for CO dissociation compared to the stepped surface. No CO dissociation was experimentally observed on the flat Co(0001) surface. These findings suggest that for Fischer-Tropsch synthesis on Co, CO dissociation can occur readily at low temperatures (390 K) provided the appropriate sites are available, demonstrating that direct C–O bond scission is not difficult under these conditions.

## 6.2 Introduction

One of the critical steps in the FT process is the dissociation of CO as a prelude to the formation of monomer (CH<sub>x</sub>) groups and subsequent chain growth via the coupling of these monomers<sup>[25,185-187]</sup>. Both theoretical and experimental investigations of CO dissociation have been reported extensively in the literature<sup>[23,63,77,136,188-193]</sup> on a variety of transition metal surfaces. Recent efforts have focused more on Co instead of the traditional Fe because of its superior activity, its higher chain growth probability, and its lower water gas shift activity<sup>[194-196]</sup>.

Cobalt catalysts, used in the form of supported nanoparticles during FTS, expose various micro-facets of different orientations containing defects such as steps and kinks<sup>[197]</sup>. These undercoordinated sites play an important role in heterogeneous catalysis. While their concentration is typically much lower than that of flat terraces their reactivity may be substantially higher. The experimental literature contains several elegant examples which show that step sites have a particularly high activity for the dissociation of diatomic molecules such as N<sub>2</sub>, CO, NO and H<sub>2</sub><sup>[43,44,107,192,198,199]</sup>.

The thermodynamically preferred structural arrangement for bulk cobalt, such as a single crystal, is the hexagonal close-packed (hcp) configuration<sup>[32]</sup>. However, for Co crystallites of size 5-10 nm, the face-centered cubic (fcc) structure becomes the thermodynamically favored configuration<sup>[197]</sup>. The distinctly different bulk symmetries exposed on the HCP and FCC Co also lead to the different exposed surface structures. The same 'sites' can be found on real catalysts, where the overall reactivity is determined by the summation of activities of the different sites.

Simulations have revealed that fcc Co nanocrystals with diameters up to 8 nm expose a variety of surface structures which may have different reactivity<sup>[136]</sup>. Within the fcc crystal lattice, two distinct arrangements of five atoms each have been identified to be highly active and energetically preferred for CO dissociation. Specifically, configuration B<sub>5</sub>-A (shown in fig. 6.1) exposes a square and triangular step site geometry<sup>[136]</sup> found for example on the Co(2 1 1)<sup>[200]</sup> or Co(3 1 1) surfaces, while configuration B<sub>5</sub>-B (shown in fig. 6.1) exhibits a step arrangement with 3-fold symmetry found for example on the Co(2 2 1) surface. However, on an fcc single crystal, either one of the B<sub>5</sub>-A or B<sub>5</sub>-B step arrangements is present, whereas both B<sub>5</sub>-A and B<sub>5</sub>-B step arrangements are present on a hexagonal close-packed (hcp) single crystal due to its ABAB stacking of atoms. In addition to the B<sub>5</sub>-A and B<sub>5</sub>-B step arrangements, another type of step arrangement, known as B<sub>6</sub> sites (or kinks), is predicted by Van Helden et al.<sup>[136]</sup> to be present in similar concentrations to both types of B<sub>5</sub> sites on fcc and hcp Co nanoparticles. Liu et al.<sup>[91]</sup> recently compared CO dissociation on hcp and fcc Co based on predicted particle morphologies using Wulff constructions. They found that CO dissociation favors a direct route as opposed to H-assisted CO dissociation on hcp Co due to the presence of favorable active sites which are absent on fcc Co. This is attributed to differences in their crystallographic structures and morphology.

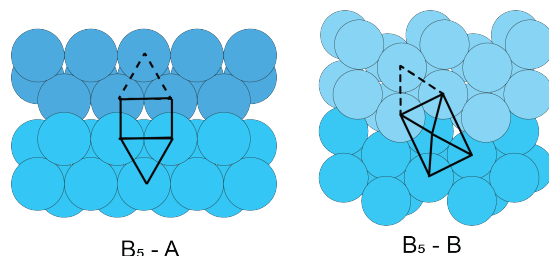


Figure 6.1: Detailed views of the  $B_5$ -A and  $B_5$ -B sites on  $\text{Co}(10\bar{1}9)$  and  $\text{Co}(11\bar{2}9)$ , respectively.

Previous investigations using scanning tunneling microscopy (STM) on  $\text{Ru}(1,1,10)$  and  $\text{Ru}(001)$  surfaces have shown that  $B_5$ -B sites<sup>[66,201]</sup> exhibit lower reactivity for CO dissociation compared to  $B_5$ -A sites<sup>[107]</sup>. Density Functional Theory (DFT) calculations indicate that the activation barriers for direct CO dissociation are in the range of  $116$ - $129$   $\text{kJ mol}^{-1}$  for hcp stepped Co surfaces ( $\text{Co}(10\bar{1}1)$ ,  $\text{Co}(10\bar{1}0)$  and  $\text{Co}(10\bar{1}2)$ ) and  $103$ - $134$   $\text{kJ mol}^{-1}$  for hcp kinked Co surfaces<sup>[91,119]</sup>, ( $\text{Co}(11\bar{2}0)$  and  $\text{Co}(11\bar{2}1)$ ), compared to  $237$   $\text{kJ mol}^{-1}$  on the hcp close-packed  $\text{Co}(0001)$  surface<sup>[202]</sup>.

Zijlstra et al.<sup>[202]</sup> investigated how the activation barrier for direct CO dissociation depends on CO coverage for step-edge and terrace Co sites. They found that at low CO coverage, the CO activation barrier was  $151$   $\text{kJ mol}^{-1}$  on the stepped  $\text{Co}(1\bar{1}05)$  surface<sup>[202]</sup> and  $100$   $\text{kJ mol}^{-1}$  on the kinked  $\text{Co}(11\bar{2}1)$  surface. At higher coverage, the variation of the activation barriers was within  $14$   $\text{kJ/mol}$  and remained below  $100$   $\text{kJ/mol}$  on the kinked surface. The  $B_5$ -B step-edge geometry which is found to be less active for CO dissociation was held responsible for the high CO activation barrier on the stepped surface. They concluded that the CO dissociation barrier for the kinked sites on the kinked surfaces does not change appreciably with CO coverage. Another study found that the activation barrier for CO at a kink site on the hcp  $\text{Co}(11\bar{2}4)$  is lower than at the step or terrace sites, indicating that kink sites may also exhibit enhanced activity for CO dissociation on Co particles<sup>[160]</sup>.

Experimental investigations conducted on a stepped Ru surface, which exposes both types of step sites, showed a preference for CO dissociation to occur primarily at  $B_5$ -A sites<sup>[116]</sup>. Complementing theoretical studies show that the Ru surfaces exhibit lower barriers  $65$   $\text{kJ mol}^{-1}$  for CO dissociation<sup>[47,203]</sup> at  $B_5$ -A stepped sites on the kinked  $\text{Ru}(11\bar{2}1)$  surface. In contrast, Filot et al.<sup>[204]</sup> observed a comparatively higher barrier of  $173$   $\text{kJ mol}^{-1}$  for direct CO dissociation on the  $B_5$ -A stepped sites of  $\text{Rh}(211)$ .

This chapter focuses on studying the reactivity of steps and kinks via direct CO dissociation on hcp-Co single crystals. We explore the reactivity of undercoordinated sites by using a vicinal cobalt single crystal that exposes a high density of monoatomic steps. We use two hcp-Co surfaces - stepped  $\text{Co}(10\bar{1}9)$  and kinked  $\text{Co}(11\bar{2}9)$  to compare the reactivity of steps and kinks for CO dissociation. The step

site concentration on the kinked Co(11 $\bar{2}$ 9) surface is 50% higher than the stepped Co(10 $\bar{1}$ 9) surface. We compare the reactivity of these two surfaces in the low CO pressure regime by determining the barrier for CO dissociation through kinetic analysis. Our findings reveal that the stepped surface exhibits a higher CO dissociation barrier of 113 kJ mol<sup>-1</sup> to that of the kinked Co(11 $\bar{2}$ 9) surface which exhibits a CO dissociation barrier of 110 kJ mol<sup>-1</sup>. The kinked surface demonstrates a higher concentration of atomic C and O post-CO dissociation owing to its higher defect site concentration compared to the stepped Co(10 $\bar{1}$ 9) surface.

### 6.3 Experimental

CO dissociation was explored on the stepped Co(10 $\bar{1}$ 9) surface and a kinked Co(11 $\bar{2}$ 9) surfaces, ball models of which are shown in fig. 6.2. The surfaces of Co(10 $\bar{1}$ 9) and Co(11 $\bar{2}$ 9) are vicinal, exposing monoatomic steps within a close-packed terrace. The distinction between the two lies not only in the width of the terrace but also in the structural characteristics at the steps, as elaborated in section 3.5 of this thesis.

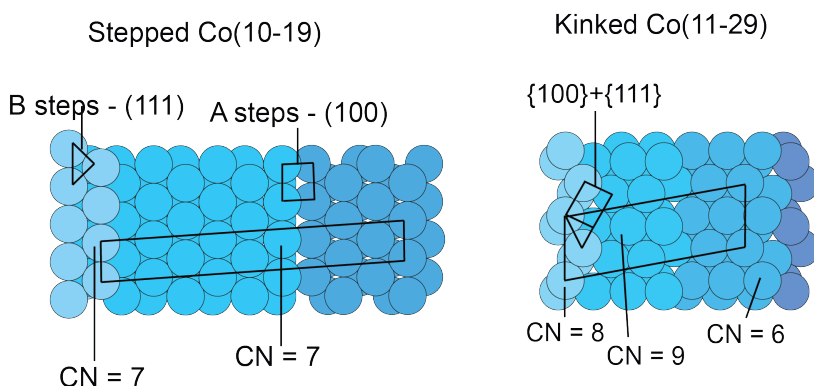


Figure 6.2: Ball models of the stepped Co(10 $\bar{1}$ 9) and kinked Co(11 $\bar{2}$ 9) surfaces illustrate the unit cell and exposed undercoordinated sites. The Co(10 $\bar{1}$ 9) surface has 2 step atoms among 9 Co atoms in the unit cell, resulting in a defect site concentration of approximately 22%. In contrast, the Co(11 $\bar{2}$ 9) surface exposes 4 defect atoms among 10 Co atoms, yielding a defect site concentration of 40%. Co atoms beneath other Co atoms are not included in the count of exposed atoms. Here, CN refers to the coordination number of the atoms

The experiments were performed in a home-built UHV chamber, extensively described in previous chapters. In brief, the chamber is equipped with a sputter-gun for sample cleaning, LEED/Auger optics to measure the chemical composition of the surface, a mass spectrometer, and a Kelvin probe for work-function measurements. CO gas was obtained from Merck (research purity of 99.99%). The gas was further purified by allowing it to flow through a liquid nitrogen trap to remove water and residual carbonyls. Post reaction analysis with Auger spectroscopy revealed no de-

tectable contamination of CO gas, eg., Ni from Ni(CO)<sub>4</sub>, under the chosen reaction conditions.

Temperature-programmed work function (TP-WF) measurements, conducted with a Kelvin probe and normalized with respect to the clean surface, were carried out at a heating rate ( $\beta$ ) of 2 Ks<sup>-1</sup>. The work function values were normalized by subtracting the clean surface value. The normalized work function ( $\Delta\phi$ ) was found to be directly proportional to the surface coverage of atomic oxygen (O<sub>ad</sub>), thus offering direct insights into O<sub>ad</sub> surface concentration<sup>[205]</sup>.

Matline beamline at ASTRID2 (Aarhus, Denmark) was used to obtain medium resolution photoemission spectra on the Co(10 $\bar{1}$ 9) and Co(11 $\bar{2}$ 9) surfaces. All the photoemission experiments were carried out at normal emission. C1s and O1s core level spectra were measured using a photon energy of 380 eV and 650 eV, respectively. Binding energies are reported with respect to the Fermi edge, which was measured after every change of the photon energy. For the XPS measurements, the samples were clamped onto a Ta flat plate by thin tantalum wires spotwelded to the sample plate. Since the thermocouple is not in direct contact with the sample, the temperature reading is less representative than the data obtained in the home laboratory. Sample cleanliness was confirmed by photoemission experiments.

The ( $\sqrt{3}\times\sqrt{3}$ )R30° - CO structure (1/3 ML,<sup>[98]</sup>) prepared by heating the CO saturated Co(0001) surface to 330 K, was used as the reference for quantification of the C1s and O1s signal intensities and deconvoluting the C1s and the O1s spectra obtained on the high-index Co(11 $\bar{2}$ 9) and Co(10 $\bar{1}$ 9) surfaces. To quantify the contribution of atomic C (evidenced by peaks distinct from those attributed to CO<sub>ad</sub>), the area under the peaks originating from CO<sub>ad</sub> was subtracted from the total spectral area, leaving only C peaks. Quantification of  $\theta_O$  and  $\theta_C$  using Auger at the home laboratory is discussed in the next section of this chapter along with the detailed description of CO dissociation experiment. This is done with the assumption that the dissociation experiments at both Matline and home laboratory are performed under similar conditions.

## 6.4 Results

We looked for direct experimental evidence of CO dissociation on the kinks of a kinked Co(11 $\bar{2}$ 9) single crystal surface as a function of the crystal temperature. To achieve this, we could follow the increase in the concentration of either atomic C or atomic O since CO dissociation results in equal amounts of C and O. Fig. 6.3 (a) and (b) show the C1s core level spectra obtained at various stages of a CO dissociation experiment conducted on the kinked Co(11 $\bar{2}$ 9) surface. As the first step of the experiment, we recorded the C1s spectra at 350 K under vacuum. This spectra (see fig. 6.3 (a)) was recorded on the surface that had just undergone a CO adsorption-desorption cycle and hence not on a freshly cleaned Co(11 $\bar{2}$ 9) surface. No discernible peak at 283

eV was observed, indicating the absence of atomic C. Subsequently, the surface was subjected to a CO pressure of  $1 \times 10^{-5}$  mbar at 350 K, followed by recording another C1s spectrum after closing the CO valve. Closing the CO valve leads to a lower CO partial pressure which disrupts the adsorption-desorption equilibrium, leaving 0.32 ML CO on the surface. The amount of CO adsorbed at 350 K during a CO adsorption - desorption experiment can be found in fig. 3.7. Analysis of the recorded spectra revealed a distinctive peak at 285.5 eV, attributed to CO adsorbed ( $\text{CO}_{ad}$ ) on the top sites in agreement with the previous literature<sup>[52]</sup>. No traces of atomic C were detected, indicating the absence of CO dissociation at 350 K. This experimental procedure was subsequently repeated at elevated surface temperatures until evidence of CO dissociation, characterized by the presence of  $\text{C}_{ad}$ , was observed.

A comparison of the C1s spectrum obtained after exposing the kinked  $\text{Co}(11\bar{2}9)$  surface to CO at 350 K (fig. 6.3 (a)) and 390 K (fig. 6.3 (b)) showed that a new peak has developed after exposing the surface to CO at 390 K, at a binding energy of 283 eV, assigned to atomic C<sup>[206]</sup>. The presence of atomic C on the kinked surface after CO exposure serves as a definitive marker for CO dissociation. Thus, the temperature at which CO starts dissociating on the kinked  $\text{Co}(11\bar{2}9)$  surface is identified as  $\sim 390$  K. To ensure that the C1s spectra were not influenced by the co-adsorbed CO, we increased the surface temperature to 420 K, the temperature at which all CO desorbs from the surface. The intensity of the 283 eV peak increased with each subsequent exposure cycle at 420 K, stabilizing after a total dosing time of approximately 17 minutes. Once no further changes in the intensity of the 283 eV peak were observed, with the sample temperature or the duration of CO exposure (data not shown in this chapter), the dissociation cycles were stopped. The C1s spectra consistently exhibited a peak at a binding energy indicative of 283 eV which is characteristic of "carbide" carbon. No "graphitic" carbon (BE  $\sim 284.4$  eV) was found on the surface, even at higher temperatures i.e.  $>550$  K.

After reaching the point where no more CO could be dissociated on the kinked  $\text{Co}(11\bar{2}9)$  surface, the sample was heated to 670 K (at  $1 \text{ K s}^{-1}$ ) while simultaneously recording the O1s and C1s spectra as shown in the fig. 6.4 (a) and 6.4 (b), respectively. The O1s and C1s spectra were used to quantify  $\theta_O$  and  $\theta_C$  (the respective coverages of oxygen and carbon). The plot in fig. 6.4 (c) represents  $\theta_O$  and  $\theta_C$  against temperature, showing no significant changes in  $\theta_O$  and  $\theta_C$  until 525 K.

Upon reaching 525 K, the surface coverages of  $\theta_C$  and  $\theta_O$  exhibit a decline which is attributed to the recombination of atomic C and O species<sup>[207]</sup>. It is interesting to note that at 549 K, the rate of decrease in  $\theta_C$  (0.0027) is higher than that of  $\theta_O$  (0.0013). This discrepancy challenges the expectation that if all deposited C and O resulting from CO dissociation were solely recombining and desorbing from the surface, the rate of decrease in  $\theta_C$  and  $\theta_O$  would be the same. However, the difference in observed rates suggest an additional mechanism at play. Once the surface temperature reaches 590 K, the area under the C1s peak corresponding to  $\theta_C$  goes to zero, while the level of  $\text{O}_{ad}$  stabilizes at 0.15 ML. Therefore, approximately 33% of C recombines

with O and desorbs from the surface. The disappearance of the C1s peak is attributed to the diffusion of atomic carbon into the bulk in addition to the recombination of C and O. A relevant process of practical interest is short-term deactivation of the Co catalyst under FT reaction conditions which can be caused by the residual oxygen as a result of CO dissociation. In their study, Kizilkaya et al.<sup>[205]</sup> determined the barrier for water formation on the defective Co(0001) surface to be  $136 \pm 7 \text{ kJ mol mol}^{-1}$ . The high barrier associated with oxygen removal through water formation implies that this process cannot be immediately classified as a rapid step within the FTS reaction mechanism<sup>[22,41]</sup>. Further exploration of this topic is not the part of this thesis but it is interesting to note that contrary to a range of both theoretical and experimental investigations, CO dissociation may not unequivocally govern the rate-determining step in the FTS process.

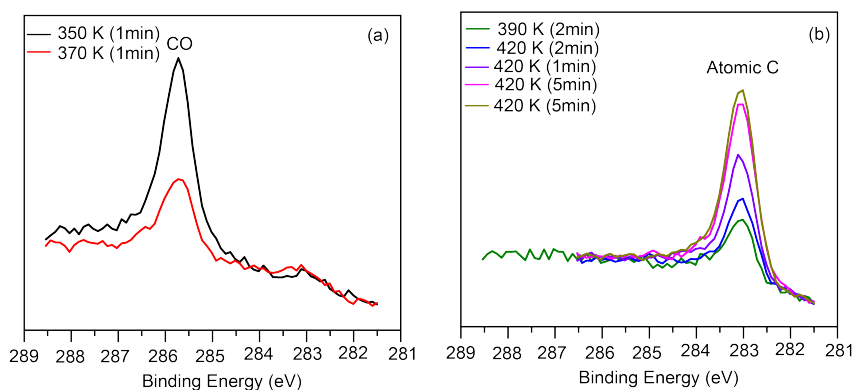


Figure 6.3: C1s spectra recorded at (a)  $< 390 \text{ K}$  and (b)  $\geq 390 \text{ K}$  to determine the temperature at which the CO dissociation begins to occur on the kinked Co(11 $\bar{2}$ 9) surface under  $p_{\text{CO}} = 1 \times 10^{-5} \text{ mbar}$  for a total of 17 minutes

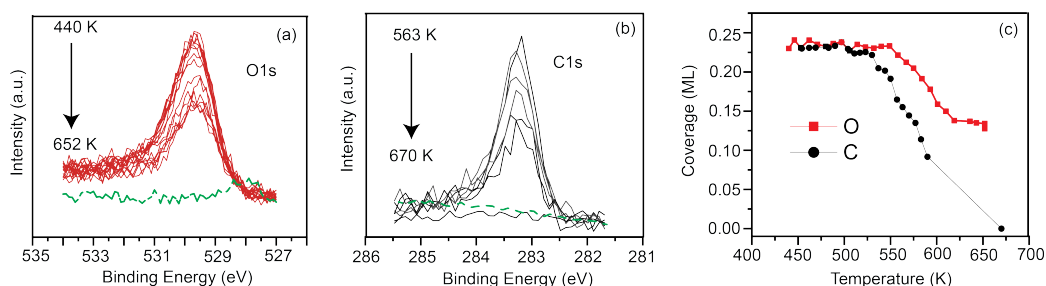


Figure 6.4: (a), (b) O1s and C1s spectra recorded while heating the kinked Co(11 $\bar{2}$ 9) at  $1 \text{ K s}^{-1}$  after the CO dissociation experiment. The O1s and C1s spectra from a clean surface is shown as the green dotted curve in (a) and (b), respectively. (c) Comparison of behavior of O and C coverage with increasing temperature  $> 440 \text{ K}$

XPS data for CO dissociation obtained at the Matline beamline has limitations

in determining the kinetic parameters due to temperature reading uncertainties, as the thermocouple was attached to the sample-plate instead of the directly to the sample. Hence, to compare CO dissociation on the kinked Co(11 $\bar{2}$ 9) and stepped Co(10 $\bar{1}$ 9) surfaces, we performed an isothermal experiment within our home laboratory, leveraging insights obtained from the temperature onset of CO dissociation on these surfaces via the XPS experiments. Throughout the experiment, we recorded work function and Auger spectra for both the Co(10 $\bar{1}$ 9) and Co(11 $\bar{2}$ 9) surfaces, providing crucial data for subsequent in-depth analysis during CO dissociation.

Fig. 6.5(a) provides a reference, illustrating the relative work function (rWF) gain from 0 as the Co(11 $\bar{2}$ 9) surface is exposed to CO pressure of  $1 \times 10^{-8}$  mbar at 100 K, plateauing when saturation is reached and no further CO can be adsorbed. The rise in rWF is attributed to the increased work function caused by the adsorbed CO. Analyzing the work function change ( $\Delta\phi$ ) with increasing CO coverage and comparing it with  $\theta_{CO}$  obtained from other quantitative techniques like TPD, we observed a direct correlation between  $\Delta\phi$  and  $\theta_{CO}$ . This method of determining the correlation between  $\Delta\phi$  and  $\theta_{CO}$  is also demonstrated in literature<sup>[52,98,208]</sup>. Since 1 L corresponds to an exposure of  $1.33 \times 10^{-6}$  mbar per second, fig. 6.5 (a) shows that the surface coverage of CO reaches a stable value after an exposure of approximately 8 L. This corresponds to a rWF value of 1200 meV, attributed to a  $CO_{ad}$  coverage of 0.645 ML, as derived from TPD measurements. CO adsorption induces a positive work function shift of 1800 mV per ML. This conversion factor is used throughout this article whenever work function data is used to determine the coverage of CO.

The CO dissociation experiment started with the determination of the work function of the clean kinked Co(11 $\bar{2}$ 9) surface, for reference. Subsequently, the surface was exposed to brief pulses of CO at  $1 \times 10^{-5}$  mbar and held at a constant temperature until no further change in the work function was observed upon closure of the CO valve. Fig. 6.5 (b) shows the result of such an experiment performed at 430 K. The work function change associated with the first CO pulse is around 600 meV, which is around half of the value for the surface saturated with CO at low temperature (see fig. 6.5 (a)). This shows that the CO coverage during dissociation is substantial, on the order of 0.32 ML. Following the initial CO pulse, the valve was closed, and the sample temperature was maintained at 430 K as CO was pumped out, rapidly decreasing the chamber pressure to  $1 \times 10^{-10}$  mbar. The desorption of residual CO molecules from the surface is marked by a drop of the  $\Delta\phi$  by 450 meV. This behavior is corroborated by XPS experiments, demonstrating complete desorption of CO from the kinked surface above 390 K. The  $\Delta\phi$  stabilizes at 150 meV as a result of the co-adsorbed oxygen. Kizilkaya et al.<sup>[205]</sup> demonstrated that oxygen induces a positive  $\Delta\phi$  as expected from the adsorption of negatively charged (i.e. electron withdrawing) O atoms<sup>[209]</sup>, whereas carbon does not alter the rWF. As the rWF of the co-adsorbed system is a linear combination of the contributions from  $O_{ad}$  and  $CO_{ad}$ <sup>[205,210]</sup>, we determined  $\theta_O$  on both the Co(10 $\bar{1}$ 9) and Co(11 $\bar{2}$ 9) surfaces using the CO uptake curves from the clean Co(10 $\bar{1}$ 9) and Co(11 $\bar{2}$ 9) surfaces. The

subsequent deposition of oxygen following CO dissociation corresponds to a  $O_{ad}$  coverage of 0.08 ML. This sequence defines one cycle of exposure.

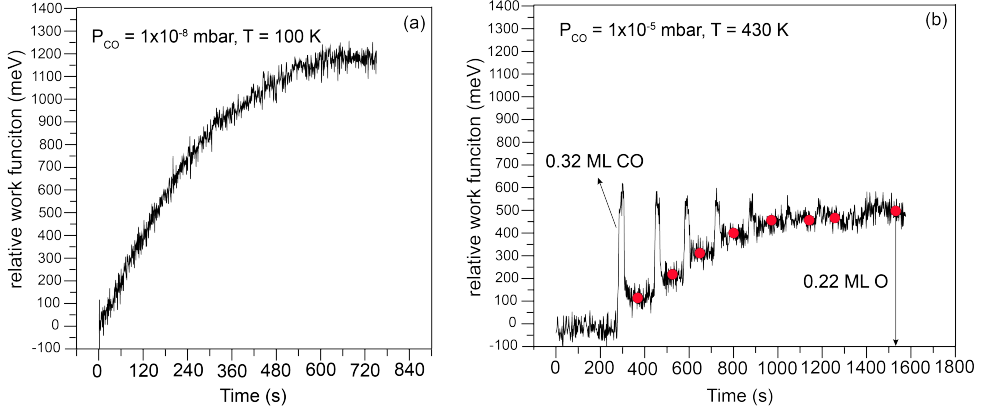


Figure 6.5: (a) Work function measurements following CO adsorption on Co(11 $\bar{2}$ 9) surface at 100 K (for reference), (b) Work function measurements during pulsed CO dosing ( $p = 1 \times 10^{-5}$  mbar) on Co(11 $\bar{2}$ 9) surface at 430 K. The work function during pulse contains contributions from  $CO_{ad}$  and  $O_{ad}$  while the signal between the pulses (represented by red dots) is solely due to  $O_{ad}$

During the next exposure cycle, the introduction of CO induces an increase in the rWF of 425 meV, corresponding to a coverage of 0.22 ML of CO. The diminished  $\Delta\phi$  observed during CO dosing in the second cycle can be attributed to two primary factors: (i) the presence of atomic carbon and oxygen, recognized for diminishing the CO adsorption capacity of the surface<sup>[211]</sup> (geometric site blocking), and (ii) the reduced adsorption energy of CO due to co-adsorbed C and O species, which concurrently results in a lower equilibrium coverage<sup>[212]</sup>. Upon closure of the CO dosing valve, rWF drops to 200 meV, correlating with  $\theta_O = 0.1$  ML. These cycles were repeated until no additional increase in work function was observed during exposure. This experiment phase is denoted as a kinetic run. After each exposure cycle, an Auger electron spectrum (AES) under vacuum was recorded and the approximate coverage of atomic C and O on the surface was determined. The coverage of carbon ( $\theta_C$ ), for eg. on the surface is determined by:

$$\theta_C = \frac{I_C}{\frac{I_{Co(11\bar{2}9)}}{I_{C_{ref}}}} \quad (6.1)$$

Where  $I_C$  and  $I_{C_{ref}}$  represent the peak-to-peak intensity, i.e., the difference between positive and negative peaks of the differentiated spectrum of carbon (C) on the Co(11 $\bar{2}$ 9) surface and the reference spectra. The reference spectra were generated on Co(0001) utilizing a previously established method<sup>[212]</sup>, involving exposure of

warm (630 K) Co(0001) to ethylene. At this higher surface temperature, ethylene undergoes complete decomposition upon adsorption, resulting in the formation of 0.5 ML of atomic carbon on the surface. In our current study, this well-defined reference state is employed to calculate surface C coverages, thereby minimizing uncertainties associated with sensitivity factors. Fig. 6.6 presents a comparison of the Auger spectra obtained on the Co(11 $\bar{2}$ 9) surface post-CO dissociation experiment with the reference spectra obtained on Co(0001).

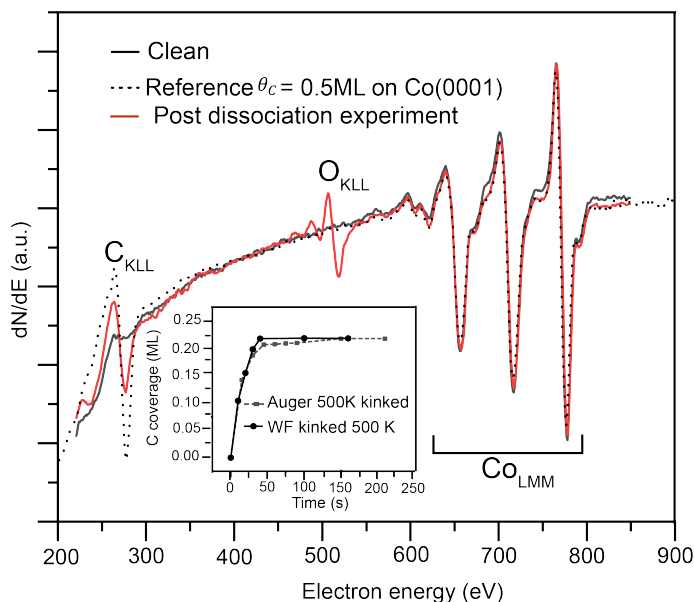


Figure 6.6: Comparison of Auger spectra from clean Co(11 $\bar{2}$ 9) (solid black line) and Co(11 $\bar{2}$ 9) after CO dissociation experiment at 430K (red line), Auger spectra of  $\theta_C = 0.5$  ML obtained on the flat Co(0001) (dotted black line) is added for reference and quantification of  $\theta_C$ . The inset shows the comparison of the  $\theta_C$  obtained using Auger and  $\theta_O$  obtained using WF

The surface coverages obtained from Auger spectroscopy were validated by cross-referencing with coverages obtained from the analysis of the work function data (inset of Fig. 6.6). Kinetic runs were carried out using the same procedure for different sample temperatures - 430 K, 450 K, 475 K and 500 K - for a total of 4 complete kinetic runs. The same experiment was also performed on the stepped Co(10 $\bar{1}$ 9) surface.

Fig. 6.7 (a) and (c) show the growth of  $\theta_O$  as a function of exposure time at varying temperatures on both kinked Co(11 $\bar{2}$ 9) and stepped Co(10 $\bar{1}$ 9) surfaces during the CO dissociation experiment. On the Co(11 $\bar{2}$ 9) surface,  $\theta_O$  reaches saturation at 0.21 monolayers (ML), while on the stepped Co(10 $\bar{1}$ 9) surface, it stabilizes at 0.13 ML. The site concentration, e.g. the step edge atom concentration, was estimated from the models shown in the Fig. 6.2. By counting the number of Co atoms on the top layer of the surface with the coordination number  $< 9$ , the concentration of underco-

ordinated atoms present at a step edge can be calculated. In this case, the step atom concentration on the stepped Co(10 $\bar{1}$ 9) and Co(11 $\bar{2}$ 9) surfaces amounts to 22% and 40%, respectively.

Panels (b) and (d) in fig. 6.7 present the equilibrium CO coverage obtained during each exposure cycle  $\theta_O$ , starting from  $\theta_O = 0$  on the kinked Co(11 $\bar{2}$ 9) and stepped Co(10 $\bar{1}$ 9) surfaces, respectively. As explained earlier, the availability of CO for adsorption diminishes with increasing  $\theta_O$ . As expected from the van't Hoff equation - eq. 6.2, the equilibrium constant is inversely proportional to the temperature.

$$\frac{d \ln k}{dt} = \frac{\Delta H^O}{RT^2} \quad (6.2)$$

where  $\ln$  denotes the natural logarithm,  $k$  is the thermodynamic equilibrium constant,  $\Delta H^O$  is enthalpy change, and  $R$  is the ideal gas constant. Hence with increasing temperature less CO can be adsorbed in equilibrium on the surface. It is important to highlight that the temperature range was capped at 525 K due to the recombination of C and O atoms at this threshold, as elucidated in our XPS experiments (Fig. 6.4(c)).

Figure 6.8 presents a comparative analysis of the oxygen growth rates on Co(11 $\bar{2}$ 9) and Co(10 $\bar{1}$ 9) surfaces resulting from CO dissociation at 475 K. To ensure a fair comparison, the data on oxygen growth acquired from the stepped Co(10 $\bar{1}$ 9) surface at 475 K was normalized to match the step concentration of the kinked Co(11 $\bar{2}$ 9) surface in fig. 6.8. The comparison shows that  $\theta_O$  increases faster on the kinked Co(11 $\bar{2}$ 9) surface than the Co(10 $\bar{1}$ 9) surface. This observation suggests that the kinked surface exhibits enhanced activity for CO dissociation relative to the stepped Co surface. In order to quantify this difference in activity, we perform a kinetic analysis by comparing isothermal uptake curves at one of the chosen temperatures.

### 6.4.1 Barrier Estimation

The work function data was used to derive the kinetics of CO dissociation by using the build-up of the oxygen coverage that was determined between the CO pulses. The C coverage is assumed to be the same as the O coverage since both  $O_{ad}$  and  $C_{ad}$  result from CO dissociation. The work function measurements also inform us about the CO equilibrium coverage, which changes from 0.32 ML to 0.04 ML as the dissociation progresses. The global CO coverage on both terraces and step sites is representative of the step site occupation since there is a dynamic equilibrium between CO adsorbed at steps and terraces which have approximately equal adsorption strength, as shown in chapter 3 of this thesis. The kinetic parameters of CO dissociation were evaluated using a microkinetic model, where the rate of C formation via CO dissociation (in ML  $s^{-1}$ ) is defined as:

$$r_{CO_{diss}} = \frac{k_B T}{h} \exp\left(\frac{\Delta G^\#}{RT}\right) \theta_{CO} (X - \theta_C) \quad (6.3)$$

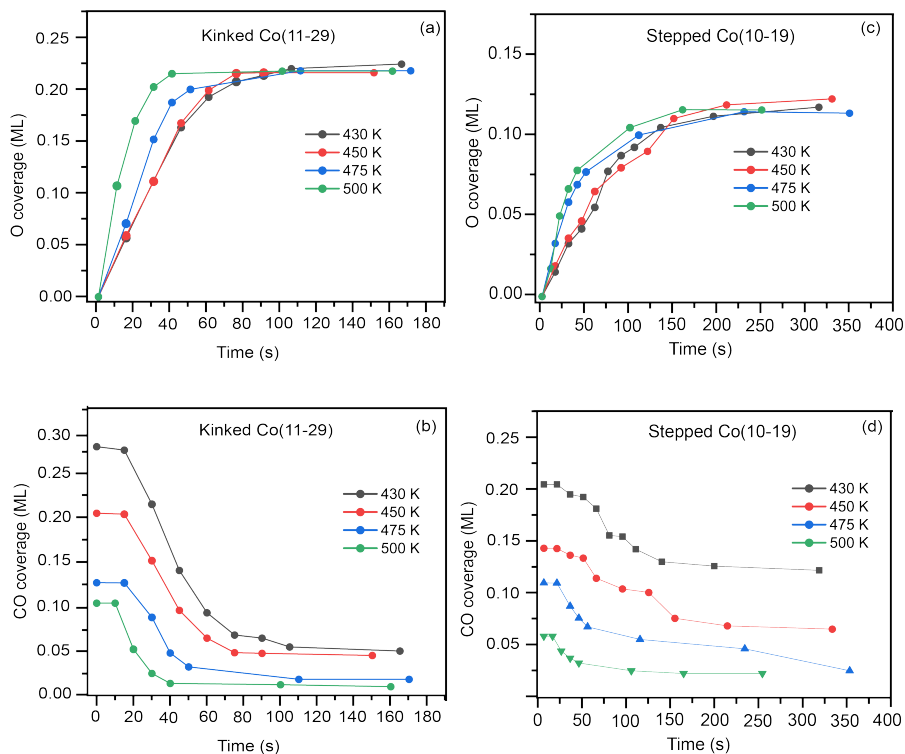


Figure 6.7: (a), (c) Comparison of growth of  $\theta_O$  during pulses of CO at different temperatures – 430 K, 450 K, 475 K and 500 K on kinked Co(11 $\bar{2}9$ ) and stepped Co(10 $\bar{1}9$ ) surfaces, respectively. The  $\theta_O$  is determined using the reference work function measurements. (b) and (d)  $\theta_{CO}$  able to adsorb after each cycle in a kinetic run at the temperatures indicated in the legend on Co(11 $\bar{2}9$ ) and Co(10 $\bar{1}9$ ), respectively

where  $X$  is the concentration of defect sites in ML and the temperature dependent  $\theta_{CO}$  is derived from the work function data used as input. The data points chosen to describe the following kinetic analysis were obtained from the experiment performed at 430 K. We explored these two cases, (i) assuming that  $X=0.2$  ML (22% defects) on the Co(10 $\bar{1}9$ ), of which 90% is ultimately covered by C and O. Fitting of the data yields a free energy of activation,  $\Delta G^\ddagger$  of 112 kJ mol $^{-1}$ . (ii) assuming that  $X=0.4$  ML (40% defects) on the Co(11 $\bar{2}9$ ), of which 90% is ultimately covered by C and O. Fitting of the data yields a free energy of activation,  $\Delta G^\ddagger$  of 110 kJ mol $^{-1}$  gives the best match. The fit for the kinetic run at 430 K is shown in fig. 6.9.

A tabulation of the computed change in the Gibbs free energy ( $\Delta G^\ddagger$ ) for the direct CO dissociation on both the stepped Co(10 $\bar{1}9$ ) and kinked Co(11 $\bar{2}9$ ) surfaces at various temperatures is presented in Table 6.1.

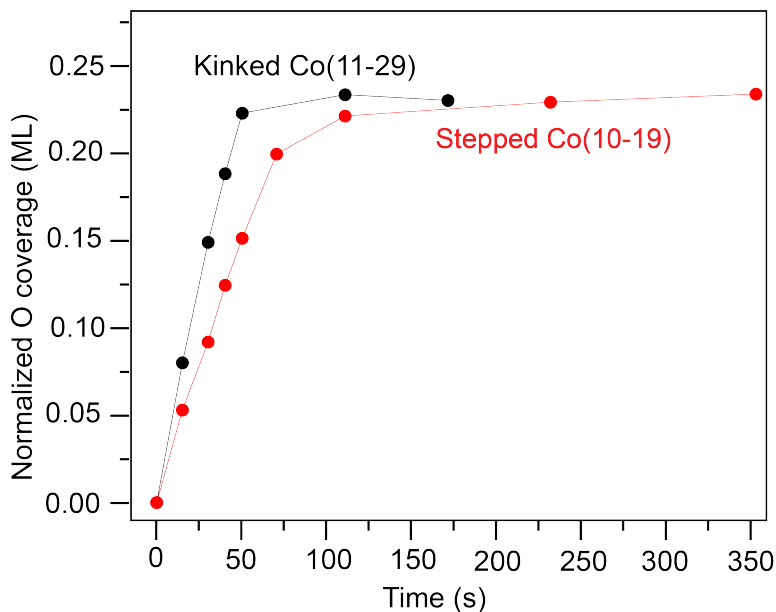


Figure 6.8: A comparison of the normalized rate of  $O_{ad}$  growth due to CO dissociation at 475 K on the stepped  $Co(10\bar{1}9)$  and kinked  $Co(11\bar{2}9)$  surfaces is presented. Normalization eliminates the influence of variations in step site concentration, allowing for a direct comparison of the CO dissociation rates on the two surface types.

## 6.5 Discussion

In this study, we focus on two surfaces, stepped  $Co(10\bar{1}9)$  and kinked  $Co(11\bar{2}9)$ , to compare their activity for direct CO dissociation. As shown in fig. 6.2, the  $Co(10\bar{1}9)$  surface exhibits flat terraces along with 22% steps with equal amounts of both A and B type step edges, while the kinked  $Co(11\bar{2}9)$  surface contains 40% kink sites. Both step and kink sites are known to facilitate CO dissociation at relatively low temperatures (300 - 400 K), as previously also observed on  $Ni(111)$  and stepped  $Ni(977)$  [211,213,214], and  $Ru(0001)$  [107]. Additionally, more open hcp Co surfaces and Co foils have also shown facile CO dissociation [101,215,216]. Theoretical studies on

Table 6.1:  $\Delta G^\ddagger$  for the direct CO dissociation on  $Co(10\bar{1}9)$  and  $Co(11\bar{2}9)$

Temperature (K)	$Co(10\bar{1}9)$ ( $\text{kJ mol}^{-1}$ )	$Co(11\bar{2}9)$ ( $\text{kJ mol}^{-1}$ )
430	112	110
450	111	108
475	110	110
500	103	95

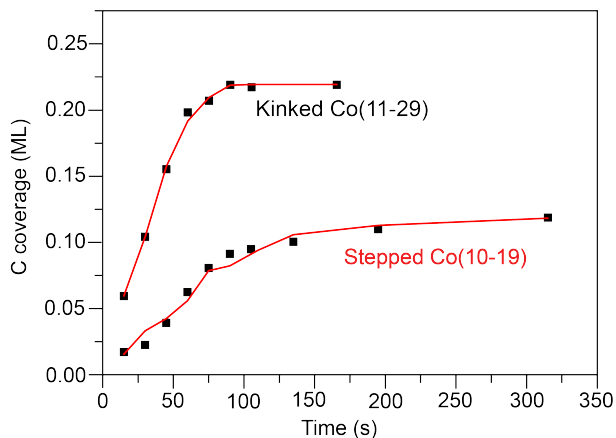


Figure 6.9: The increase of the  $C_{ad}$  coverage after repeated cycle of exposure with respect to the duration of exposure at 430 K. Markers indicate the measured data points whereas the solid line represents the results of a microkinetic simulation used to evaluate the data as discussed

cobalt support these findings, with calculated CO dissociation barriers ranging from 103 to 130  $\text{kJ mol}^{-1}$  on open hcp Co surfaces<sup>[91]</sup>. In the case of fcc Co nanoparticles, such defects constitute a significant proportion of all surface atoms, amounting to about 10% of surface imperfections for particle size which show optimal activity for FTS<sup>[136]</sup>.

Our current study indicates that the accumulation of atomic O and C on both the surfaces, post-CO dissociation, aligns with the total concentration of stepped sites. This observation suggests comparable levels of activity for CO dissociation at both  $B_5$ -A and  $B_5$ -B sites on the stepped surface. If one of these sites were to exhibit activity ten times lower (for example) than the other, a distinctive two-stage pattern in the oxygen uptake curves as presented in fig. 6.10 would be anticipated. This expectation arises from the fact that the more active step site would reach saturation earlier than the less active counterpart. This result is in contrast to the previous investigation where  $B_5$ -B sites<sup>[66,201]</sup> on the catalyst surface exhibit lower reactivity compared to the  $B_5$ -A sites<sup>[200,202]</sup>.

Accurately estimating the activation energy for CO dissociation from the experimental data presented in fig. 6.9 is challenging. The simultaneous CO desorption and CO dissociation processes result into uncertainty in the active site concentration. Another challenge is the influence of neighboring C and O atoms adsorbed near defect sites on CO adsorption on the surfaces with small terraces, such as the kinked Co(11 $\bar{2}$ 9) surface<sup>[210]</sup>. The application of an Arrhenius-type equation, accompanied by an approximated prefactor, gives rise to a different combinations of A (prefactor) and  $E_{act}$  (activation energy) that can fit the experimental dataset equally well. The assumption of a pre-factor of  $1 \times 10^{10} \text{ s}^{-1}$  results in an activation energy of 81  $\text{kJ mol}^{-1}$  while assuming a prefactor of  $1 \times 10^{13} \text{ s}^{-1}$  results in an activation energy

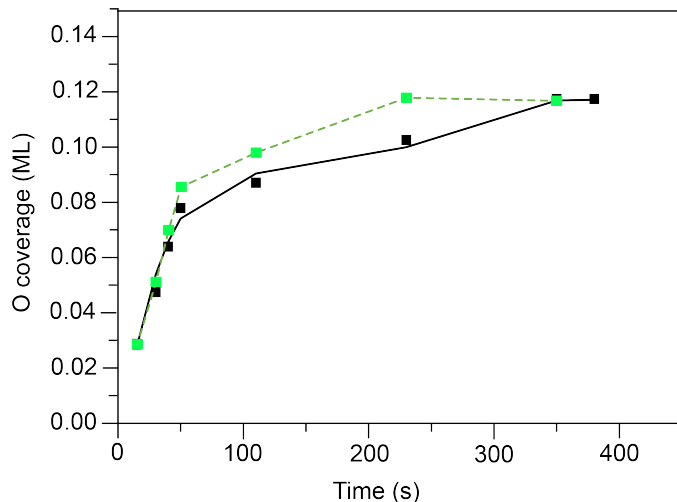


Figure 6.10: Anticipated growth of  $\theta_{\text{O}}$  during pulses of CO at 475 K on the stepped  $\text{Co}(10\bar{1}9)$  surface assuming that one of the  $\text{B}_5\text{-A}$  or  $\text{B}_5\text{-B}$  sites is 10 times more active for CO dissociation than the other. Original data points representing growth of  $\theta_{\text{O}}$  during CO dissociation experiment on the stepped  $\text{Co}(10\bar{1}9)$  at 475 are shown in green

of  $100 \text{ kJ mol}^{-1}$ . To simplify the fitting procedure and reduce the number of variables, an alternative approach using the Eyring equation (eq. 6.3) was employed, as previously applied in the results section. By utilizing this method, only one variable remains, namely the Gibbs free energy of activation. By employing the Eyring equation, the computed activation energy falls within interval of  $95 - 112 \text{ kJ mol}^{-1}$ . Given the inherent uncertainties stemming from the experimental setup and the subsequent data analysis, we present a relatively wide range for the activation energy, spanning from  $80$  to  $110 \text{ kJ mol}^{-1}$ , to encompass the potential spectrum of values.

While the alteration in Gibbs free energy is conventionally influenced by changes in enthalpy, temperature, and system entropy, one would anticipate a decrease in  $\Delta G^\ddagger$  with an increase in the sample temperature. Contrary to this expectation, our current study reveals a marginal dependence of the change in Gibbs free energy of activation on sample temperature. Only at 500 K, we see a significant decrease in the gibbs free energy. This observation suggests a compensatory effect, wherein alterations in independent variables offset the  $\Delta G^\ddagger$ , contributing to its limited dependence on temperature. For instance, the system's enthalpy may rise with increasing temperature, compensating the expected increase in Gibbs free energy of activation.

The analysis of data obtained from the CO dissociation experiment at 430 K reveals a barrier of  $110 \text{ kJ mol}^{-1}$  on the kinked  $\text{Co}(11\bar{2}9)$  surface. In contrast, the determined CO dissociation barrier on the stepped  $\text{Co}(10\bar{1}9)$  surface slightly exceeds this value at  $112 \text{ kJ mol}^{-1}$ . This trend persists across the range of sample temperatures chosen in this study, indicating a slightly more pronounced CO dissociation rate on

the kinked surface compared to the stepped surface. Despite the subtle activity variance between the two surfaces, the difference in the CO dissociation barrier remains modest. Consequently, we conclude that CO dissociation is slightly easier on kinked Co(11 $\bar{2}$ 9) surface as compared to the Co(10 $\bar{1}$ 9) surface. Considering the exponential dependence of the CO dissociation rate on the dissociation barrier, even a slight elevation in the barrier on the stepped surface is sufficient to account for the observed differences in the rate, as depicted in fig. 6.8.

## 6.6 Conclusions

The reactivity of the step and kink sites for CO dissociation was investigated using a well defined stepped Co(10 $\bar{1}$ 9) and kinked Co(11 $\bar{2}$ 9) surfaces with a step density of 22% and 40%, respectively. CO dissociation occurs at step and kink sites at a temperature  $\geq 390$  K. By assuming the pre-exponential factor of  $1 \times 10^{13} \text{ s}^{-1}$ , a slightly lower barrier for this process was estimated on the kinked Co(11 $\bar{2}$ 9) -  $110 \text{ kJmol}^{-1}$  as compared to the stepped Co(10 $\bar{1}$ 9) where the CO activation barrier was found to be  $112 \text{ kJ mol}^{-1}$ . The change in the Gibbs free energy of activation is found to be slightly dependent on the sample temperature during CO dissociation. 0.12 ML and 0.22 ML atomic O produced as a result of CO dissociation on the stepped Co(10 $\bar{1}$ 9) and kinked Co(11 $\bar{2}$ 9) surfaces, respectively block the defect sites on these surfaces for further dissociation. Our findings revealed that CO dissociation ceases upon surface saturation, aligning with atomic O and C concentrations reaching 90% of the total step/kink site concentration on both the surfaces. At temperatures  $>500$  K, atomic C and O recombine and desorb as CO while at higher temperatures, C dissolves in the bulk and O remains on the surface. Since the barrier of CO dissociation is lower than of O removal from the Co surface, CO dissociation may not be the rate determining step in FTS.

## 6.7 Abbreviations

1. AES Auger electron spectrum
2.  $C_{ad}$  Adsorbed C
3. CN Coordination number
4. FCC Face-centered cubic
5. FTS Fischer-Tropsch synthesis
6. HCP Hexagonal close packed
7.  $k$  Thermodynamic equilibrium constant
8. LEED Low energy electron diffraction
9. ML Monolayer
10.  $O_{ad}$  Adsorbed O
11.  $R$  Universal gas constant ( $\text{m}^3 \cdot \text{Pa} \cdot \text{K}^{-1} \cdot \text{mol}^{-1}$ )
12.  $rWF$  Relative work function
13. STM Scanning tunneling microscopy
14.  $T$  Absolute temperature (K)
15. TPD Temperature programmed desorption
16. TP-WF Temperature programmed work function
17. UHV Ultrahigh Vacuum
18.  $X$  Concentration of defect sites
19. XPS X-ray photoelectron spectroscopy
20.  $\theta_{CO}$  CO coverage
21.  $\theta_C$  Carbon coverage
22.  $\theta_O$  Oxygen coverage
23.  $I_C$  Peak-to-peak intensity of C
24.  $I_{Co}$  Peak-to-peak intensity of Cobalt
25.  $\Delta H^O$  Change of enthalpy ( $\text{kJ mol}^{-1}$ )

26.  $r_{CO_{diss}}$  Rate of CO dissociation ( $ML\ s^{-1}$ )
27.  $k_B$  Boltzmann constant ( $JK^{-1}$ )
28.  $\Delta G^\ddagger$  Gibbs free energy (J)

# Chapter 7

## Conclusions

Surface science, an interdisciplinary field focused on the physical and chemical processes occurring at phase interfaces such as solid-gas and solid-vacuum, plays a crucial role in understanding molecular adsorption and organization at the atomic level. This understanding is fundamental to unraveling the mechanisms behind surface chemical reactions and heterogeneous catalysis, which forms the basis for studying the elementary reaction steps of Co based FTS in this thesis. This chapter presents the key conclusions of this dissertation, addressing the research questions posed in the introduction and comparing the findings with real-world conditions.

### 7.1 Chapter 3 : Influence of defect sites on CO adsorption at low coverage

Chapter 3 examines and compares the adsorption of CO on flat Co(0001), sputtered Co(0001), stepped Co(10 $\bar{1}$ 9), and kinked Co(11 $\bar{2}$ 9) surfaces. The focus is primarily on low CO coverage in order to study the adsorption strength of CO on the Co atoms, with minimal interference from lateral interactions. IR spectroscopy results indicated the presence of CO adsorbed on the top sites of both the terraces and the steps of the surfaces studied. XPS analysis enabled us to distinguish step site adsorption and terrace adsorption based on binding energy (BE) differences. It revealed that there was a slight preference for the step sites over terrace sites in CO adsorption. This finding is supported by density functional theory (DFT) simulations, which demonstrated minimal variation in CO adsorption energies on the top sites of surface atoms with different coordination numbers. The small difference in CO adsorption energy between undercoordinated sites and terrace sites of Co indicated a lack of a strong driving force for CO-induced surface reconstruction. Consequently, under typical reaction conditions, significant CO-induced reconstruction is unlikely to occur, and Co catalyst nanoparticles are expected to retain their initial structure with-

out transforming into highly faceted nanoparticles. This also implies that the defect sites will remain accessible for further adsorption during FTS since no poisoning of the active sites occurs by strongly bound CO. However, the influence of strong CO adsorption on the FT chain growth on the open surfaces was not investigated in this thesis.

In this chapter, CO adsorption on flat, stepped, and kinked cobalt surfaces was studied using both ultrahigh vacuum (UHV) experiments and DFT modeling. While each approach has its limitations, integrating data from both methods enabled a highly detailed understanding of how surface structure influences CO adsorption. For example, experimental data obtained in the UHV chamber, such as temperature-programmed desorption (TPD) spectra, were influenced by background desorption and signals from other surface processes, including hydrogen and CO desorption. To address this, a quadrupole mass spectrometer (QMS) with an aperture was utilized, which minimized signals from desorption on non-targeted areas of the sample holder, resulting in a consistent background signal that could be effectively subtracted.

On the theoretical side, DFT modeling provided valuable insights into adsorption energies and activation barriers on specific surface structures, supporting a more comprehensive interpretation of the data. However, DFT has its own limitations, such as challenges in precisely predicting CO adsorption sites and energies on transition metal surfaces and accounting for van der Waals interactions. Thus, DFT results were experimentally validated to ensure accuracy. By combining both experimental and theoretical approaches, this study achieved a comprehensive, molecular-level understanding of CO adsorption on the low and high index Co surfaces. This integration of experiment and theory allowed for a more robust analysis of the complex interplay between experimental observations and theoretical predictions, thereby enhancing our understanding of the underlying processes involved in FTS.

## 7.2 Chapter 4 and 5 : CO and hydrogen co-adsorption on Co(0001) and Co(11 $\bar{2}$ 9)

During FTS, CO and hydrogen adsorb onto the catalyst surface, leading to surface crowding and lateral interactions between the adsorbates. These interactions have a significant impact on the adsorption behavior of CO and hydrogen. Therefore, non-reactive co-adsorption of CO and hydrogen on the flat Co(0001) surface is investigated to gain further insights into the co-adsorption phenomena in chapter 4. Our investigations of the co-adsorption system reveal that as the coverage of atomic hydrogen ( $H_{ad}$ ) on Co(0001) increases at low surface temperatures, the capacity of CO to co-adsorb with  $H_{ad}$  decreases. This decrease in CO adsorption shows a linear trend. However a single-site model is not sufficient to capture the complexity of CO-H co-adsorption, as the saturation coverages of the two adsorbates do not

sum to unity with the single-site model. By considering adsorbate segregation into ad-islands, we were able to obtain a reasonable quantitative description of the correlation between  $\theta_{CO}$  and  $\theta_H$  values in our model system. CO and hydrogen form known structures within the islands but still get mutually influenced on adsorption. Our findings reveal that when the Co(0001) surface is covered with 1ML  $H_{ad}$ , very little CO can still be co-adsorbed. Similarly, when the surface is saturated with  $CO_{ad}$ , minimal hydrogen co-adsorption occurs. This behavior can be attributed to the occupation of sites required for dissociative hydrogen adsorption by CO molecules or their inaccessibility due to neighboring CO molecules, thereby increasing the energy barrier for hydrogen's dissociative adsorption. Dosing hydrogen in the presence of a hot tungsten filament results into hot hydrogen atoms and molecules enabling them to overcome the dissociative adsorption barrier on Co(0001) surfaces pre-covered with CO.

In chapter 5, the influence of surface structure on the co-adsorption of hydrogen and CO is investigated. For pure hydrogen, our study demonstrates a significant enhancement in the dissociative adsorption of  $H_2$  on the kinked Co(11 $\bar{2}$ 9) compared to the flat Co(0001) surface, attributed to the barrierless route for dissociative adsorption provided by the kinks on the surface. For CO, we found that a higher saturation coverage of CO can be achieved on the kinked Co(11 $\bar{2}$ 9) surface compared to the flat Co(0001) surface at low temperature. Notably, no discernible LEED patterns were observed during CO adsorption on Co(11 $\bar{2}$ 9) at 100 K, indicating the absence of ordered structures.

Additionally, chapter 5 explores the non-reactive co-adsorption of CO and hydrogen on the Co(11 $\bar{2}$ 9) surface, comparing it to the flat Co(0001) surface in order to highlight the role of step sites on the co-adsorption process. Two adsorption sequences are again investigated: hydrogen followed by CO, and CO followed by hydrogen. In the first sequence, where hydrogen is dosed before CO, our findings reveal a decreasing adsorption capacity for CO as hydrogen coverage increases. Our results suggest that the co-adsorption of CO and hydrogen on the kinked Co(11 $\bar{2}$ 9) surface can be explained by the formation of a segregated layer. However, this observation does not fully capture the complexity of CO-H co-adsorption, as the combined saturation coverages of these two adsorbates exceed unity. Based on the CO adsorption behavior on the kinked Co(11 $\bar{2}$ 9) surface outlined in Chapter 3 and the high coverage observed in the co-adsorption system with hydrogen, a plausible hypothesis is that CO adsorbs at step-top sites in a tilted orientation, leaving room for dissociative hydrogen adsorption at nearby hollow sites. The exact adsorption configurations of CO and hydrogen on both terraces and steps remain unclear and require further investigation. This contrasts with the flat Co(0001) surface, where findings align well with the segregation model.

For the second adsorption sequence, where CO is adsorbed first followed by hydrogen, a surface saturated with  $CO_{ad}$  exhibits minimal hydrogen adsorption. This inhibition of hydrogen adsorption by CO can be attributed to CO occupying step

sites or obstructing these sites due to the presence of neighboring CO molecules, as hydrogen dissociation primarily occurs at step sites. CO can adsorb on both terrace and step sites without a clear preference (as shown in chapter 3), so adsorbate coverage at the steps follows the trend of overall CO coverage. Thus, steps remain available for hydrogen dissociation up to high CO coverages until the surface saturation is achieved.

Lateral interactions can profoundly influence heterogeneous catalytic reaction kinetics by altering the configurations of adsorbates, subsequently impacting catalytic activity. When adsorbates interact repulsively, the effects on configurations and reactivity are mainly observed at high coverages, where adsorbates are forced into close proximity. This phenomenon is evident on Co(0001) and Co(11 $\bar{2}$ 9) surfaces during exposure to CO and hydrogen sequentially. Repulsive interactions lead to the destabilization of H atoms and CO molecules in different configurations. In contrast, attractive interactions are observed even at low coverages, resulting in the formation of adsorbate islands on the surface. The presence of these islands can limit the contact between species in surface reactions, hindering homogeneous mixing.

### 7.3 Chapter 6 : CO dissociation

Although the importance of defects and undercoordinated sites in the dissociation of CO is widely acknowledged, there is ongoing debate regarding the specific nature of active sites responsible for CO dissociation—an essential step in FT synthesis. Therefore, we compare the CO dissociation behavior on the stepped Co(10 $\bar{1}$ 9) and kinked Co(11 $\bar{2}$ 9) surfaces to elucidate the reactivity of these two types of defect sites. Chapter 6 of this thesis focuses on a comparative analysis of the kinetics of CO dissociation on stepped Co(10 $\bar{1}$ 9) and kinked Co(11 $\bar{2}$ 9) surfaces. Our investigations reveal that the dissociation reaction exhibits a similar Gibbs free energy barrier on both stepped and kinked Co surfaces, approximately 110 kJ mol<sup>-1</sup>. However, the step and kink sites on the surfaces can become blocked by atomic O and C, thereby hindering further dissociation. It was also found that both B5-A and B5-B sites are active for CO dissociation to the same extent on the stepped Co(10 $\bar{1}$ 9) surface. These findings provide valuable insights into the CO dissociation process on different surface structures of cobalt catalysts, highlighting the importance of step-edge sites and the potential limitations imposed by the presence of atomic oxygen and carbon species.

### 7.4 Future Prospects

We conducted a series of reactions on cobalt single crystal surfaces with distinct orientations, including flat, defective, stepped, and kinked structures. These studies were motivated by Fischer-Tropsch Synthesis (FTS), making the findings valuable for both academic insight and potential industrial application. While our surface

science approach yielded promising results, several challenges remain, suggesting areas for further exploration. One particularly compelling direction for future research is to examine how steps and kinks influence CO adsorption at high CO coverage, especially given the impact of lateral interactions on densely populated surfaces. High CO coverage, typical under FTS conditions, is expected to significantly raise the energy barrier for CO dissociation, likely favoring alternative dissociation pathways and chain-growth mechanisms within the FT process. Advancing this research could involve integrating the findings of this study with high-coverage CO adsorption studies using techniques such as temperature-programmed desorption (TPD), X-ray photoelectron spectroscopy (XPS), and infrared (IR) spectroscopy.

One primary challenge we encountered when studying CO and hydrogen co-adsorption on the kinked Co(11 $\bar{2}$ 9) surface was the limitation in resolving structural details using the techniques at hand. A more systematic approach, beginning with co-adsorption studies on stepped surfaces and building on insights gained from narrow terrace surfaces, as discussed in this thesis, could deepen our understanding of CO and hydrogen co-adsorption on kinked surfaces. Additionally, the use of scanning tunneling microscopy (STM) could help determine whether CO molecules occupy step sites or leave them vacant, potentially opening low-barrier pathways for hydrogen dissociation and adsorption on the surface. Performing co-adsorption experiments on the stepped Co(10 $\bar{1}$ 9) at temperatures below 100 K, followed by structural analysis as the layer is warmed, could provide insights into the role of ordering in introducing activation barriers for rearrangement and site changes. Further theoretical studies on the kinked Co(11 $\bar{2}$ 9) surface are required to better understand mutual interactions as a function of surface structure and co-adsorbate combinations. Calculations that incorporate multiple interaction types would provide a more comprehensive understanding of these complex systems. The ordering of co-adsorbates is still poorly understood, particularly with regard to how it affects adsorption site occupation and reactivity. Overall, understanding the interplay between adsorption energies and lateral interactions is crucial for comprehending surface restructuring and its implications for catalytic activity in heterogeneous catalysis.

During CO dissociation experiments on stepped and kinked surfaces at the synchrotron facility - FlexPES beamline, a major challenge was the rapid contamination of the surfaces by surrounding gases in the XPS chamber. To address this, future research should focus on conducting CO dissociation experiments on cleaner, defect-rich surfaces, combined with XPS analysis to better understand the adsorption behavior of atomic O and C following CO dissociation. These insights will be crucial for optimizing Fischer-Tropsch Synthesis (FTS) under realistic reaction conditions. Step sites, which are highly reactive for CO dissociation under UHV conditions, may become poisoned under actual FT reaction environments. This is why one should be careful in extrapolating the data obtained under UHV conditions to high gas pressure. By addressing these challenges and incorporating a complementary set of experimental techniques like steady-state isotopic transient kinetic analysis (SSITKA),

we can advance our understanding of CO adsorption and dissociation mechanisms on stepped and kinked surfaces, paving the way for improved catalytic applications and industrial processes.

## 7.5 Abbreviations

1. BE Binding Energy (eV)
2. DFT Density Functional Theory
3. FTS Fischer-Tropsch synthesis
4.  $H_{ad}$  Adsorbed hydrogen
5. IR Infrared
6. LEED Low energy electron diffraction
7. QMS Quadrupole mass spectrometer
8. FTS Fischer-Tropsch synthesis
9. SSITKA Steady-state isotopic transient kinetic analysis
10. TPD Temperature programmed desorption
11. UHV Ultrahigh Vacuum
12. XPS X-ray photoelectron spectroscopy
13.  $\theta_{CO}$  CO coverage
14.  $\theta_H$  Hydrogen coverage



# Chapter 8

## List of publications

### 8.1 Publications within the scope of this thesis

#### Chapter 4 and 5

- C.J. Weststrate, Daniel Garcia Rodriguez, Devyani Sharma, and J.W. Niemantsverdriet. "Structure-dependent adsorption and desorption of hydrogen on FCC and HCP cobalt surfaces". *Journal of Catalysis*, 405:303–312, 2021.

### 8.2 Publications outside the scope of this thesis

- C. J. Weststrate, Devyani Sharma, Daniel Garcia Rodriguez, Michael A. Gleeson, Hans O.A. Fredriksson, and J.W. Niemantsverdriet. "Reactivity of  $C_3H_x$  adsorbates in presence of co-adsorbed co and hydrogen: Testing fischer-tropsch chain growth mechanisms". *Topics in Catalysis*, 63:1412–1423, 2020.
- C. J. Weststrate, Devyani Sharma, Daniel Garcia Rodriguez, Michael A. Gleeson, Hans O.A. Fredriksson, and J.W. Niemantsverdriet. "Mechanistic insight into carbon-carbon bond formation on cobalt under simulated fischer-tropsch synthesis conditions". *Nature Communications*, 11, 2020.
- C. J. Weststrate, Devyani Sharma, Daniel García Rodríguez, Hans O.A. Fredriksson, and J.W. Niemantsverdriet. "Water formation kinetics on co(0001) at low and near-ambient hydrogen pressures in the context of fischer-tropsch synthesis". *Journal of Physical Chemistry C*, 2022.
- C. J. Weststrate, Devyani Sharma, Michael A. Gleeson, and J. W. Niemantsverdriet. "Water and hydroxyl reactivity on flat and stepped cobalt surfaces". *Journal of Physical Chemistry C*, 127:2974–2980, 2023.

- Gregory Collinge, Devyani Sharma, Jean-Sabin Mcewen, and Mark Saeys. “Rate expressions in mean field microkinetic models incorporating multiple types of active sites”.

### **8.3 Contributions by the author**

The research presented in this dissertation was primarily conducted by the author. The computational results presented in chapter 3 of this thesis were contributed by Dr. Thobani Gambu from the University of Gent, as a part of a collaborative effort during the author’s exchange program at the university. Other than the computational results, the author designed the study, collected and analyzed the data and wrote all chapters of the dissertation.

# Bibliography

- [1] European Commission. "Causes of climate change". Downloaded on February 1<sup>st</sup>, 2025. URL [https://climate.ec.europa.eu/climate-change/causes-climate-change\\_en](https://climate.ec.europa.eu/climate-change/causes-climate-change_en).
- [2] B. Raj and O. Singh. "Study of Impacts of Global Warming on Climate Change: Rise in Sea Level and Disaster Frequency". *Global Warming - Impacts and Future Perspectives*, 2012.
- [3] Government of the Netherlands. "Climate change. downloaded on february 1<sup>st</sup>, 2025". URL <https://www.government.nl/topics/climate-change/dutch-vision-on-global-climate-action>.
- [4] J. Delbeke, A. Runge-Metzger, Y. Slingenberg, and J. Werksman. "The paris agreement". *European Union*, pages 24–45, 2019.
- [5] A. Shah, R. Fishwick, J. Wood, G. Leeke, S. Rigby, and M. Greaves. "A review of novel techniques for heavy oil and bitumen extraction and upgrading". *Energy and Environmental Science*, 3:700–714, 2010.
- [6] S. S. Kumar and H. Lim. "An overview of water electrolysis technologies for green hydrogen production". *Energy Reports*, 8:13793–13813, 2022.
- [7] J. B. Senderens and P. Sabatier. "New synthesis of methane". *C.R. Acad. Sci Paris*, 82: 514–516, 1902.
- [8] F. Fischer and H. Tropsch. "The synthesis of petroleum at atmospheric pressures from gasification products of coal". *Brennstoff-Chemie*, 7:97–104, 1926.
- [9] J. Van de Loosdrecht, F. G. Botes, I. M. Ciobica, A. Ferreira, P. Gibson, D. J. Moodley, A. M. Saib, J. L. Visagie, C. J. Weststrate, and J. W. Niemantsverdriet. *Fischer-Tropsch Synthesis: Catalysts and Chemistry*, volume 7. Oxford Elsevier Ltd., 2013. ISBN 9780080965291.
- [10] R. Zennaro, G. Pederzani, S. Morselli, S. Cheng, and C. H. Bartholomew. "Quantitative comparison of supported cobalt and iron Fischer Tropsch synthesis catalysts". *Studies in Surface Science and Catalysis*, 136:513–518, 2001.
- [11] E. Iglesia, S. L. Soled, and R. A. Fiato. "Fischer-Tropsch synthesis on cobalt and ruthenium. Metal dispersion and support effects on reaction rate and selectivity". *Journal of Catalysis*, 137(1):212–224, 1992.
- [12] L. J. France, P. P. Edwards, V. L. Kuznetsov, and H. Almegren. *Carbon Dioxide Utilisation: Closing the Carbon Cycle - chapter 10*. Elsevier B.V., 2015. ISBN 9780444627469.
- [13] R. A. Van Santen, A. J. Markvoort, I. A. W. Filot, M. M. Ghouri, and E. J. M. Hensen. "Mechanism and microkinetics of the Fischer-Tropsch reaction". *Physical Chemistry*

- Chemical Physics*, 15:17038–17063, 2013.
- [14] K. F. Tan, J. Xu, J. Chang, A. Borgna, and M. Saeys. “Carbon deposition on Co catalysts during Fischer-Tropsch synthesis: A computational and experimental study”. *Journal of Catalysis*, 274(2):121–129, 2010.
- [15] D.-K. Lee, J.-H. Lee, and S.-K. Ihm. “Effect of carbon deposits on carbon monoxide hydrogenation over alumina-supported cobalt catalyst”. *Applied Catalysis*, 36:199–207, 1988.
- [16] H. Schulz. “Principles of Fischer-Tropsch synthesis - Constraints on essential reactions ruling FT-selectivity”. *Catalysis Today*, 214:140–151, 2013.
- [17] A. Tavakoli, M. Sohrabi, and A. Kargari. “Application of Anderson-Schulz-Flory (ASF) equation in the product distribution of slurry phase FT synthesis with nanosized iron catalysts”. *Chemical Engineering Journal*, 136:358–363, 2008.
- [18] G. Henrici-Olivé and S. Olivé. “The Fischer-Tropsch Synthesis: Molecular weight distribution of primary products and reaction mechanism”. *Journal of the German Chemical Society*, 108:136–142, 1976.
- [19] S. H. Chan, O. L. Ding, and D. L. Hoang. “A Thermodynamic View of Partial Oxidation, Steam Reforming, and Autothermal Reforming on Methane”. *International Journal of Green Energy*, 1(2):265–278, 2004.
- [20] A. Y. Khodakov, W. Chu, and P. Fongarland. “Advances in the development of novel cobalt Fischer-Tropsch catalysts for synthesis of long-chain hydrocarbons and clean fuels”. *Chemical Reviews*, 107(5):1692–1744, 2007.
- [21] G. A. Beitel, A. Laskov, H. Oosterbeek, and E. W. Kuipers. “Polarization modulation infrared reflection absorption spectroscopy of CO adsorption on Co(0001) under a high-pressure regime”. *Journal of Physical Chemistry*, 100(30):12494–12502, 1996.
- [22] C. H. Wu, B. Eren, H. Bluhm, and M. B. Salmeron. “Ambient-pressure X-ray photoelectron spectroscopy study of cobalt foil model catalyst under CO, H<sub>2</sub>, and their mixtures”. *ACS Catalysis*, 7:1150–1157, 2017.
- [23] H. S. Taylor. “A theory of the catalytic surface”. *Proceedings of the Royal Society A*, 108(745):105–117, 1925.
- [24] G. A. Somorjai, R. L. York, D. Butcher, and J. Y. Park. “The evolution of model catalytic systems; studies of structure, bonding and dynamics from single crystal metal surfaces to nanoparticles, and from low pressure (<10<sup>-3</sup> Torr) to high pressure (>10<sup>-3</sup> Torr) to liquid interfaces”. *Physical Chemistry Chemical Physics*, 9(27):3500–3513, 2007.
- [25] Q. Ge and M. Neurock. “Adsorption and activation of CO over flat and stepped Co surfaces: A first principles analysis”. *Journal of Physical Chemistry B*, 110(31):15368–15380, 2006.
- [26] F. J. E. Scheijen, D. Curulla Ferré, and J. W. Niemantsverdriet. “Adsorption and dissociation of CO on body-centered cubic transition metals and alloys: effect of coverage and scaling relations”. *Journal of Physical Chemistry C*, 113:11041–11049, 2009.
- [27] J. W. Niemantsverdriet, A. M. van Der Kraan, W. L. van Dijk, and H. S. van Der Baan. “Behavior of metallic iron catalysts during Fischer-Tropsch Synthesis Studied with Mössbauer spectroscopy, X-ray diffraction, carbon content determination, and reaction kinetic measurements”. *Journal of Physical Chemistry*, 84:3363–3370, 1980.
- [28] E. Rytter and A. Holmen. “On the support in cobalt Fischer-Tropsch synthesis—emphasis on alumina and aluminates”. *Catalysis Today*, 275:11–19, 2016.
- [29] R. C. Reuel and C. H. Bartholomew. “Effects of support and dispersion on the CO

- hydrogenation activity/selectivity properties of cobalt". *Journal of catalysis*, 85:78–88, 1984.
- [30] A. S. Lisitsyn, A. V. Golovin, V. L. Kuznetsov, and Y. I. Yermakov. "Properties of Catalysts Prepared by Pyrolysis of  $\text{Co}_2(\text{CO})_8$  on Silica Containing Surface Ti Ions". *Journal of Catalysis*, 95:527–538, 1985.
- [31] E. Iglesia. "General review design, synthesis, and use of cobalt-based Fischer-Tropsch synthesis catalysts". *Applied Catalysis A: General*, 161:59–78, 1997.
- [32] G. L. Bezemer, J. H. Bitter, H. P. C. E. Kuipers, H. Oosterbeek, J. E. Holewijn, X. Xu, F. Kapteijn, A. J. Van Dillen, and K. P. De Jong. "Cobalt particle size effects in the Fischer-Tropsch reaction studied with carbon nanofiber supported catalysts". *Journal of the American Chemical Society*, 128(12):3956–3964, 2006.
- [33] Ø. Borg, J. C. Walmsley, R. Dehghan, B. S. Tanem, E. A. Blekkan, S. Eri, E. Rytter, and A. Holmen. "Electron microscopy study of  $\gamma\text{-Al}_2\text{O}_3$  supported cobalt Fischer-Tropsch synthesis catalysts". *Catalysis Letters*, 126:224–230, 2008.
- [34] A. Barbier, A. Tuel, G. A. Martin, I. Arcon, and A. Kodre. "Characterization and catalytic behavior of  $\text{CO}/\text{SiO}_2$  catalysts: Influence of dispersion in the Fischer-Tropsch reaction". *Journal of Catalysis*, 200:106–116, 2001.
- [35] G. L. Bezemer, A. van Laak, A. J. van Dillen, and K. P. de Jong. "Cobalt supported on carbon nanofibers - a promising novel Fischer-Tropsch catalyst". *Studies in Surface Science and Catalysis*, 147:259–264, 2004.
- [36] A. Martínez and G. Prieto. "Breaking the dispersion-reducibility dependence in oxide-supported cobalt nanoparticles". *Journal of Catalysis*, 245:470–476, 2007.
- [37] S. L. Soled, E. Iglesia, R. A. Fiato, J. E. Baumgartner, H. Vroman, and S. Miseo. "Control of metal dispersion and structure by changes in the solid-state chemistry of supported cobalt Fischer-Tropsch catalysts". *Topics in Catalysis*, 26:101–109, 2003.
- [38] X. Y. Quek, I. A. W. Filot, R. Pestman, R. A. van Santen, V. Petkov, and E. J. M. Hensen. "Correlating Fischer-Tropsch activity to Ru nanoparticle surface structure as probed by high-energy X-ray diffraction". *Chemical Communications*, 50:6005–6008, 2014.
- [39] R. A. Van Santen, M. M. Ghouri, S. Shetty, and E. M. H. Hensen. "Structure sensitivity of the fischer-tropsch reaction; molecular kinetics simulations". *Catalysis Science and Technology*, 1:891–911, 2011.
- [40] R. A. Van Santen. "Complementary structure sensitive and insensitive catalytic relationships". *Accounts of Chemical Research*, 42:57–66, 2009.
- [41] C. J. Weststrate, P. Van Helden, J. Van De Loosdrecht, and J. W. Niemantsverdriet. "Elementary steps in Fischer-Tropsch synthesis: CO bond scission, CO oxidation and surface carbiding on  $\text{Co}(0001)$ ". *Surface Science*, 648:60–66, 2016.
- [42] X. Q. Gong, R. Raval, and P. Hu. "CO dissociation and O removal on  $\text{Co}(0001)$ : A density functional theory study". *Surface Science*, 562:247–256, 2004.
- [43] C. J. Weststrate, M. Mahmoodinia, M. H. Farstad, I. H. Svenum, M. D. Strømsheim, J. W. Niemantsverdriet, and H. J. Venvik. "Interaction of hydrogen with flat (0001) and corrugated (11–20) and (10–12) cobalt surfaces: Insights from experiment and theory". *Catalysis Today*, 342(April):124–130, 2020.
- [44] C. J. Weststrate, D. G. Rodriguez, D. Sharma, and J. W. Niemantsverdriet. "Structure-dependent adsorption and desorption of hydrogen on FCC and HCP cobalt surfaces". *Journal of Catalysis*, 405:303–312, 2021.
- [45] P. Van Helden, J. A. Van Den Berg, and C. J. Weststrate. "Hydrogen adsorption on Co

- surfaces: A density functional theory and temperature programmed desorption study". *ACS Catalysis*, 2(6):1097–1107, 2012.
- [46] I. A. W. Filot. "Quantum Chemical and Microkinetic Modeling of the Fischer-Tropsch Reaction". *Doctoral Thesis, Eindhoven University of Technology*, 2015.
- [47] I. A. W. Filot, R. A. Van Santen, and E. J. M. Hensen. "Quantum chemistry of the Fischer-Tropsch reaction catalysed by a stepped ruthenium surface". *Catalysis Science and Technology*, 4(9):3129–3140, 2014.
- [48] H. P. Koch, P. Singnurkar, R. Schennach, A. Stroppa, and F. Mittendorfer. "A RAIRS, TPD, and DFT study of carbon monoxide adsorption on stepped Rh(553)". *Journal of Physical Chemistry C*, 112(3):806–812, 2008.
- [49] J. D. Batteas, D. E. Gardin, M. A. Van Hove, and G. A. Somorjai. "A LEED, TDS, and HREELS study of CO adsorbed on the Rh(311) stepped surface". *Surface Science*, 297(1):11–18, 1993.
- [50] D. P. Woodruff. *The Chemical Physics of Solid Surfaces: Surface Dynamics*, volume 11. 2003. ISBN 0444514376.
- [51] M. D. Strømsheim, I. H. Svenum, M. H. Farstad, C. J. K. Weststrate, A. Borg, and H. J. Venvik. "CO-Induced Surface Reconstruction of the Co(11 $\bar{2}$ 0) Surface - A Combined Theoretical and Experimental Investigation". *Journal of Physical Chemistry C*, 124(52):28488–28499, 2020.
- [52] C. J. Weststrate, J. Van De Loosdrecht, and J. W. Niemantsverdriet. "Spectroscopic insights into cobalt-catalyzed Fischer-Tropsch synthesis: A review of the carbon monoxide interaction with single crystalline surfaces of cobalt". *Journal of Catalysis*, 342:1–16, 2016.
- [53] J. M. Heras, H. Papp, and W. Spiess. "Face specificity of the H<sub>2</sub>O adsorption and decomposition on Co surfaces - a LEED, UPS, sp and TPD study". *Surface Science*, 117(1-3):590–604, 1982.
- [54] S. Hüfner. *Springer-Verlag Berlin Heidelberg GmbH*. 3<sup>rd</sup> edition, 2010. ISBN 9783642075209.
- [55] J. W. Niemantsverdriet. *Spectroscopy in Catalysis*. John Wiley and Sons, 3<sup>rd</sup> edition, 2007. ISBN 9783527611348.
- [56] D. P. Woodruff and T. A. Delchar. *Modern Techniques of Surface Science*. Cambridge University Press, 2<sup>nd</sup> edition, 1994. ISBN 0521414679.
- [57] S. Mischler and H. E. Bishop. "A novel practical approach to the quantification of Auger electron spectroscopy". *Surface and Interface Analysis*, 17(6):315–319, 1991.
- [58] D. Klyachko and S. Borodyansky. "Step function determination of Auger peak intensity". *World Intellectual Property Organization*, (WO 02/069363 A2), 2002.
- [59] John Wolstenholme. *Auger electron spectroscopy*. Momentum Press, 2015. ISBN 9781606506820.
- [60] M. A. van Hove and S. Y. Tong. *Surface crystallography by LEED: Theory, Computation and Structural results*. Springer Berlin, Heidelberg, 1<sup>st</sup> edition, 1979. ISBN 9783642671975.
- [61] M. A. van Hove, W. H. Weinberg, and C. Chi-Ming. *Low-energy electron diffraction: experiment, theory and surface structure determination*, volume 6. Springer Science and Business Media, 2011. ISBN 9783642827235.
- [62] M. A. van Hove and G. A. Somorjai. "A new microfacet notation for high-Miller-index surfaces of cubic materials with terrace, step and kink structures". *Surface Science*, 92(2-3):489–518, 1980.

- [63] T. Zubkov, G. A. Morgan, J. T. Yates, O. Köhlert, M. Lisowski, R. Schillinger, D. Fick, and H. J. Jänsch. "The effect of atomic steps on adsorption and desorption of CO on Ru(1 0 9)". *Surface Science*, 526(1-2):57–71, 2003.
- [64] W. Hoffmann and C. Benndorf. "Water adsorption structures on flat and stepped Ru(0001) surfaces". *Journal of Vacuum Science and Technology A: Vacuum, Surfaces, and Films*, 18(4):1520–1525, 2000.
- [65] B. Böller, K. M. Durner, and J. Wintterlin. "The active sites of a working Fischer–Tropsch catalyst revealed by operando scanning tunnelling microscopy". *Nature Catalysis*, 2(11):1027–1034, 2019.
- [66] T. E. Madey and D. Menzel. "Adsorption of CO on (001) ruthenium at temperatures 300 K". *Japanese Journal of Applied Physics*, 13(S2):229–235, 1974.
- [67] R. I. Masel. *Principles of Adsorption and Reaction on Solid Surfaces*. John Wiley and Sons, Hoboken, U.S.A, 1<sup>st</sup> edition, 1996. ISBN 9780471303923.
- [68] P. A. Redhead. "Thermal desorption of gases". *Vacuum*, 12:203–211, 1962.
- [69] J. Kuppers and E. Habenschaden. "Evaluation of flash desorption spectra". *Surface Science Letters*, 138(1):147–150, 1984.
- [70] A. M. de Jong and J. W. Niemantsverdriet. "Thermal desorption analysis: Comparative test of ten commonly applied procedures". *Surface Science*, 233(3):355–365, 1990.
- [71] C. T. Campbell, L. Árnadóttir, and J. R. V. Sellers. "Kinetic prefactors of reactions on solid surfaces". *Zeitschrift für Physikalische Chemie*, 227(11):1435–1454, 2013.
- [72] R. C. Baetzold and G. A. Somorjai. "Pre-exponential factors in surface reactions". *Journal of Catalysis*, 45(1):94–105, 1976.
- [73] J. W. Niemantsverdriet. "Thin metal films and gas chemisorption, studies in surface science and catalysis". *Applied Catalysis*, 35(1):188–189, 1987.
- [74] R. Smoluchowski. "Anisotropy of the electronic work function of metals". *Physical Review*, 60(9):661–674, 1941.
- [75] N. D. Lang and W. Kohn. "Theory of metal surfaces: Charge density and surface energy". *Physical Review B*, 1(12):4555–4568, 1970.
- [76] I. Chorkendorff and J. W. Niemantsverdriet. *Concepts of Modern Catalysis and Kinetics*. John Wiley and Sons, 3<sup>rd</sup> edition, 2017. ISBN 9783527602650.
- [77] Y. Li and G. A. Somorjai. *Introduction to Surface Chemistry and Catalysis*. John Wiley and Sons, New Jersey, 2<sup>nd</sup> edition, 1994. ISBN 9780470508237.
- [78] B. Çağlar. "Bond activation process of biomass-derived molecules". *Doctoral Thesis*, Eindhoven University of Technology, 2014.
- [79] P. Atkins and J. de Paula. *Atkins' Physical Chemistry*. Oxford University Press, Great Britain, 8<sup>th</sup> edition, 2006. ISBN 9780716787594.
- [80] Friedrich M. Hoffmann. "Infrared reflection absorption spectroscopy". *Surface Science Reports*, (3):107–192, 1983.
- [81] G. Blyholder. "Molecular orbital view of chemisorbed carbon monoxide". *Journal of Physical Chemistry*, 68(10):2772–2778, 1964.
- [82] G. Blyholder. "CNDO model of carbon monoxide on Nickel". *Journal of Physical Chemistry*, 126(6):756–761, 1975.
- [83] R. P. Eischens, W. A. Pliskin, and S. A. Francis. "Infrared spectra of chemisorbed carbon monoxide". *The Journal of Chemical Physics*, 22(10):1786–1787, 1954.
- [84] S. Dahl, E. Törnqvist, and I. Chorkendorff. "Dissociative adsorption of N<sub>2</sub> on Ru(0001):

- A surface reaction totally dominated by steps". *Journal of Catalysis*, 192(2):381–390, 2000.
- [85] B. N. J. Persson and R. Ryberg. "Vibrational interaction between molecules adsorbed on a metal surface: The dipole-dipole interaction". *Physical Review B*, 24(12):6954–6970, 1981.
- [86] C. J. Weststrate and J. W. Niemantsverdriet. "CO adsorption on Co(0001) revisited: High-coverage CO superstructures on the close-packed surface of cobalt". *Journal of Catalysis*, 408:142–154, 2022.
- [87] P. Hollins. "Influence of Dipole Coupling on the Infrared Spectra of Adsorbed Species and Its Significance for the Interpretation of Transmission Spectra From Supported Metal Catalysts.". *Adsorption Science and Technology*, 2(3):177–193, 1985.
- [88] F. Fischer and H. Tropsch. "The preparation of synthetic oil mixtures (synthol) from carbon monoxide and hydrogen". *Brennst. Chem*, 4:276–285, 1923.
- [89] H. Karaca, O. V. Safonova, S. Chambrey, P. Fongarland, P. Roussel, A. Griboval-Constant, M. Lacroix, and A. Y. Khodakov. "Structure and catalytic performance of Pt-promoted alumina-supported cobalt catalysts under realistic conditions of Fischer-Tropsch synthesis". *Journal of Catalysis*, 277(1):14–26, 2011.
- [90] M. K. Gnanamani, G. Jacobs, W. D. Shafer, and B. H. Davis. "Fischer-Tropsch synthesis: Activity of metallic phases of cobalt supported on silica". *Catalysis Today*, 215:13–17, 2013.
- [91] J. X. Liu, H. Y. Su, D. P. Sun, B. Y. Zhang, and W. X. Li. "Crystallographic dependence of CO activation on cobalt catalysts: HCP versus FCC". *Journal of the American Chemical Society*, 135(44):16284–16287, 2013.
- [92] R. Pestman, W. Chen, and E. Hensen. "Insight into the Rate-Determining Step and Active Sites in the Fischer-Tropsch Reaction over Cobalt Catalysts". *ACS Catalysis*, 9(5):4189–4195, 2019.
- [93] F. Calle-Vallejo, D. Loffreda, M. T. M. Koper, and P. Sautet. "Introducing structural sensitivity into adsorption-energy scaling relations by means of coordination numbers". *Nature Chemistry*, 7(5):403–410, 2015.
- [94] J. E. De Vrieze, G. M. Bremmer, M. Aly, V. Navarro, J. W. Thybaut, P. J. Kooyman, and M. Saeys. "Shape of Cobalt and Platinum Nanoparticles under a CO Atmosphere: A Combined in Situ TEM and Computational Catalysis Study". *ACS Catalysis*, 9(8):7449–7456, 2019.
- [95] J. P. Den Breejen, P. B. Radstake, G. L. Bezemer, J. H. Bitter, V. Frøseth, A. Holmen, and K. P. De Jong. "On the origin of the cobalt particle size effects in Fischer-Tropsch catalysis". *Journal of the American Chemical Society*, 131(20):7197–7203, 2009.
- [96] D. Hibbitts, E. Dybeck, T. Lawlor, M. Neurock, and E. Iglesia. "Preferential activation of CO near hydrocarbon chains during Fischer-Tropsch synthesis on Ru". *Journal of Catalysis*, 337:91–101, 2016.
- [97] T. Ramsvik, A. Borg, M. Kildemo, S. Raaen, A. Matsuura, A. J. Jaworowski, T. Worren, and M. Leandersson. "Molecular vibrations in core-ionised CO adsorbed on Co(0001) and Rh(1 0 0)". *Surface Science*, 492(1-2):152–160, 2001.
- [98] J. Lahtinen, J. Vaari, K. Kauraala, E. A. Soares, and M. A. Van Hove. "LEED investigations on Co (0001): The ( $\sqrt{3} \times \sqrt{3}$ ) R30° - CO overlayer". *Surface Science*, 448(2-3):269–278, 2000.
- [99] J. Lahtinen, J. Vaari, and K. Kauraala. "Adsorption and structure dependent

- desorption of CO on Co(0001)". *Surface Science*, 418(3):502–510, 1998.
- [100] F. Greuter, D. Heskett, and E. W. Plummer. "Chemisorption of Co(0001) - structure and electronic properties". *Physical Review B*, 27:7117–7138, 1983.
- [101] H. Papp. "Chemisorption and reactivity of carbon monoxide on a Co(11 $\bar{2}$ 0) single crystal surface; Studied by LEED, UPS, EELS, AES and work function measurements". *Surface Science*, 149(2-3):460–470, 1985.
- [102] D. Heskett, F. Greuter, H.-J. Freund, and E. W. Plummer. "Angle resolved photoemission study of CO/Co(0001)". *Journal of Vacuum Science and Technology*, 20: 623–624, 1982.
- [103] M. E. Bridge, C. M. Comrie, and L. M. Lambert. "Carbon monoxide on Co(0001)". *Surface Science*, 67:393–404, 1977.
- [104] G. T. K. Gunasooriya, A. P. Van Bavel, H. P. C. E. Kuipers, and M. Saeys. "CO adsorption on cobalt: Prediction of stable surface phases". *Surface Science*, 642:L6–L10, 2015.
- [105] R. B. Rankin. "Similarities and differences for atomic and diatomic molecule adsorption on the B-5 type sites of the HCP(101 $\bar{6}$ ) surfaces of Co, Os, and Ru from DFT calculations". *Heliyon*, 5(6):e01924, 2019.
- [106] H. Aizawa and S. Tsuneyuki. "First-principles study of CO bonding to Pt(111): validity of the Blyholder model". *Surface Science Letters*, 399:L364–L370, 1998.
- [107] Y. Tison, K. Nielsen, D. J. Mowbray, L. Bech, C. Holse, F. Calle-Vallejo, K. Andersen, J. J. Mortensen, K. W. Jacobsen, and J. H. Nielsen. "Scanning tunneling microscopy evidence for the dissociation of carbon monoxide on ruthenium steps". *Journal of Physical Chemistry C*, 116(27):14350–14359, 2012.
- [108] A. Abrami, M. Barnaba, L. Battistello, A. Bianco, B. Brena, G. Cautero, Q. H. Chen, D. Cocco, G. Comelli, S. Contrino, F. DeBona, S. Di Fonzo, C. Fava, P. Finetti, P. Furlan, A. Galimberti, A. Gambitta, D. Giuressi, R. Godnig, W. Jark, S. Lizzit, F. Mazzolini, P. Melpignano, L. Olivi, G. Paolucci, R. Pugliese, S. N. Qian, R. Rosei, G. Sandrin, A. Savoia, R. Sergo, G. Sostero, R. Tommasini, M. Tudor, D. Vivoda, F. Q. Wei, and F. Zanini. "Super ESCA: First beamline operating at ELETTRA". *Review of Scientific Instruments*, 66(2):1618–1620, 1995.
- [109] D. A. Shirley. "High-resolution X-ray photoemission spectrum of the valence bands of gold". *Physical Review B*, 5(12):4709–4714, 1972.
- [110] G. Kresse and J. Hafner. "Ab initio molecular dynamics for liquid metals". *Physical Review B*, 47(1):558–561, 1993.
- [111] G. Kresse and J. Hafner. "Ab initio molecular dynamics for open-shell transition metals". *Physical Review B*, 48(17):13115–13118, 1993.
- [112] K. Lee, É. D. Murray, L. Kong, B. I. Lundqvist, and D. C. Langreth. "Higher-accuracy van der Waals density functional". *Physical Review B - Condensed Matter and Materials Physics*, 82(8):1–4, 2010.
- [113] J. Klimeš, D. R. Bowler, and A. Michaelides. "Van der Waals density functionals applied to solids". *Physical Review B - Condensed Matter and Materials Physics*, 83(19): 195131–1–1195131–13, 2011.
- [114] P. J. Feibelman, B. Hammer, J. K. Nørskov, F. Wagner, M. Scheffler, R. Stump, R. Watwe, and J. Dumesic. "The CO/Pt(111) Puzzle a". *Journal of Physical Chemistry B*, 105(18): 4018–4025, 2001.
- [115] P. Janthon, F. Viñes, J. Sirirajarensre, J. Limtrakul, and F. Illas. "Adding Pieces to the

- CO/Pt(111) Puzzle: The Role of Dispersion". *Journal of Physical Chemistry C*, 121(7): 3970–3977, 2017.
- [116] A. Patra, H. Peng, J. Sun, and J. P. Perdew. "Rethinking CO adsorption on transition-metal surfaces: Effect of density-driven self-interaction errors". *Physical Review B*, 100(3):1–8, 2019.
- [117] M. Methfessel and A. T. Paxton. "High-precision sampling for brillouin-zone integration in metals". *Physical Review B*, 40(6):15–1989.
- [118] V. K. Jones, L. R. Neubauer, and C. H. Bartholomew. "Effects of crystallite size and support on the CO hydrogenation activity/selectivity properties of Fe/carbon". *Journal of Physical Chemistry*, 90(20):4832–4839, 1986.
- [119] M. A. Petersen, J. A. Van Den Berg, I. M. Ciobîcă, and P. Van Helden. "Revisiting CO Activation on Co Catalysts: Impact of Step and Kink Sites from DFT". *ACS Catalysis*, 7(3):1984–1992, 2017.
- [120] M. Ehrensperger and J. Wintterlin. "In situ high-pressure high-temperature scanning tunneling microscopy of a Co(0001) Fischer-Tropsch model catalyst". *Journal of Catalysis*, 319:274–282, 2014.
- [121] A. Stroppa, F. Mittendorfer, J. N. Andersen, G. Parteder, F. Allegretti, S. Surnev, and F. P. Netzer. "Adsorption and dissociation of CO on bare and Ni-decorated stepped Rh(553) surfaces". *Journal of Physical Chemistry C*, 113(3):942–949, 2009.
- [122] A. L. Walter, F. Schiller, M. Corso, L. R. Merte, F. Bertram, J. Lobo-Checa, M. Shipilin, J. Gustafson, E. Lundgren, A. X. Brión-Ríos, P. Cabrera-Sanfeliix, D. Sánchez-Portal, and J. E. Ortega. "X-ray photoemission analysis of clean and carbon monoxide-chemisorbed platinum(111) stepped surfaces using a curved crystal". *Nature Communications*, 6:1–7, 2015.
- [123] B. Tränkenschuh, N. Fritsche, T. Fuhrmann, C. Papp, J. F. Zhu, R. Denecke, and H. P. Steinrück. "A site-selective in situ study of CO adsorption and desorption on Pt(355)". *Journal of Chemical Physics*, 124(7):074712–1–074712–9, 2006.
- [124] B. Tränkenschuh, C. Papp, T. Fuhrmann, R. Denecke, and H. P. Steinrück. "The dissimilar twins - a comparative, site-selective in situ study of CO adsorption and desorption on Pt(3 2 2) and Pt(3 5 5)". *Surface Science*, 601(4):1108–1117, 2007.
- [125] J. W. Gibbs. *Elementary Principles in Statistical Mechanics*. Cambridge University Press, U.S.A, 1902 - 1<sup>st</sup> edition. ISBN 9780511686948.
- [126] H. Papp. "Chemisorption and reactivity of carbon monoxide on a Co(11 $\bar{2}$ 0) single crystal surface; studied by LEED, UPS, EELS, AES and work function measurements". *Surface Science*, 149:460–470, 1985.
- [127] H. R. Siddiqui, X. Guo, I. Chorkendorff, and J. T. Jr. Yates. "CO adsorption site exchange between step and terrace sites on Pt(112)". *Surface Science*, 191:L813–L818, 1987.
- [128] H. Hopster and H. Ibach. "Adsorption of CO on Pt(111) and Pt 6(111)  $\times$  (111) studied by high resolution electron energy loss spectroscopy and thermal desorption spectroscopy". *Surface Science*, 77(1):109–117, 1978.
- [129] C. Klünker, M. Balden, S. Lehwald, and W. Daum. "CO stretching vibrations on Pt(111) and Pt(110) studied by sum-frequency generation". *Surface Science*, 360(1-3): 104–111, 1996.
- [130] G. Lauth, T. Solomun, W. Hirschwald, and K. Christmann. "The interaction of CO with Ru(10 $\bar{1}$ 0) surface". *Surface Science*, 210:201–224, 1989.

- [131] H. Pfnür, P. Feulner, H. A. Engelhardt, and D. Menzel. "An example of "fast" desorption: Anomalously high pre-exponentials for CO desorption from Ru(001)". *Chemical Physics Letters*, 59(3):481–486, 1978.
- [132] D. G. Castner, B. A. Sexton, and G. A. Somorjai. "Leed and thermal desorption studies of small molecules (H<sub>2</sub>, O<sub>2</sub>, CO, CO<sub>2</sub>, NO, C<sub>2</sub>H<sub>4</sub>, C<sub>2</sub>H<sub>2</sub> AND C) chemisorbed on the rhodium (111) and (100) surfaces". *Surface Science*, 71(3):519–540, 1978.
- [133] G. Ertl and J. Koch. "Adsorption von CO auf einer Palladium(111)-Oberfläche". *Zeitschrift für Naturforschung - Section A Journal of Physical Sciences*, 25(12):1906–1912, 1970.
- [134] W. L. Yim, T. Nowitzki, M. Necke, H. Schnars, P. Nickut, J. Biener, M. M. Biener, V. Zielasek, K. Al-Shamery, T. Klüner, and M. Bäumer. "Universal phenomena of CO adsorption on gold surfaces with low-coordinated sites". *Journal of Physical Chemistry C*, 111(1):445–451, 2007.
- [135] H. P. Steinrück, M. P. D'Evelyn, and R. J. Madix. "The role of defects in the dissociative adsorption of CO on Ni(100)". *Surface Science*, 172(3):L561–L567, 1986.
- [136] P. Van Helden, I. M. Ciobîcă, and R. L. J. Coetzer. "The size-dependent site composition of FCC cobalt nanocrystals". *Catalysis Today*, 261:48–59, 2016.
- [137] U. Burgun, H. R. Zonouz, H. Okutan, H. Atakül, S. Senkan, A. Sarioglan, and G. G. Gur. "Effects of Rare Earth Metal Promotion over Zeolite-Supported Fe-Cu-Based Catalysts on the Light Olefin Production Performance in Fischer-Tropsch Synthesis". *ACS Omega*, 8:648–662, 2022.
- [138] S. Fonseca, G. Maia, and L. M. C. Pinto. "Hydrogen adsorption in the presence of coadsorbed CO on Pd(111)". *Electrochemistry Communications*, 93(July):100–103, 2018.
- [139] M. Huang and K. Cho. "Density functional theory study of CO hydrogenation on a MoS<sub>2</sub> surface". *Journal of Physical Chemistry C*, 113(13):5238–5243, 2009.
- [140] V. H. Jr. Baldwin and J. B. Hudson. "Coadsorption of Hydrogen and Carbon Monoxide on (111) Platinum". *Journal of Vacuum Science and Technology*, 8(1):49–52, 1971.
- [141] X. C. Guo and D. A. King. "Coadsorption of Carbon Monoxide and Hydrogen on Metal Surfaces". *Chemical Physics of Solid Surfaces*, 6(C):113–155, 1993.
- [142] H. Conrad, G. Ertl, and E. E. Latta. "Adsorption of hydrogen on palladium single crystal surfaces". *Surface Science*, 41:435–446, 1974.
- [143] Ts. S. Marinova and D.V. Chakarov. "Coadsorption of carbon monoxide and hydrogen on iridium single crystals". *Surface Science*, 217:65–77, 1989.
- [144] R. Zenobi, J. Xu, and J. T. Yates. "Effects of elevated hydrogen pressures on co chemisorbed on ni(111)". *Surface Science*, 276:241–248, 1992.
- [145] E. A. Lewis, D. Le, A. D. Jewell, C. J. Murphy, T. S. Rahman, and E. C. H. Sykes. "Segregation of Fischer-Tropsch reactants on cobalt nanoparticle surfaces". *Chemical Communications*, 50(49):6537–6539, 2014.
- [146] C. J. Weststrate and J. W. Niemantsverdriet. "Understanding FTS selectivity: The crucial role of surface hydrogen". *Faraday Discussions*, 197:101–116, 2017.
- [147] M. Morkel, G. Rupprechter, and H. J. Freund. "Ultrahigh vacuum and high-pressure coadsorption of CO and H<sub>2</sub> on Pd(111): A combined SFG, TDS, and LEED study". *Journal of Chemical Physics*, 119(20):10853–10866, 2003.
- [148] M. Johansson, O. Lytken, and I. Chorkendorff. "The sticking probability for H<sub>2</sub> in presence of CO on some transition metals at a hydrogen pressure of 1 bar". *Surface Science*, 602(10):1863–1870, 2008.

- [149] K. D. Rendulic, A. Winkler, and H. P. Steinrück. "The role of surface defects in the adsorption and desorption of hydrogen on Ni(111)". *Surface Science*, 185(3):469–478, 1987.
- [150] K. M. E. Habermehl-Cwirzen, K. Kauraala, and J. Lahtinen. "Hydrogen on cobalt: The effects of carbon monoxide and sulphur additives on the D<sub>2</sub>/Co(0001) System". *Physica Scripta T*, T108:28–32, 2004.
- [151] Z. Huesges and K. Christmann. "Interaction of hydrogen with a Co(0001) surface". *Zeitschrift für Physikalische Chemie*, 227(6-7):881–899, 2013.
- [152] D. E. Peebles, J. A. Schreifels, and J. M. White. "The interaction of coadsorbed hydrogen and carbon monoxide on Ru(001)". *Surface Science*, 116(1):117–134, 1982.
- [153] E. D. Williams, P. A. Thiel, W. H. Weinberg, and J. T. Yates. "Segregation of co-adsorbed species: Hydrogen and carbon monoxide on the (111) surface of rhodium". *The Journal of Chemical Physics*, 72(6):3496–3505, 1980.
- [154] G. A. Kok, A. Noordermeer, and B. E. Nieuwenhuys. "Decomposition of methanol and the interaction of coadsorbed hydrogen and carbon monoxide on a Pd(111) surface". *Surface Science*, 135:65–80, 1983.
- [155] C. Burda, X. Chen, R. Narayanan, and M. A. El-Sayed. "Chemistry and properties of nanocrystals of different shapes". *Chemical Reviews*, 105:1025–1102, 2005.
- [156] R. D. Ramsier, Q. Gao, H. Neergaard-Waltenburg, and J. T. Yates. "Thermal dissociation of NO on Pd surfaces: The influence of step sites". *The Journal of Chemical Physics*, 100:6837–6845, 1994.
- [157] C. A. Scamehorn, N. M. Harrison, and M. I. McCarthy. "Water chemistry on surface defect sites: Chemisorption versus physisorption on MgO(001)". *The Journal of Chemical Physics*, 101:1547–1554, 1994.
- [158] Z. Xu, M. G. Sherman, J. T. Jr. Yates, and P. R. Antoniewicz. "Perturbation of a chemisorbed CO molecule by physisorbed Xe". *Surface Science*, 276:249–261, 1992.
- [159] J. M. White and S. Akhter. "Adsorbate-adsorbate interactions during coadsorption on metals". *Critical Reviews in Solid State and Materials Sciences*, 14(2):131–173, 1988.
- [160] R. J. Bartholomew and C. H. Farrauto. *Fundamentals of industrial catalytic processes*, New Jersey. John Wiley and Sons, 2<sup>nd</sup> edition, 2011. ISBN 9780471730071.
- [161] H. Conrad, G. Ertl, and J. Küppers. "Interactions between oxygen and carbon monoxide on a Pd(111) surface". *Surface Science*, 76(2):323–342, 1978.
- [162] R. J. Behm, V. Penka, M. G. Cattania, K. Christmann, and G. Ertl. "Evidence for "subsurface" hydrogen on Pd(110): An intermediate between chemisorbed and dissolved species". *The Journal of Chemical Physics*, 78(110):7486–7490, 2003.
- [163] M. Eriksson and L.-G. Ekedahl. "Real time measurements of hydrogen desorption and absorption during CO exposures of Pd : hydrogen sticking and dissolution". *Applied Surface Science*, 133:89–97, 1998.
- [164] A. Föhlisch, M. Nyberg, P. Bennich, L. Triguero, J. Hasselström, O. Karis, L. G. M. Pettersson, and A. Nilsson. "The bonding of CO to metal surfaces". *Journal of Chemical Physics*, 112:1946–1958, 2000.
- [165] Ts. S. Marinova and D. V. Chakarov. "Coadsorption of carbon monoxide and hydrogen on Iridium single crystals". *Surface Science*, 217:65–77, 1989.
- [166] H. Conrad, G. Ertl, and E. E. Latta. "Coadsorption of hydrogen and carbon monoxide on a pd (110) surface". *Journal of Catalysis*, 35:363–368, 1974.

- [167] K. H. Rieder and W. Stocker. "Hydrogen chemisorption on Pd(100) studied with He scattering". *Surface Science*, 148:139–147, 1984.
- [168] D. Henning, R. Lober, M. Methfessel, M. Scheffler, and S. Wilke. "Ab initio study of hydrogen adsorption on Pd (100)". *Surface science*, 307:76–81, 1994.
- [169] H. Okuyama, W. Siga, N. Takagi, M. Nishijima, and T. Aruga. "Path and mechanism of hydrogen absorption on Pd(100)". *Surface Science*, 401:344–354, 1998.
- [170] H. Wang, R. G. Tobin, D. K. Lambert, G. B. Fisher, and C. L. Dimaggio. "H-CO interactions on the terraces and step edges of a stepped Pt surface". *Surface Science*, 330:173–181, 1995.
- [171] A.M. Bradshaw, D. Hoge, and M. Tushaus. "Island formation during CO/H coadsorption on Pt111 studied by IR reflection-adsorption spectroscopy". *Surface Science Letters*, 207:L935–L942, 1988.
- [172] J. Lauterbach, M. Schick, and W. H. Weinberg. "Coadsorption of CO and hydrogen on the Ir(111) surface Coadsorption of CO and hydrogen on the Ir(111) surface". *Journal of Vacuum Science and Technology A*, 14:1511–1515, 1995.
- [173] G. E. Mitchell, J. L. Gland, and J. M. White. "Vibrational spectra of coadsorbed CO and H on Ni(100) and Ni(111)". *Surface Science*, 131:167178, 1983.
- [174] R. Zenobi, J. Xu, and J. T. Yates. "Effects of elevated hydrogen pressures on CO chemisorbed on Ni(111)". *Surface Science*, 276:241–248, 1992.
- [175] B. Poelsema, K. Lenz, and G. Comsa. "The dissociative adsorption of hydrogen on defect-free Pt(111)". *Journal of Physics Condensed Matter*, 22:1–10, 2010.
- [176] D. Hoge, M. Töshaus, and A. M. Bradshaw. "Island formation during co/h coadsorption on pt111 studied by ir reflection-absorption spectroscopy". *Surface Science*, 207:L935–L942, 1988.
- [177] P. B. Merrill and R. J. Madix. "Site blocking by hydrogen: CO on clean and H-presaturated Fe(100)". *Surface Science*, 271:81–84, 1992.
- [178] L. J. Richter, T. A. Germer, and W. Ho. "Coadsorption-induced site changes: bridging hydrogen from CO and H on Rh(100)". *Surface Science Letters*, 195:182–192, 1988.
- [179] L. J. Richter, B. A. Gurney, and W. Ho. "The influence of adsorbate-adsorbate interactions on surface structure: The coadsorption of co and h2 on rh(100)". *The Journal of Chemical Physics*, 86:477–490, 1987.
- [180] E. I. Ko, J. B. Benziger, and R. J. Madix. "Reactions of methanol on W(100) and W(100)-(5x1)C surfaces". *Journal of Catalysis*, 62:264–274, 1980.
- [181] D. W. Goodman, T. Madey, M. Ono, and J. T. Yates. "Interaction of hydrogen, carbon monoxide, and formaldehyde with ruthenium". *Journal of Catalysis*, 50:27–35, 1977.
- [182] A. D. Johnson, K. J. Maynard, S. P. Daley, Q. Y. Yang, and S. T. Ceyer. "Hydrogen embedded in Ni: Production by incident atomic hydrogen and detection by High-Resolution Electron Energy Loss". *Physical Review Letters*, 67:927–930, 1991.
- [183] D. J. Klinke and L. J. Broadbelt. "A theoretical study of hydrogen chemisorption on Ni(111) and Co(0001) surfaces". *Surface Science*, 429:169–177, 1999.
- [184] M. Bowker and K. C. Waugh. "The adsorption of chlorine and chlorination of ag(111)". *Surface Science*, 134:639–664, 1983.
- [185] S. G. Shetty, I. M. Ciobăcă, E. J. M. Hensen, and R. A. Van Santen. "Site regeneration in the Fischer-Tropsch synthesis reaction: A synchronized CO dissociation and C-C coupling pathway". *Chemical Communications*, 47(35):9822–9824, 2011.

- [186] W. Chen, I. A. W. Filot, R. Pestman, and E. J. M. Hensen. "Mechanism of Cobalt-Catalyzed CO Hydrogenation: 2. Fischer-Tropsch Synthesis". *ACS Catalysis*, 7(12):8061–8071, 2017.
- [187] Z. P. Liu and P. Hu. "A new insight into Fischer-Tropsch synthesis". *Journal of the American Chemical Society*, 124(39):11568–11569, 2002.
- [188] A. T. Gwathmey and R. E. Cunningham. "The influence of crystal face in catalysis". *Advances in Catalysis*, 10:57–95, 1958.
- [189] X. Q. Gong, R. Raval, and P. Hu. "CH<sub>x</sub> hydrogenation on Co(0001): A density functional theory study". *Journal of Chemical Physics*, 122(2):024711–1–024711–6, 2005.
- [190] J. T. Yates. "Surface chemistry at metallic step defect sites". *Journal of Vacuum Science and Technology A: Vacuum, Surfaces, and Films*, 13:1359–1367, 1995.
- [191] G. Ertl, T. Zambelli, J. Wintterlin, and J. Trost. "Identification of the "active sites" of a surface-catalyzed reaction". *Science*, 273:1688–1690, 1996.
- [192] S. Dahl, A. Logadottir, R. C. Egeberg, J. H. Larsen, I. Chorkendorff, E. Törnqvist, and J. K. Nørskov. "Role of steps in N<sub>2</sub> activation on Ru(0001)". *Physical Review Letters*, 83(9):1814–1817, 1999.
- [193] Z. P. Liu and P. Hu. "General rules for predicting where a catalytic reaction should occur on metal surfaces: A density functional theory study of C-H and C-O bond breaking/making on flat, stepped, and kinked metal surfaces". *Journal of the American Chemical Society*, 125:1958–1967, 2003.
- [194] A. Y. Khodakov, A. Griboval-Constant, R. Bechara, and V. L. Zholobenko. "Pore size effects in fischer tropsch synthesis over cobalt-supported mesoporous silicas". *Journal of Catalysis*, 206:230–241, 2002.
- [195] Y. Zhang, D. Wei, S. Hammache, and J. G. Goodwin. "Effect of water vapor on the reduction of Ru-Promoted Co/Al<sub>2</sub>O<sub>3</sub>". *Journal of Catalysis*, 188:281–290, 1999.
- [196] A. Martínez, C. López, F. Márquez, and I. Díaz. "Fischer-Tropsch synthesis of hydrocarbons over mesoporous Co/SBA-15 catalysts: The influence of metal loading, cobalt precursor, and promoters". *Journal of Catalysis*, 220:486–499, 2003.
- [197] O. Kitakami, H. Sato, Y. Shimada, F. Sato, and M. Tanaka. "Size effect on the crystal phase of cobalt fine particles". *Physical Review B*, 56:13849–13854, 1997.
- [198] B. Böller, K. M. Durner, and J. Wintterlin. "The active sites of a working Fischer-Tropsch catalyst revealed by operando scanning tunnelling microscopy". *Nature Catalysis*, 2:1027–1034, 2019.
- [199] R. Van Lent, S. V. Auras, K. Cao, A. J. Walsh, M. A. Gleeson, and L. B. F. Juurlink. "Site-specific reactivity of molecules with surface defects—the case of H<sub>2</sub> dissociation on Pt". *Science*, 363:155–157, 2019.
- [200] P. Van Helden, J. A. Van Den Berg, and I. M. Ciobică. "Hydrogen-assisted CO dissociation on the Co(211) stepped surface". *Catalysis Science and Technology*, 2:491–494, 2012.
- [201] E. Shincho, C. Egawa, S. Naito, and K. Tamaru. "The behaviour of CO adsorbed on Ru(1,1,10) and Ru(001); the dissociation of CO at the step sites of the Ru(1,1,10) surface". *Surface Science*, 149(1):1–16, 1985.
- [202] B. Zijlstra, R. J. P. Broos, W. Chen, H. Oosterbeek, I. A. W. Filot, and E. J. M. Hensen. "Coverage Effects in CO Dissociation on Metallic Cobalt Nanoparticles". *ACS Catalysis*, 9(8):7365–7372, 2019.
- [203] S. Shetty, A. P. J. Jansen, and R. A. Van Santen. "Direct versus hydrogen-assisted CO

- dissociation". *Journal of the American Chemical Society*, 131(36):12874–12875, 2009.
- [204] I. A. W. Filot, R. J. P. Broos, J. P. M. Van Rijn, G. J. H. A. Van Heugten, R. A. Van Santen, and E. J. M. Hensen. "First-Principles-Based Microkinetics Simulations of Synthesis Gas Conversion on a Stepped Rhodium Surface". *ACS Catalysis*, 5(9):5453–5467, 2015.
- [205] A. C. Kizilkaya, J. W. Niemantsverdriet, and C. J. Weststrate. "Oxygen Adsorption and Water Formation on Co(0001)". *Journal of Physical Chemistry C*, 120(9):4833–4842, 2016.
- [206] T. Ramsvik, A. Borg, H. J. Venvik, F. Hansteen, M. Kildemo, and T. Worren. "Acetylene chemisorption and decomposition on the Co(11 $\bar{2}$ 0) single crystal surface". *Surface Science*, 499:183–192, 2002.
- [207] W. Chen, B. Zijlstra, I. A. W. Filot, R. Pestman, and E. J. M. Hensen. "Mechanism of carbon monoxide dissociation on a Cobalt Fischer–Tropsch catalyst". *ChemCatChem*, 10:136–140, 2018.
- [208] J. Vaari, J. Lahtinen, A. Talo, and P. Hautojärvi. "Promotion of CO dissociation by magnesia on Co(0001)". *Surface Science*, 251:1096–1099, 1096.
- [209] M. A. Barteau, R. J. Madix, R. Vanselow, and L. R. Pederson. "Spectroscopic investigation of the interaction between H<sub>2</sub>O and oxygen on Ag(110) observation of compensation effects during the thermal dissolution of aluminum oxide layers on tungsten and molybdenum (111) and on tungsten(110) in the presence of electric fields". *Surface Science*, 140:123–136, 1984.
- [210] A. C. Kizilkaya. "Effect of adsorbate interactions on catalytic reactivity : elementary surface reactions on rhodium and cobalt". *Doctoral thesis, Technical University of Eindhoven*, 2014.
- [211] H. Nakano, S. Kawakami, T. Fujitani, and J. Nakamura. "Carbon deposition by disproportionation of CO on a Ni(977) surface". *Surface Science*, 454(1):295–299, 2000.
- [212] C. J. Weststrate, A. C. Kazalkaya, E. T. R. Rossen, M. W. G. M. Verhoeven, I. M. Ciobîcă, A. M. Saib, and J. W. Niemantsverdriet. "Atomic and polymeric carbon on Co(0001): Surface reconstruction, graphene formation, and catalyst poisoning". *Journal of Physical Chemistry C*, 116(21):11575–11583, 2012.
- [213] H. Nakano and J. Nakamura. "Carbide-induced reconstruction initiated at step edges on Ni(111)". *Surface Science*, 482-485:341–345, 2001.
- [214] H. Nakano, J. Ogawa, and J. Nakamura. "Growth mode of carbide from C<sub>2</sub>H<sub>4</sub> or CO on Ni(111)". *Surface Science*, 514:256–260, 2002.
- [215] K. A. Prior, K. Schwaha, and R. M. Lambert. "Surface chemistry of the non-basal planes of cobalt: The structure, stability, and reactivity of Co(10 $\bar{1}$ 2)-CO". *Surface Science*, 77(2):193–208, 1978.
- [216] J. J. C. Geerlings, M. C. Zonneville, and C. P. M. de Groot. "Structure sensitivity of the Fischer-Tropsch reaction on cobalt single crystals". *Surface Science*, 241(3):315–324, 1991.



# Acknowledgments

As I bring this chapter of my academic life to a close, I find myself filled with gratitude for the many people who stood by me with support, insight and encouragement.

First and foremost, I would like to express my deepest gratitude to my supervisor, Dr. C.J. (Kees-Jan) Weststrate, for his unwavering guidance and for introducing me to the world of surface science experiments. Your supervision throughout the challenging years of my PhD has made me a more capable contributor to my field. Thank you for your patience and support.

I am sincerely thankful to my first promoter, Prof. Dr. Ir. Richard van de Sanden, who stepped in for my initial promoter, Prof. Hans Niemantsverdriet. Without your intervention and continued support, this day would not have been possible. Thank you for believing in me and for guiding me through the final stages of the defense process.

I would also like to extend my heartfelt thanks to Dr. Michael Gleeson for meticulously proofreading my thesis and for your invaluable support during its finalization. I have greatly appreciated your company—whether at DIFFER or during our time at the synchrotrons. Your contribution to my research has been truly significant, and I feel incredibly fortunate to have had you alongside me. Much like Richard, I can confidently say that without you, I would not have reached this milestone.

I want to thank my other committee members prof.dr.ir. Emiel Hensen, prof.dr. Irene Groot, prof.dr.ir. Erwin Kessels, prof.dr.ir. Gerard van Rooij and prof.dr.ir. Mark Saeys. I highly appreciate your efforts in reading and evaluating my dissertation and participating in the defense ceremony.

A special thanks to Prof. Dr. Ir. Mark Saeys for welcoming me into your group in Gent for three months. That experience was a turning point for me, one that reenergized my motivation to continue my PhD journey. Thank you for your openness, your willingness to engage with my ideas, and for fostering a truly collaborative environment. The people in your group - Andres, Sara and Jenoff not only improved the quality of my work, but also made my time there memorable and uplifting. I may be risking too much honesty here, but those three months under your guidance

were vital in helping me realize that my ideas are still good and valid.

Dr Thobani Gambu, I'd really like to thank you for collaborating on computational work on CO adsorption on the stepped and kinked surfaces. It formed a backbone for my thesis chapter and made it more conceptually stronger. It was truly a pleasure working with you. I won't ever forget our lengthy and insightful discussions during COVID when I wasn't able to perform any experiments anymore and spent a lot of time analyzing my results.

Gregory Collinge and Jean-Sabin Mcewen, I'd also like to thank you both for collaboration where we ended up publishing a journal paper together. This was also the moment where I realized that I am completely capable for being a confident researcher.

I would also like to thank other members of Syngaschem B.V.—Dr. Foteini Sarpountzi and Dr. Hans Fredriksen—for their support and insightful feedback during my presentations, and for the many enjoyable lunchtime conversations that often wandered far from science. Those moments provided a welcome balance to my PhD life.

Dani, my office and lab colleague—although we approached research in very different ways, we still managed to collaborate from time to time, especially at synchrotrons and while working with the two experimental setups at DIFFER. Now that we're both at ASML, I'm glad that our paths continue to cross. It's good to still have you around.

Aron Tamminga, you hold an incredibly important place in my life. You've been one of my longest-standing friends in the Netherlands, and I still find it wild that we first met through a "secret club" with six other people—only to be revealed at the end of the year. Among the many things that kept me going during this PhD, your friendship and constant support were truly invaluable. You are one of my most cherished friends, and I'll always be thankful to have you in my life.

To Bram, Corrie, Ronald, Hester, Elise, Lennart, and Thomas—the "wolf family"—you were an essential part of this journey. (Yes, this is the first time I'm using the word journey in this acknowledgment, because I genuinely can't imagine it without you.) I'm deeply grateful for all the laughter, lunches, dinners, sangrias, board games, and so much more. You made these years incredibly special. From scientific and philosophical chats with Ronald, to cooking with Corrie, laughing with Bram and Lennart, volunteering with Hester, and that unforgettable 30 km walk with Elise and Thomas—you all made this experience so much more meaningful. Thank you for being part of it.

How could I ever forget Rifat? We went through so many ups and downs, and yet somehow ended up becoming such good friends by the end of it all. I've always admired your calm presence and your genuine willingness to help, no matter the sit-

uation. You're a truly kind and grounded person, and I consider myself incredibly lucky to have met you, known you, and to now call you a friend. I really hope to see you at my defense—it would mean a lot. Writing this next part feels unexpectedly heavy. I never imagined how much would change between when I started my PhD and the moment I'd be defending it.

Ammaji, you were with me in thought through all the hard days. I could still feel your fingers running through my hair, calming me in moments of despair—that memory was my anchor. I missed you deeply over these years, and I carried you with me every step of the way. I tried my best to be a good girl, just as you would've wanted, even when things were hard. Baba Sahab—your presence in my life has been a constant source of strength, before, during, and even after this PhD journey. I know your attention to detail has rubbed off on me, and maybe that's one reason I ended up doing a PhD at all. You've always taken pride in my achievements, and for that, and for your steady support and encouragement through every chapter of my life, I am truly grateful.

You are truly the light of my life. Since the moment you walked into it, everything became simpler, brighter, and filled with joy. Thank you for caring for me in all the little and big ways—bringing me snacks when I forget to eat, handling chores when I'm overwhelmed, and offering perspectives I might never have considered on my own. Thank you for traveling with me, growing with me, and most of all, for being entirely, wonderfully you—someone who inspires me almost every single day. Your love and support mean more than words can say. Miluji tě.

Vidu, Mummy and Papa — thank you for being my emotional home throughout this journey. You were always just a message or call away, no matter the time zone, the hour, or the chaos in your own life. Your unwavering belief in me, your words of comfort when I was at my lowest, and your contagious laughter in moments when I just needed to breathe—it all meant more than I can put into words. You reminded me to keep going when I doubted myself, and you celebrated my smallest wins like they were your own.

Mummy, thank you for always believing that I'll get to see this day and always making me feel hopeful. Papa – I'll tell you all about this day when I see you again. Thank you for reminding me that who I am matters more than what I achieve, and for loving me through it all. I'm endlessly grateful to be your family—and I dedicate a piece of this milestone to you.

---

# CURRICULUM VITAE

Devyani Sharma was born on 14<sup>th</sup> September 1992 in Delhi, India. She began her academic journey in 2010 by pursuing a Bachelor's degree in Chemical Engineering at Banasthali University, Jaipur. Following graduation, she gained hands-on industry experience as a Plant-in-Charge at a wastewater treatment plant in Delhi. She then transitioned into the automotive sector, where she worked as an R&D engineer focused on designing and developing catalysts for catalytic converters. In 2015, she enrolled in the Master's program in Chemical Engineering at the Indian Institute of Technology (IIT) Madras. As part of her graduate studies, she completed her research thesis in the group of Prof. Karsten Reuter at the Department of

Theoretical Chemistry, Technical University of Munich (TUM), Germany. Following her Master's, she commenced a PhD project at the Dutch Institute for Fundamental Energy Research (DIFFER), with the research results presented in this dissertation. Since early 2022, Devyani has been working at ASML, initially as a Design Engineer and currently as a Product Owner in the Department of Machine Conditioning.





